Analysis of Drifter Dispersion by Rings

A. D. Kirwan*

J. K. Lewis

R. E. Whitaker

Science Applications, Inc.
4348 Carter Creek Parkway
Bryan, Texas 77801

(409) 846-7756

1982

*Present Affilation
Department of Marine Science
University of South Florida
140 7th Avenue South
St. Petersburg, Florida 33701

Prepared for the Minerals Management Service

Contract No. 14-12-0001-29034

ABSTRACT

NDBO deployed three drifters in a warm core ring in Campeche Bay during November 1980. The observed drifter trajectories through April 1981 are presented and discussed. These data allow the evaluation of absolute velocities over the record length. A high frequency mode ($T<24$ h) derived from the original data is removed from the velocity sequences. Causes of this unexpected mode and its influence on previous analyses are discussed.

A new technique for computing the vorticity ζ, divergence D, normal deformation rate N, and shear deformation rate S from a single drifter data set is presented. The derivation is based on analytic solutions of the differential kinematic parameters (DKP) equation in which $\zeta^2 > N^2 + S^2$. The procedure also provides for estimates of ring translation and geometry. The resulting histories of DKP's, swirl and translation speeds and the evolution of the ring's shape and orientation are presented and discussed. The results of this study show that 1) motions within a ring do not separate the drifters, 2) a carefully seeded buoy will suffice to determine the rings DKP's, rotation, translation, and geometry, 3) spectral analysis and filtering may be generally required to utilize drifter data from the Gulf of Mexico, 4) vorticity is the dominant ring DKP, 5) the ring underwent substantial modification moving across Campeche Bay, and 6) typical translation speeds are 5 cm/s and typical swirl speeds are 50 cm/s.

Table of Contents

Tables

Figures

Figures (cont.)

Figures (cont.)

Figures (cont.)

1. Introduction

On 19 November 1980, the NOAA Buoy Office (NDBO) deployed three experimental TzD buoys in the Gulf of Mexico. The purpose of the deployment was to determine the buoy's operational effectiveness for gathering near real-time meteorological and oceanographic data from data-sparse regions. A summary of the analysis of the engineering data is given in "TzD Buoy Operational Test and Evaluation," Final Report of September 30, 1981. In this report, the TzD buoy will frequently be referred to as a drifter.

The three drifters were deployed in a warm core ring which had been shed by the Loop Current. The drifters were deployed at approximately $24^{o}30'N$ and $92^{o}W$. All three drifters stayed in this feature through 17 April 1981 when buoy ID number 1598 left the ring. At that time, the ring was located off the Mexican coast centered approximately at $22^{o}30'N$ and $96^{o}W$. Buoy ID 1600 left the ring early in May 1981. However, drifter ID 1599 continued to track the ring until about 15 June 1981. During the period when the drifters left the ring, it had migrated up against the 1800 meter bathymetric curve off the coast of Mexico. There it interacted strongly with the ocean bottom and, thus, dissipated its ring characteristics.

Since the drifters tracked the ring for such a long period, their trajectories or paths contain considerable information on the currents and horizontal velocity gradients that existed in the ring. These features are important considerations in the design for buoy array dispersion measurements in the open ocean for climate-related programs.

In 1981, Science Applications, Inc. (SAI), was contracted

by the NDBO to analyze these drifter data to provide criteria for the design of such arrays as well as to test the feasibility of using these buoys as a tool for measurements of ocean current kinematics and dynamics. More specifically, SAI performed the following tasks.

Task 1 - Assimilated the drifting buoy data set in a format suitable for data processing and analysis at their Bryan, Texas, facility. The basic data set was furnished by the NDBO.

Task 2 - Developed a computer program to describe the differential kinematic properties (DKP) of the drifting buoy data set prepared in Task 1.

Task 3 - Performed dynamical analysis and made interpretations of the analyzed data set.

Task 4 - Prepared a draft report on the interpretations of dispersion of the array by ring shears and translation, as well as dynamical balance in the ring. Made recommendations on how the drifting buoy system can be used to describe ocean currents and circulation features.

In performing the work described above, an unexpected high frequency component was found in the velocity records. This high frequency fluctuation severly aliased the calculations of the DKP as well as the dynamical calculations. The result was that only a qualitative interpretation could be made regarding the dispersion of the array by ring shears and the dynamical balance within the ring.

Because of this problem, NDBO supplied additional support

to SAI to develop techniques to remove the high frequency fluctuations from the buoy velocity records and to repeat the analysis for the DKP. Specifically, SAI performed the following tasks:

Task 1 - SAI performed cross-spectral and rotary spectral analysis of the velocity records of drifting buoys ID's 1598, 1599 and 1600.

Task 2 - Based on the results obtained in Task 1, SAI developed a low-pass filter and filtered the buoy velocity records in order to remove the previously observed 10-20 cm/s fluctuations with time scales of 24 hours or less.

Task 3 - Using the results from Task 2, SAI repeated the analyses of ring translational and rotational velocity and ring geometry. This is the final report of all of these activities.

2. Theory

2.1 Background

As indicated in the Introduction, there is a large amount of position data available from three drifters which spent five or more months in this ring. In order to address quantitatively questions on the dispersion of drifter arrays by mesoscale processes and on the extrapolation of experience from rings in the Gulf of Mexico to those in the world ocean, it is important to have a parametric model. To be effective, such a model should incorporate approximate physics and summarize a large amount of data in a small number of parameters. The purpose of this section is to document the parametric model used in this study.

The basis for this model is a general variational formulation for geophysical fluid dynamics proposed by J. Stephens (1965, 1967). This formulation has two advantages. First, the parametric equations for the velocity which arise from the functional minimazation are readily connected to the dynamics. The second advantage is that the parameters appearing in the parametric model are constants following the fluid motion. Thus, this formulation is ideally suited to the Lagrangian character of the drifter data.

It should be noted that the variational formulation has a disadvantage which limits its utility as a prognostic tool. The formulation does not allow for internal dissipation. Thus, solutions will be valid for restricted periods.

2.2 Formulation

The basic assumptions required for the variational formulation are discussed extensively by Stephens (1965).

Briefly, these are that the flow is inviscid and is confined to a coordinate frame that is in steady rotation relative to an inertial frame. For this study, additional stipulations are appropriate; namely

1) the flow is horizontal, and

2) the quasi-hydrostatic approximation applies.

For these conditions, the Stephens variational principle can be expressed as

$$I = \int_{t_0}^{t_1} \int_V \{ \tfrac{1}{2} \rho(\vec{v} + \vec{\Omega} \Lambda \vec{r}) \cdot (\vec{v} + \vec{\Omega} \Lambda \vec{r}) - \rho (\varepsilon + \Phi') + \lambda \left(\frac{\partial \rho}{\partial t} + \nabla \cdot \rho \vec{v}\right) - \vec{A} \cdot \frac{d\vec{X}}{dt} \} \, dV dt \qquad (2.1)$$

Here

ρ = density

$\vec{v}$ = velocity relative to the rotating earth

$\vec{\Omega}$ = earth's rotation vector

$\vec{r}$ = position vector from center of earth to the fluid parcel

ε = thermodynamic internal energy

Φ' = gravitational potential excluding the centripetal acceleration

λ = Lagrangian scalar multiplier

$\vec{A}$ = Lagrangian vector multiplier

$\vec{X}$ = Lagrangian coordinate vector

In (2.1), the first term in the integrand represents the absolute kinetic energy density, the second term represents the total potential energy field, the third term represents the conservation of mass, and the last term represents the parcel identity constraint. Note

that the coefficients of λ and $\vec{A}$ are identically zero. By expanding the first term of the integrand and combining the centripetal acceleration terms, $(\vec{\Omega} \Lambda \vec{r}) \cdot (\vec{\Omega} \Lambda \vec{r})$, with Φ', a more convenient form results:

$$I = \int_{t_o}^{t_1} \int_{V} \{ \rho [\vec{v} \cdot \vec{v} + 2 \vec{v} \cdot (\vec{\Omega} \Lambda \vec{r}) - \rho (\epsilon + \Phi) + \lambda \left(\frac{\partial \rho}{\partial t} + \nabla \cdot \rho \vec{v} \right) + \vec{A} \cdot \frac{d\vec{X}}{dt} \} \, dV dt \qquad (2.2)$$

$$\Phi = \Phi' + \rho \, |\vec{\Omega} \Lambda \vec{r}|^2$$

In order to render I an extremum, it is necessary that variations with respect to $\vec{v}$, ρ, $\vec{X}$, $\vec{r}$, and $\vec{A}$ vanish. These conditions lead respectively to:

$$\vec{v} + \vec{\Omega} \Lambda \vec{r} = \nabla \lambda + \vec{A} \cdot \nabla \vec{X} \qquad (a)$$

$$\frac{d\lambda}{dt} + \lambda \nabla \cdot \vec{v} = \frac{\partial}{\partial \rho} (\rho \epsilon) + \tfrac{1}{2} \vec{v} \cdot \vec{v} + \vec{v} \cdot (\vec{\Omega} \Lambda \vec{r}) - \Phi \qquad (b)$$

$$\frac{d\vec{A}}{dt} = 0 \qquad (c) \qquad (2.3)$$

$$\frac{\partial \rho}{\partial t} + \vec{v} \cdot \nabla \rho \vec{v} = 0 \qquad (d)$$

$$\frac{d\vec{X}}{dt} = 0 \qquad (e)$$

These results are given in slightly different form by Stephens (1965).

Equation (2.3 a) shows that the Lagrangian multipliers λ and $\vec{A}$ play the role of a scalar and vector potentials for the absolute velocity. Incidently, this can be expressed in terms of the relative velocity by incorporating $\vec{\Omega} \Lambda \vec{r}$ in the right hand side. Through Clebsch, Helmholtz and numerous other theorems, λ and $\vec{A}$ can be replaced by three scalar functions, two of which will obey an equation of the form (2.3 c). Equation (2.3 b) is recognized as a

form of Bernoulli's equation. Equation (2.3 c) says that the vector $\vec{A}$ is conserved following the fluid motion. This suggests an interpretation of $\vec{A}$ as a measure of the vorticity although this is not a unique interpretation. In this regard, equations (2.3 c) and (2.3 d) can be combined to produce a potential vorticity equation. Equations (2.3 d) and (2.3 e) merely re-express the original constraints of conservation of mass and parcel identity.

The equations of motion may be obtained from (2.3) by taking the gradient of (2.3 b) and subtracting it from the local time derivative of (2.3 a), eliminating Φ, and noting that $\nabla \frac{\partial}{\partial \rho} (\rho \varepsilon) = \frac{1}{\rho} \nabla P$, where P is the thermodynamic pressure.

In order to apply these results, the velocity $\vec{V}$ (components $\tilde{u}$ and $\tilde{v}$) is partitioned into two parts: a translation velocity $\vec{U}$ and a swirl velocity $\vec{u}$. In component form, (2.3 a) then becomes:

$$\begin{aligned} \tilde{u} &= U + u \\ \tilde{v} &= V + v \end{aligned} \tag{2.4}$$

In (2.3 a), λ and X are expanded in a power series in the space coordinates x and y. The zero order terms are identified with the translation velocity $\vec{U}$ and the swirl velocity becomes, to first order,

$$\begin{aligned} u &= \left(\frac{D+N}{2}\right) x + \left(\frac{S-\zeta}{2}\right) y \\ v &= \left(\frac{S+\zeta}{2}\right) x + \left(\frac{D-N}{2}\right) y \end{aligned} \tag{2.5}$$

The entities D, N, S, and ζ may vary both with position and time but must be constant along a parcel path. Precise physical interpretations depend upon the parameters used in (2.3 a). In the

model to be discussed shortly, they can be identified with the components of the velocity gradient or differential kinematic properties (DKP); i.e., the horizontal divergence, normal deformation rate, shear deformation rate, and local vorticity. In general, however, they can be regarded as shape parameters which specify the geometry of the ring.

2.3 Solutions

Previous studies have estimated the DKP by determining the u_i, v_i, x_i, and y_i from absolute position data and then employing least squares (Molinari and Kirwan, 1975; Okubo and Ebbysmeyer, 1976; Lewis and Kirwan, 1981). These procedures assumed that the independent variables in the least squares equations (drifter velocities and positions) were determined independently and that the appropriate center for the expansion in (2.5) is the center of mass of the cluster. The first assumption is never true, and the second prevents the technique from being applied to drifter data from an eddy or ring if we wish to expand about the center of the eddy or ring. The analysis procedure developed in this study provides a means of overcoming these shortcomings by making explicit use of appropriate solutions to (2.5). To this end, note that equations (2.5) are coupled, first order differential equations for the present position of the i^{th} drifter. The form of the solution for these equations is crucially dependent on the frequency parameter

$$\gamma^2 = N^2 + S^2 - \zeta^2. \tag{2.6}$$

There are three classes of solutions depending on different values of γ^2 (see Okubo, 1970, for a discussion). All three can be

expressed in the form

$$x_i(t) = X_i\, H(t) + Y_i\, J(t)\, (S-\zeta)/\gamma$$

$$y_i(t) = X_i\, J(t)\, (S+\zeta)/\gamma + Y_i\, K(t) \qquad (2.7)$$

The X_i and Y_i are the coordinates of the i^{th} drifter at time t = o relative to the local origin at that time.

The forms for the H, J and K functions depend upon γ^2. Table 1 summarizes the possibilities. This table shows that, with D = 0, when the sum of squares of the shear and normal distortion exceed the squared vorticity ($\gamma^2 > 0$, case I), then the drifter displacements will increase exponentially with time (of course a convergence of the cluster would tend to counteract this effect). For case II ($\gamma^2 = 0$), the solutions predict that the drifter displacements will grow linearly with time (aside from the exponential divergence term). Finally, for case III ($\gamma^2 < 0$), the solution shows that the drifter trajectories (relative to the ring center) form ellipses (for D=0). For the exceptional situation when $N^2 = S^2 = 0$, these ellipses become circles. It is case III which is most applicable to this study.

Petterssen (1953) and Okubo (1970) have provided some additional physical insight into these three cases. Their discussion can be summarized succinctly by considering a non-dimensional parameter which we shall refer to as the Petterssen-Okubo (PO) number. This is given by

γ^2	H(t)	J(t)	K(t)
> 0	$e^{Dt/2}\,(\cosh \gamma\, t/2 + (N/\gamma)\, \sinh \gamma t/2)$	$e^{Dt/2} \sinh \gamma t/2$	$e^{Dt/2}(\cosh \gamma t/2 - (N/\gamma)\sinh \gamma t/2)$
$= 0$	$e^{Dt/2}\,(1 + N\, t/2)$	$(te^{Dt/2})/2$	$e^{Dt/2}(1 - Nt/2)$
< 0	$e^{Dt/2}\,(\cos \gamma t/2 + (N/\gamma)\, \sin \gamma t/2)$	$e^{Dt/2}\, \sin \gamma t/2$	$e^{Dt/2}(\cos \gamma t/2 - (N/\gamma)\, \sin \gamma t/2)$

Table 1 Definitions of the H, J, and K functions. Here γ represents the magnitude of $[N^2 + S^2 - \zeta^2]^{\frac{1}{2}}$.

$$PO = \sqrt{(N^2 + S^2)/\zeta^2}\ .$$

This number represents the ratio of the magnitudes of total horizontal deformation and of vorticity about the vertical.

A pivotal value is PO = 1, which corresponds to case II. Petterssen (1953) has pointed out that, in this case, the local current is composed of a translation velocity and a lateral shear. Also, the geostrophic vorticity is balanced by the Laplacian of the geopotential. Values of PO greater than one (case I) indicate flows in which deformation is the dominate factor. Then the solutions given above show displacements which increase exponentially with time. Petterssen (1953) has noted that, in this case, the Laplacian of the geopotential is a diagnostic of the total deformation and not the vorticity. Since this is not consistent with the geostrophic approximation, these motions most likely will be associated with scales less than geostrophic scales.

It is expected that quasi-geostrophic motions will be associated with PO values less than one. From (2.7) and Table 1, it is seen that such motions are periodic with a frequency of

$$\gamma/2 = \pm\ (\zeta/2)\ \sqrt{1 - (PO)}.$$

Here the plus root is taken for cyclonic motion and the minus root for anticyclonic motion. Note that γ is not a reliable measure of the true voriticy since it is an underestimate in cyclonic motion and an overestimate in anticyclonic motion. At the limiting value of PO = 0, it is exact.

This suggests that the PO plays a role in horizonally sheared motions analogous to the Brunt-Vasaila (BV) frequency

in vertical motions. For $0 \leq PO < 1$ the motion is periodic and presumably stable. But for $PO > 1$ the motion has unstable characteristics similar to negative BV's.

It should be noted that, for appropriately short times (i.e. $Dt/2$ and $\gamma t/2 << 1$) all cases represented in (2.7) reduce to the approximate linear form:

$$x_i = X_i + t\,[X_i\,(D + N)/2 + Y_i(S-\zeta)/2]$$

$$y_i = Y_i + t\,[X_i\,(S + \zeta)/2 + Y_i\,(D-N)/2]\,. \tag{2.8}$$

This equation says that the present position relative to the moving origin is obtained by adding to the previous relative position the displacements due to the velocity induced by the average rotation, divergence and distortion of the cluster during the time interval.

We now see that the analytical solutions provide information concerning three important factors:

a) The solutions give us a system of equations in which the only independent variables are position. This eliminates the problem of having two independent variables (position and velocity) that are not determined independently.

b) The solutions give the correct form of the Taylor's expansion to calculate the DKP. This form is quite convenient in that it does not require position fixes at a constant time interval.

c) The solutions show that the equations in (2.8) can be used only for time intervals t between position fixes such that

$\frac{Dt}{2}$ and $\frac{\gamma t}{2} << 1$.

2.4 Geometric Interpretation of Solutions

To summarize for the case applicable to Gulf of Mexico rings (case III), the paths relative to the ring's center are given by

$$x = \{X[\cos \gamma t/2 + (N/\gamma) \sin \gamma t/2] + Y((S-\zeta)/\gamma) \sin \gamma t/2\} \cdot e^{Dt/2}$$
$$y = \{X((S+\zeta)/\gamma) \sin \gamma t/2 + Y[\cos \gamma t/2 - (N/\gamma) \sin \gamma t/2]\} \cdot e^{Dt/2}. \quad (2.9)$$

Here X and Y refer to the initial position relative to the ring center. The subscript i has been deleted since (2.9) may be written for each drifter.

By elementary trigonometric identities, (2.9) can be expressed as

$$x = A_x \cos(\gamma t/2 + M + \Gamma) e^{Dt/2}$$
$$y = B_y \sin(\gamma t/2 + M - \Gamma) e^{Dt/2} \quad (2.10)$$

where

$$A_x^2 = X^2 + [X N + Y (S-\zeta)]^2/\gamma^2$$
$$B_y^2 = Y^2 + [X (S+\zeta) - Y N]^2/\gamma^2 \quad (2.11)$$

$$M = \tfrac{1}{2}\{\tan^{-1}[\frac{-(XN+Y(S-\zeta))}{\gamma X}] + \tan^{-1}[\frac{Y\gamma}{(X(S+\zeta)-YN}]\} \quad (2.12)$$

$$\Gamma = \tfrac{1}{2}\{\tan^{-1}[\frac{-(XN+Y(S-\zeta))}{\gamma X}] - \tan^{-1}[\frac{Y\gamma}{(X(S+\zeta)-YN}]\} .$$

Equation (2.10) demonstrates clearly that the motion is periodic with amplitudes which increase or decrease exponentially in time

depending upon whether there is horizontal convergence ($D<0$) or divergence ($D>0$). The period of the motion is

$$T = 4\pi/\gamma \tag{2.13}$$

and there is a phase shift between the x and y components of $2\Gamma + \pi/2$ radians.

As will be demonstrated below, the analysis is performed over half period increments. Thus, the maximum value of $Dt/2$ is

$$Dt/2 = DT/4 - D\pi/\gamma .$$

If $D\pi/\gamma << 1$, then the exponential factor in (2.10) can be neglected. This will be assumed to be true for the moment. In Appendix A, two methods are presented for extending the theory to account for divergence. Note that with $D\pi/\gamma << 1$, (2.10) become parametric equations for an ellipse (Thomas, 1958). The angle that the major axis of the ellipse makes with the X (east/west) axis is

$$\delta = \tfrac{1}{2} \tan^{-1} \left\{ \left[\frac{2 A_x B_y}{B_y^2 - A_x^2} \right] \sin 2\Gamma \right\} . \tag{2.14}$$

The major axis length is given by $(A_x^2 + B_y^2)^{\frac{1}{2}}$ and the minor axis length by $(|A_x^2 - B_y^2|)^{\frac{1}{2}}$.

Differentiation of (2.10) gives the swirl velocities:

$$u = -(\gamma/2)\, A_x \sin(\gamma t/2 + M + \Gamma) = (\gamma/2) A_x \cos(\gamma t/2 + M + \pi/2 + \Gamma)$$

$$v = (\gamma/2)\, B_y \cos(\gamma t/2 + M - \Gamma) = (\gamma/2) B_y \sin(\gamma t/2 + M + \pi/2 - \Gamma)$$

or (2.15)

$$u = A_u \cos(P + \Gamma)$$

$$v = B_v \sin(P - \Gamma).$$

where

$$A_u = (\gamma/2)\, A_x$$

$$B_v = (\gamma/2)\, B_y$$

$$P = \gamma t/2 + M + \pi/2 .$$

From this it is seen that the hodograph of the swirl velocities also forms an ellipse with the same orientation as the ellipse for the paths. Note that there is a phase shift of $\pi/2$ radians between the two ellipses.

By substituting (2.11) and (2.12) into (2.14) and subsequent reduction, it is seen that

$$\tan 2\delta = - N/S . \tag{2.16}$$

This result provides a simple geometric interpretation of the role of N and S on ring phase. To see this, take the special case of N=0. Then δ=0 or $\pi/2$. If S > 0, then the major axis of the ellipse is along the x (east/west) direction (i.e. δ = 0). But if S < 0, then the major ellipse axis is along the y (north/south) direction ($\delta = \pi/2$). On the other hand, if S = 0, then $\delta = \pm \pi/4$. This means that the major axis is 45° north of east if N < 0 and 45° south of east if N > 0.

2.5 Ring Translation

The solutions given by (2.10) or (2.11) are merely for the paths relative to the moving ring center. The absolute path is given by the integral of (2.4). This is

$$\int_0^t \tilde{u}\,(\lambda)\, d\lambda = \int_0^t U\,(\lambda)\, d\lambda + x(t)$$

$$\int_0^t \tilde{v}\,(\lambda)\, d\lambda = \int_0^t V\,(\lambda)\, d\lambda + y(t). \tag{2.17}$$

The integrals on the RHS of (2.17) represent the translation or path of the ring center. Finally, x(t) and y(t) are the positions relative to the ring center. They are given by (2.10):

$$x(t) = A_x \cos(\gamma t/2 + M + \Gamma)\, e^{Dt/2}$$

$$y(t) = B_y \sin(\gamma t/2 + M - \Gamma)\, e^{Dt/2}. \tag{2.18}$$

Of special interest to this study is the case of U and V constant for one rotation period. Then the absolute path form one of three possible geometric forms. First, if U and V are zero the paths are elliptical in shape but will not close if $D \neq 0$. The other two forms depend upon the ratio of the swirl velocity magnitude to the magnitude of the translation velocity. If this ratio is less than 1, then the paths form wave-like patterns that do not close. If the ratio is 1, then the path will form a cusp when the swirl velocity and translation velocity are opposed. Finally, when the ratio is greater than 1, the paths will form closed loops.

2.6 Relationship Between Theory and Observations

The quantities in the theory that are observed are $\tilde{u}$ and $\tilde{v}$. From these observations, we need to calculate the DKP and the ring translation velocities U and V. These 6 quantities can be calculated from values of each of the absolute velocities at three critical points, which are three successive extrema.

There are three stages to the calculation given the six critical values of the absolute velocity. The first stage is to note $\gamma/2$ and Γ along with the values of the absolute velocities.

The $\gamma/2$ quantity is readily determined by noting the time between successive extreme for each component (there are separate $\gamma/2$'s for the $\tilde{u}$ and $\tilde{v}$ records). Then we use

$$\gamma/2 = \pi(1/(t_2 - t_1) + 1/(t_3 - t_2))$$

where t_i are the times of successive extrema.

The calculation of Γ is slightly more complicated. The following sequence has been developed from the theoretical expressions for the swirl velocity for an anticyclonic ring:

- For a $\tilde{u}_{max}$ followed by a $\tilde{v}_{min}$ or a $\tilde{u}_{min}$ followed by a $\tilde{v}_{max}$,

  $2\Gamma = \pi/2 - (t_u - t_v)\,\gamma/2$

- For a $\tilde{v}_{min}$ followed by a $\tilde{u}_{min}$ or a $\tilde{v}_{max}$ followed by a $\tilde{u}_{max}$,

  $2\Gamma = -\pi/2 - (t_u - t_v)\,\gamma/2.$

Note that for purely circular motion, $2\Gamma = -\pi/2$.

The second stage is the calculation of the translation velocities and swirl velocity amplitudes. The paradigm for this is given in Appendix A.

Finally, from the swirl velocities it is possible to calculate the DKP from A_u, B_v and Γ. To this end note that, apart from the divergence term, a constant of motion obtained from (2.10) and (2.15) is the angular momentum/unit mass. This is given by

$$vy - ux = L = (2/\gamma)\, A_u\, B_v \cos 2\Gamma. \qquad (2.19)$$

Then using the "Stokes" relations, the remaining DKP can be calculated from

$$\zeta = (A_u^2 + B_v^2)/2\ L$$
$$S = (B_v^2 - A_u^2)/2\ L \qquad (2.20)$$
$$N = -A_u B_v \sin 2\ r/2L.$$

3. Discussion of Drifter Paths

The basic data set used in this study are sequential positions of drifters ID's 1598, 1599, and 1600. These data were supplied by the NDBO. The paths for each of the drifters are shown in Figures 1a, 1b, and 1c from the time of deployment, 19 November 1980, until 11 May 1981. By that time, ID's 1598 and 1600 had left the ring. From close inspection of the position data it appears that ID 1598 left the ring shortly after the 17th of April 1981, moving northward approximately along the 1800 meter depth contour. Drifter ID 1600 apparently left the ring during the first week of May 1981. It also moved northward generally following the depth contours. However, drifter ID 1599 apparently stayed with the ring until mid June 1981.

That two of the drifters left the ring in April and May 1981 is not surprising. At that time the ring was located off the coast of Mexico centered approximately at 22°30'N and 96°W. The ring center was located in approximately 1800 meters of water. This is located on the continental rise. The water depth decreases rapidly towards the west. In the space of 100 kilometers the depth decreases to 200 meters. Thus the ring was interacting strongly with the bottom topography. This interaction rapidly dissipates the energy and alters the shape of the ring. Thus the ring most likely had lost its basic characteristics when the drifters migrated to the north.

An examination of the paths shown in Figures 1a, 1b, and 1c reveals several interesting features. First it is noteworthy that, from the deployment in November 1980 until the middle of April

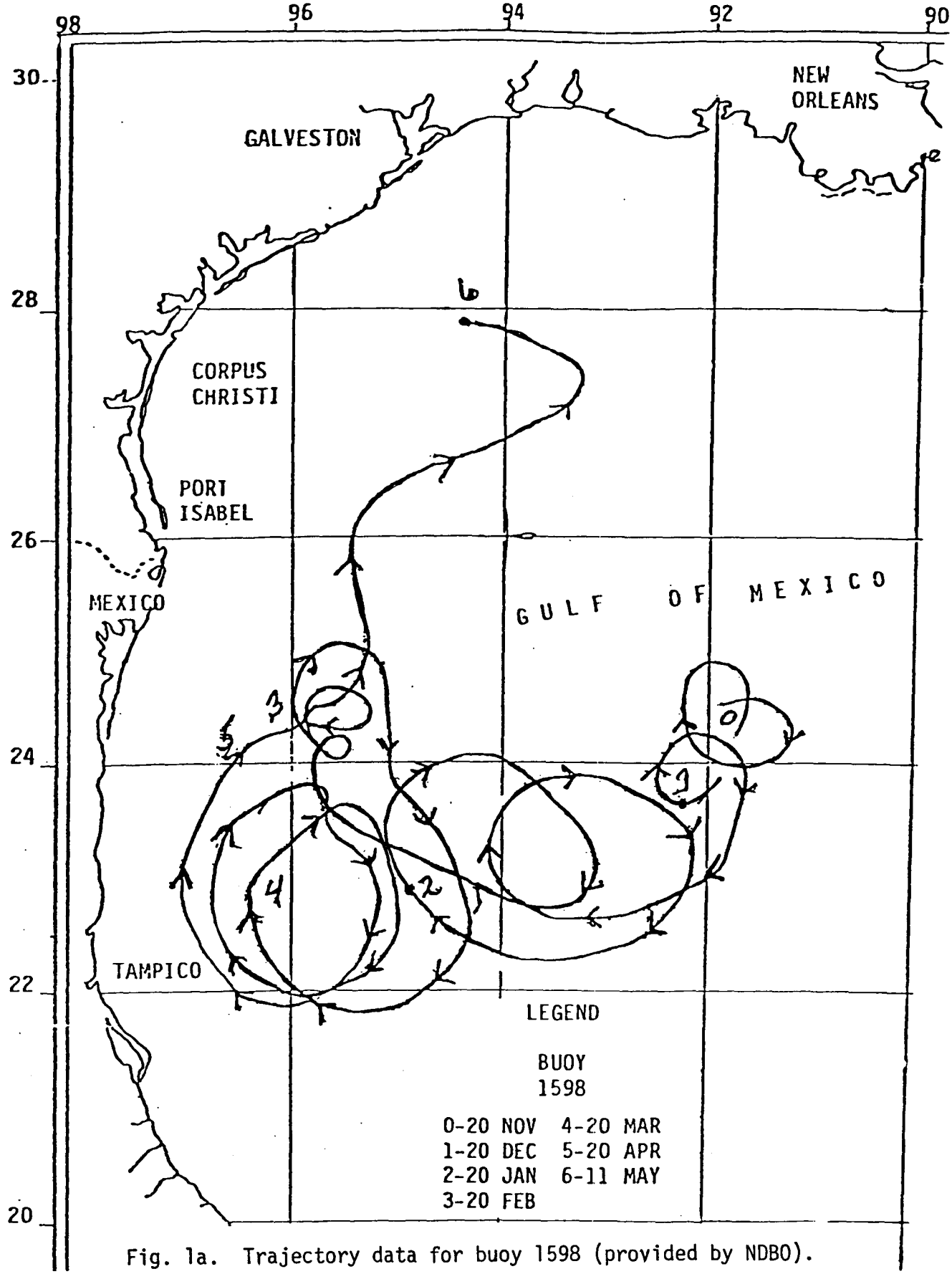

Fig. 1a. Trajectory data for buoy 1598 (provided by NDBO).

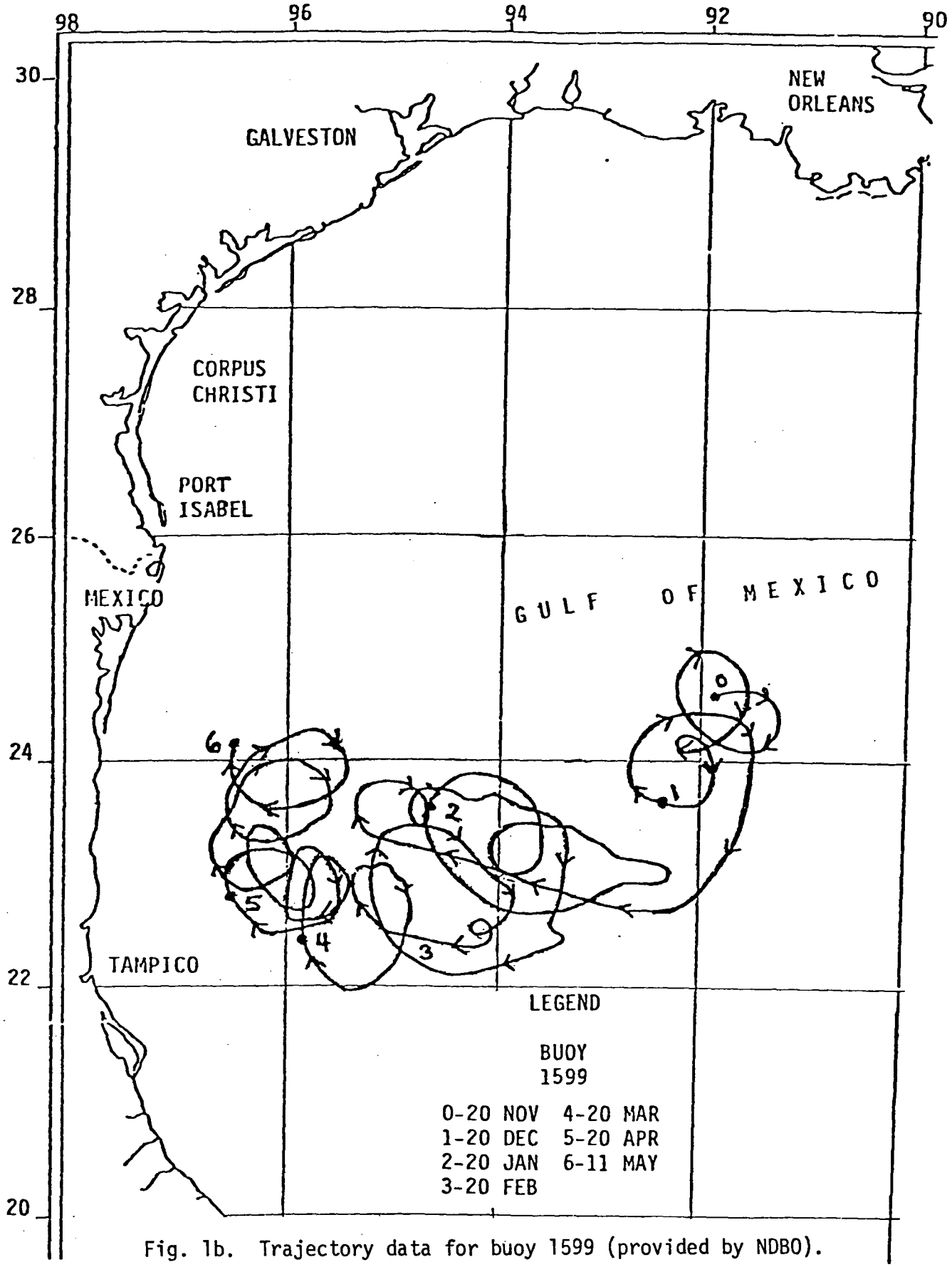

Fig. 1b. Trajectory data for buoy 1599 (provided by NDBO).

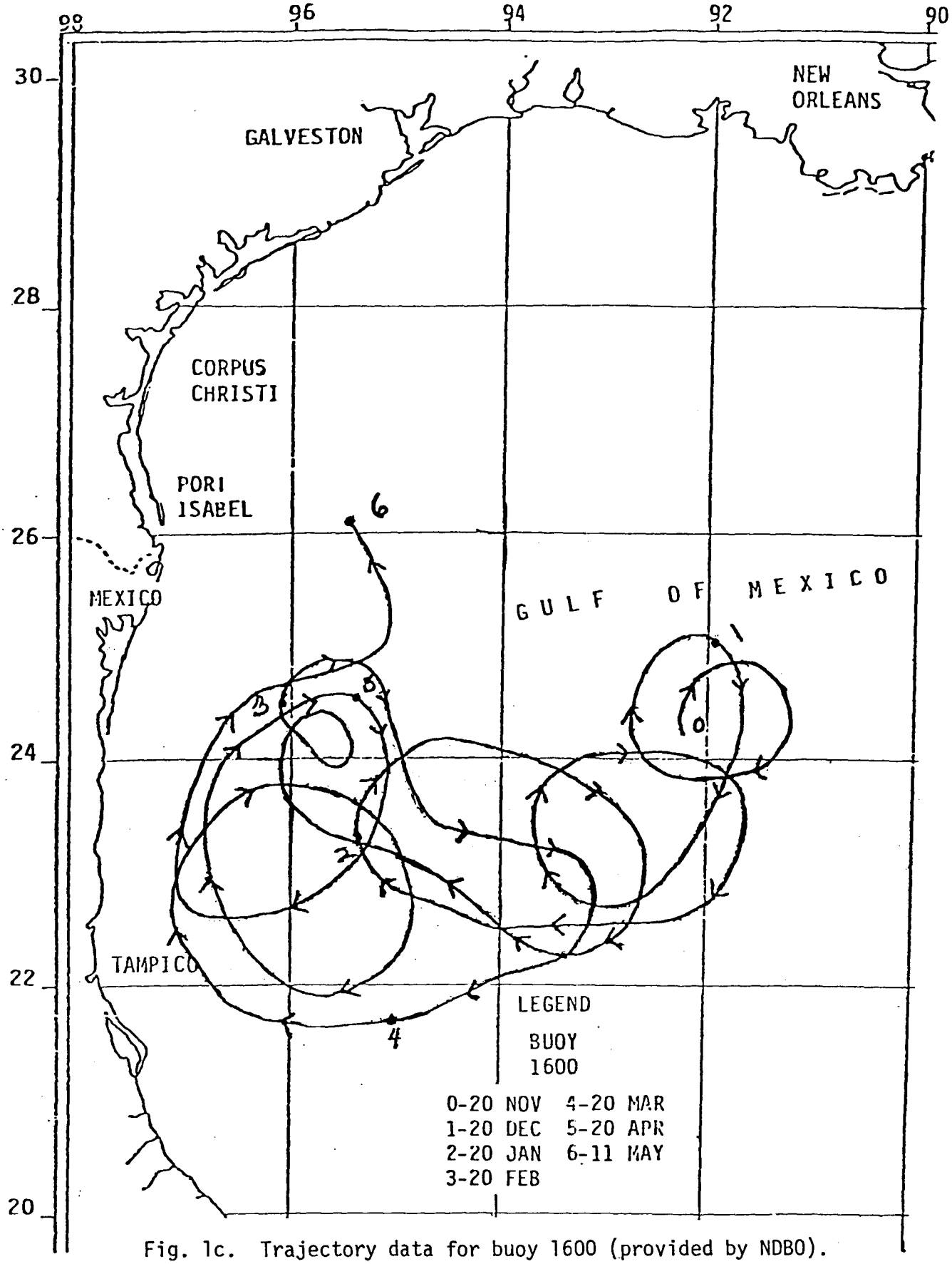

Fig. 1c. Trajectory data for buoy 1600 (provided by NDBO).

1981, the drifter paths traversed the same general region of the Gulf of Mexico and there was no permanent separation of the drifters during this period.

Closer inspection of these figures reveal, however, substantial differences in local characteristics of the paths. For example, early in the deployment the paths of ID's 1598 and 1599 are very similar, but as the ring migrates from 24°N, 92°W to 23°30'N, 94°W ID 1598's path shows much larger loops or perhaps wave-like features rather than closed loops. On the other hand, ID 1600's path shows bigger loops than the other two drifters early in the deployment. Yet, when the ring has migrated to 96°W, ID 1600's path is very similar to that of ID 1598.

At various times in the five month period that all three drifters were in the ring, all of the paths exhibit slowly migrating loops, very small loops, or cusps and large wave-like features rather than closed loops. As explained in the previous section, all three of these types of features can be explained by the ratio of the translation velocity to the swirl velocity.

Figures 2-4 show the trajectories for ID's 1598, 1599 and 1600 broken down in 15-day intervals. This interval was selected because it is slightly larger than the average period of rotation of the ring.

The (a) panels indicate that ID's 1598 and 1599 were deployed quite close together (approximately 10 km) and closer to the ring center than 1600. All three trajectories show westward translation of the ring. During the first part of December 1980 (the (b)

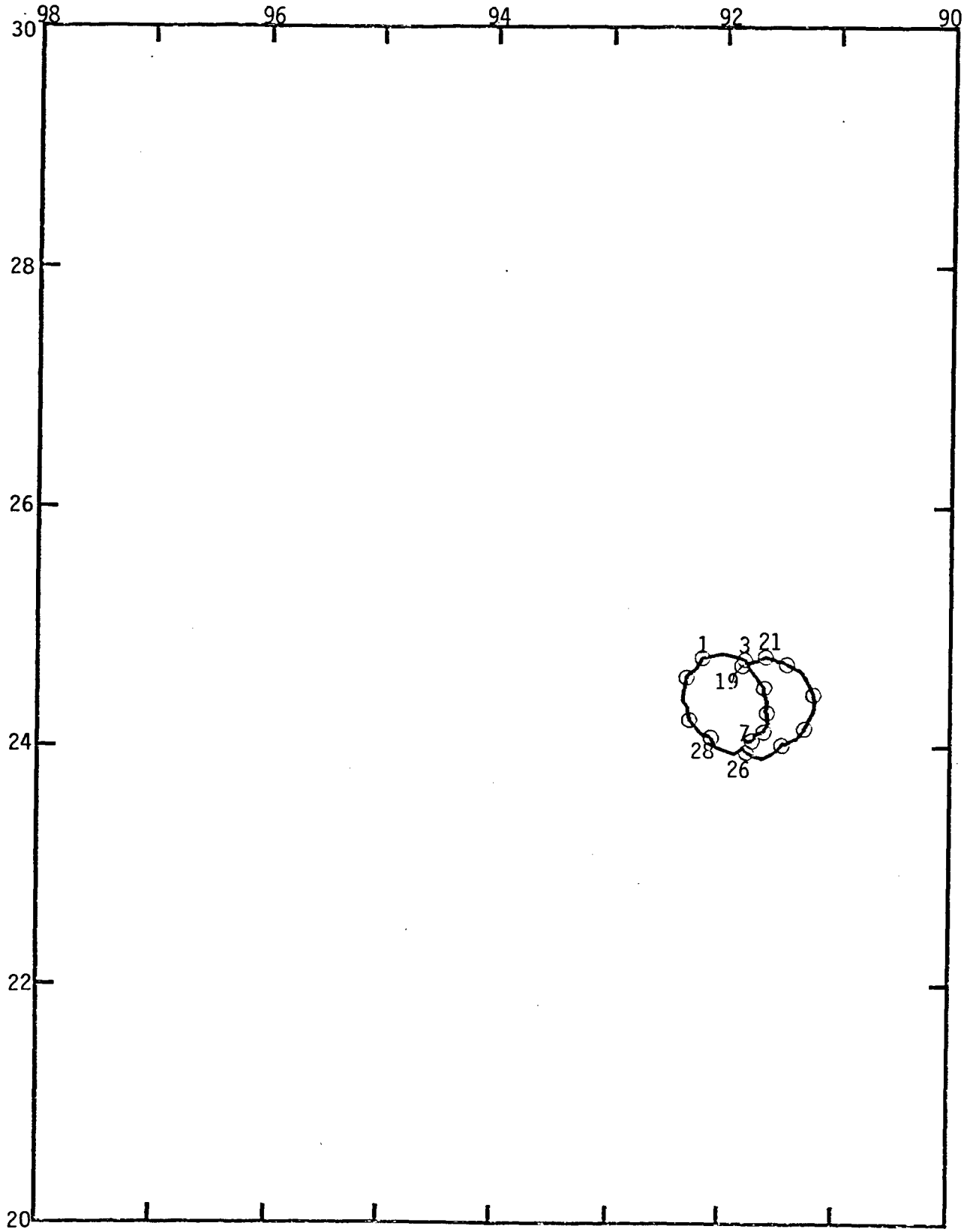

Fig. 2a. Buoy 1598 trajectory 19 Nov 80 - 7 Dec 80. The trajectories begin with the thin line and the circles correspond to position nearest to 0000 hrs (no circles for 20, 27 Nov and 2 Dec). Scales are longitude and latitude.

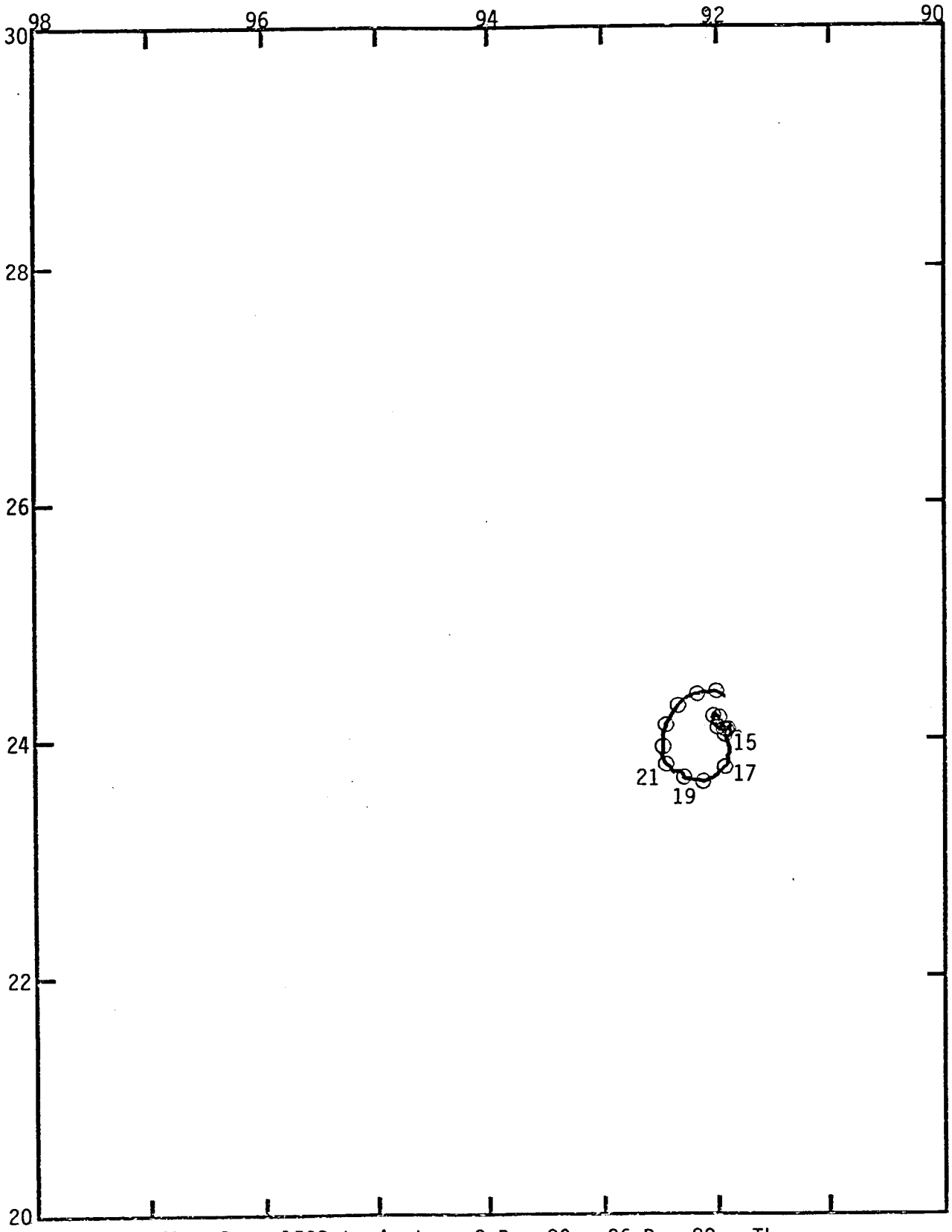

Fig. 2b. Buoy 1598 trajectory 8 Dec 80 - 26 Dec 80. The trajectories begin with the thin line and the circles correspond to position nearest to 0000 hrs (no circles on 16 and 20 Dec). Scales are longitude and latitude.

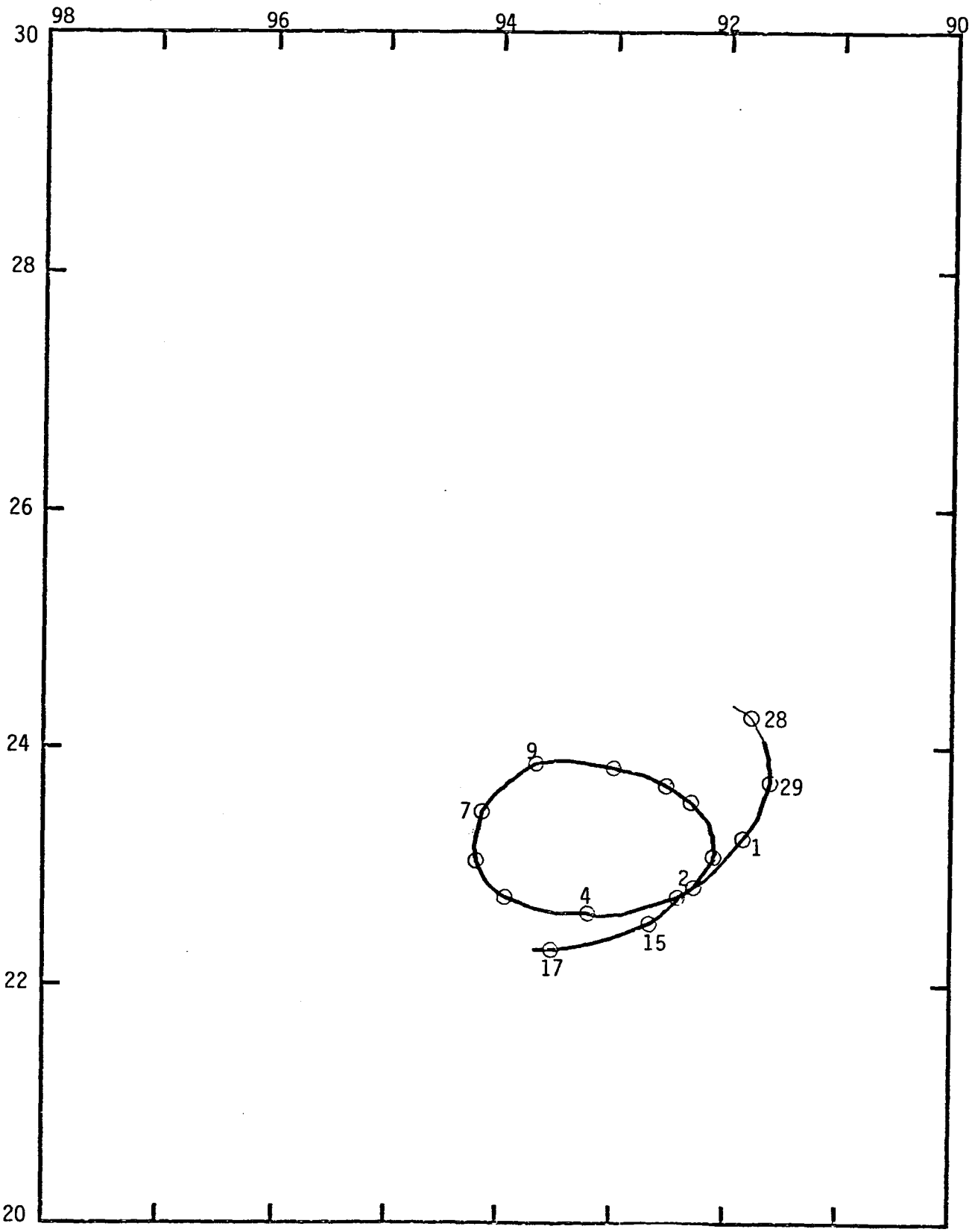

Fig. 2c. Buoy 1598 trajectory 27 Dec 80 - 17 Jan 81. The trajectories begin with the thin line and the circles correspond to position nearest to 0000 hrs (no circles on 30, 31 Dec 80 and 3, 8, 16 Jan 81). Scales are longitude and latitude.

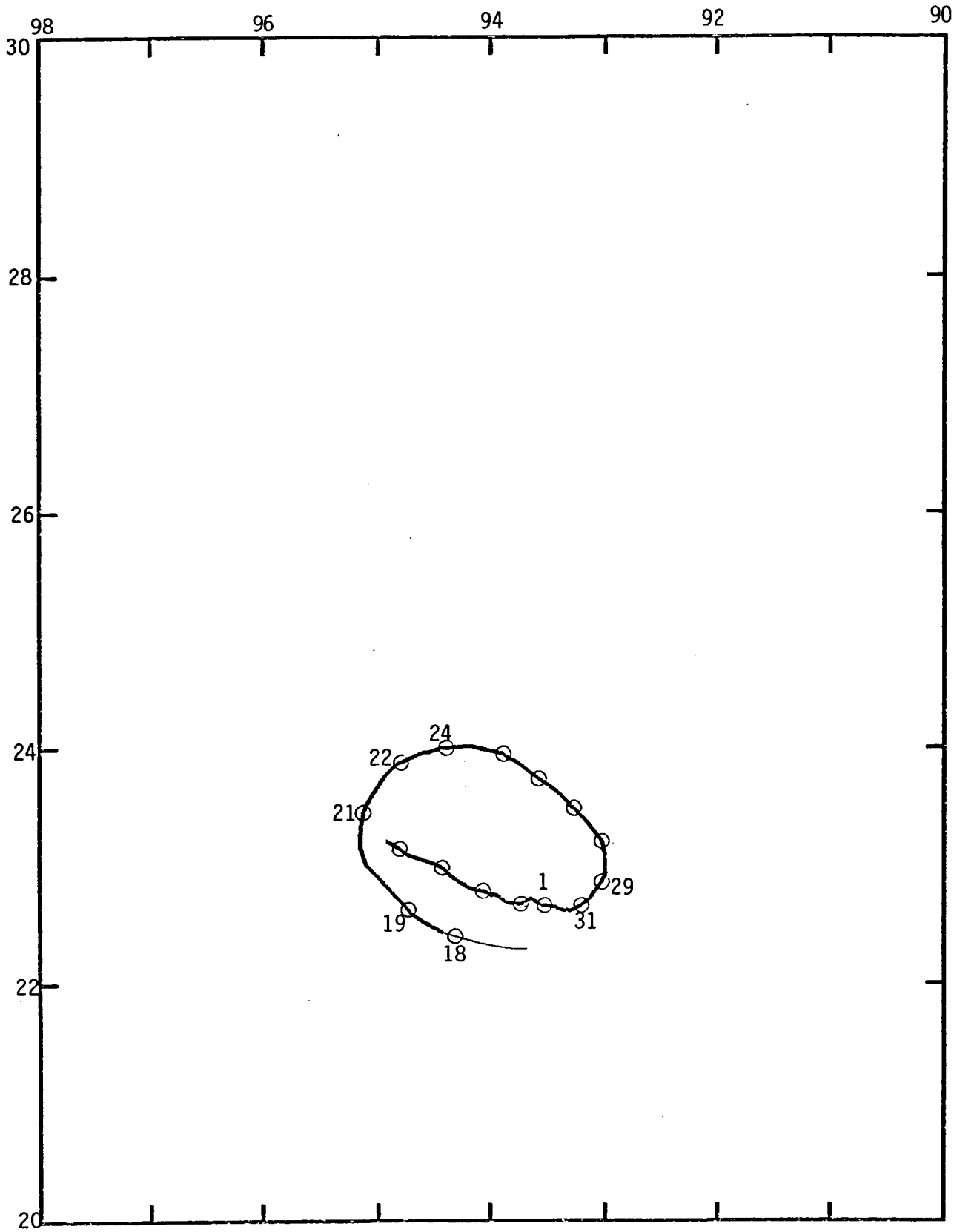

Fig. 2d. Buoy 1598 trajectory 17 Jan 81 - 5 Feb 81. The trajectories begin with the thin line and the circles correspond to position nearest to 0000 hrs (no circles on 20, 23 Jan). Scales are longitude and latitude.

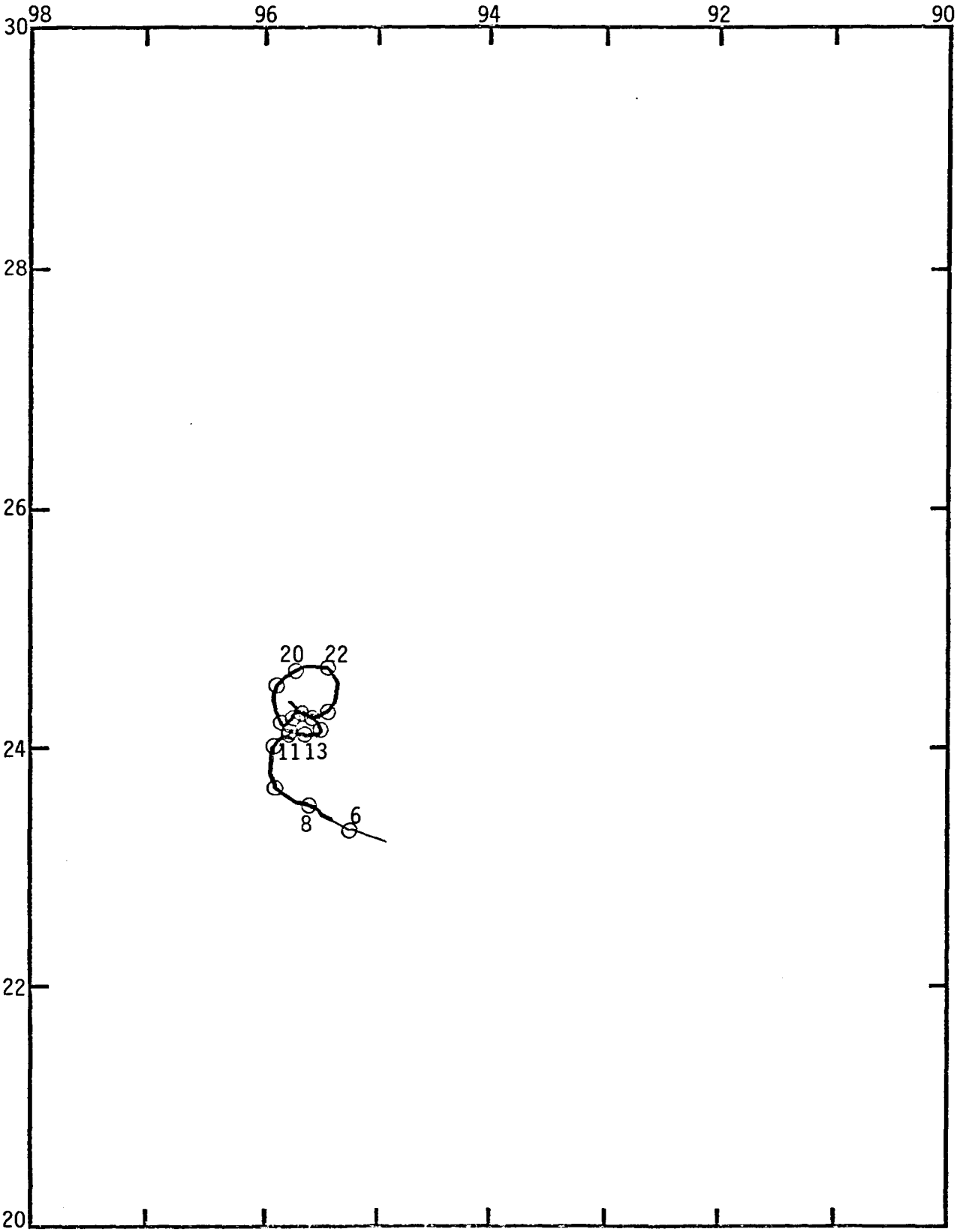

Fig. 2e. Buoy 1598 trajectory 5 Feb 81 - 24 Feb 81. The trajectories begin with the thin line and the circles correspond to position nearest to 0000 hrs (no circles on 7, 12 and 21 Feb). Scales are longitude and latitude.

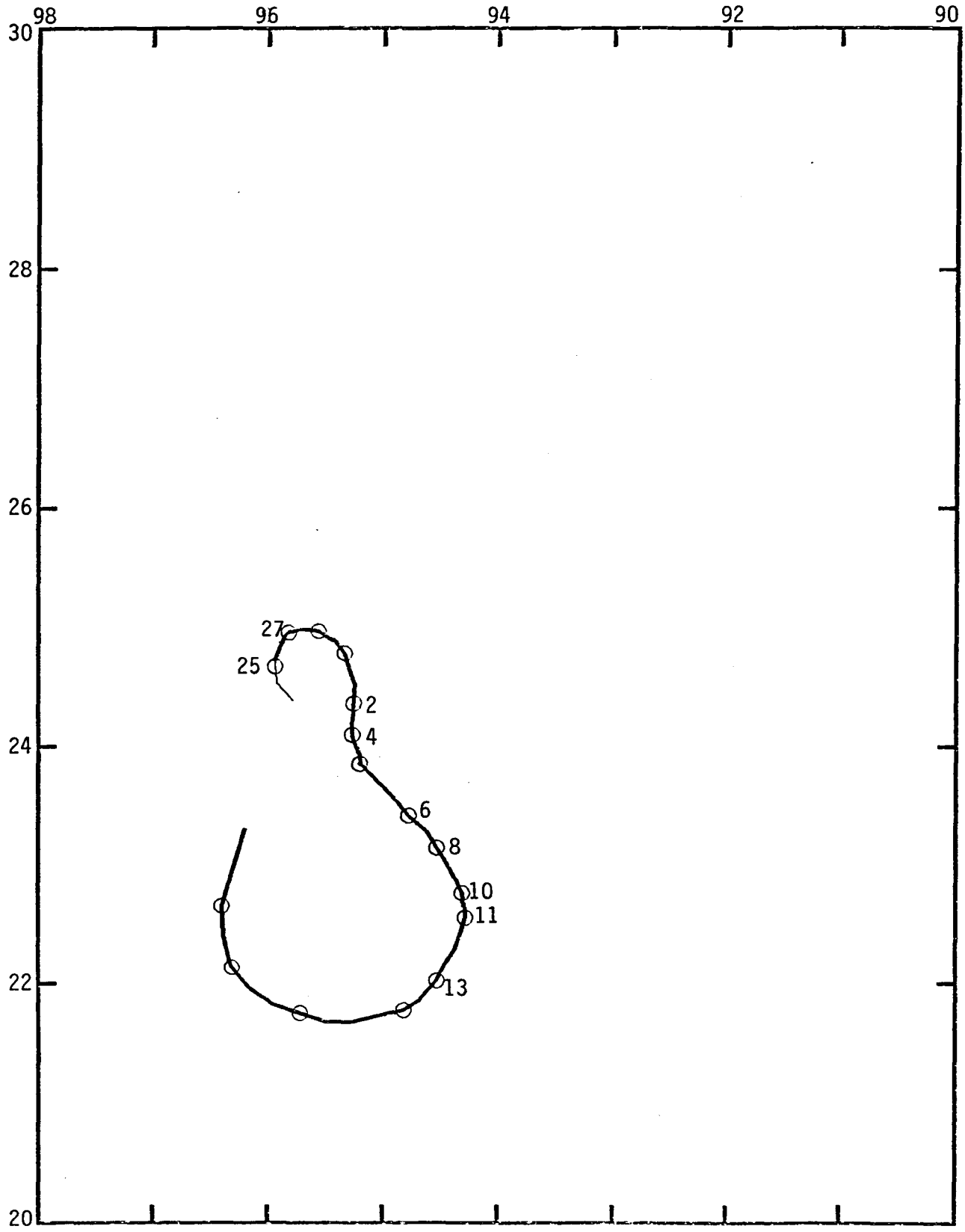

Fig. 2f. Buoy 1598 trajectory 24 Feb 81 - 18 Mar 81. The trajectories begin with the thin line and the circles correspond to position nearest to 0000 hrs (no circles on 26 Feb, 3, 7 and 9 Mar). Scales are longitude and latitude.

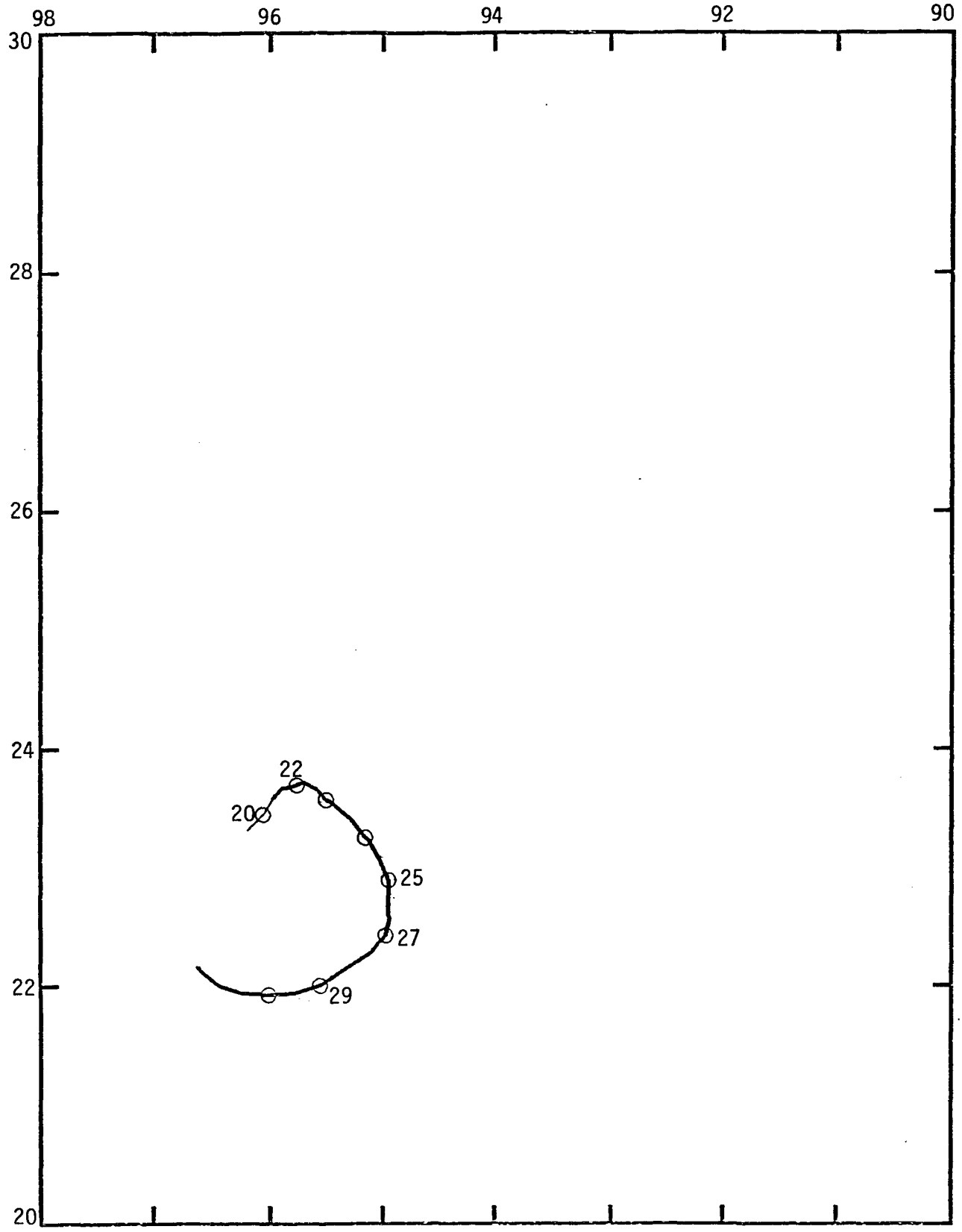

Fig. 2g. Buoy 1598 trajectory 20 Mar 81 - 31 Mar 81. The trajectories begin with the thin line and the circles correspond to position nearest to 0000 hrs (no circles on 21, 26, 28 Mar). Scales are longitude and latitude.

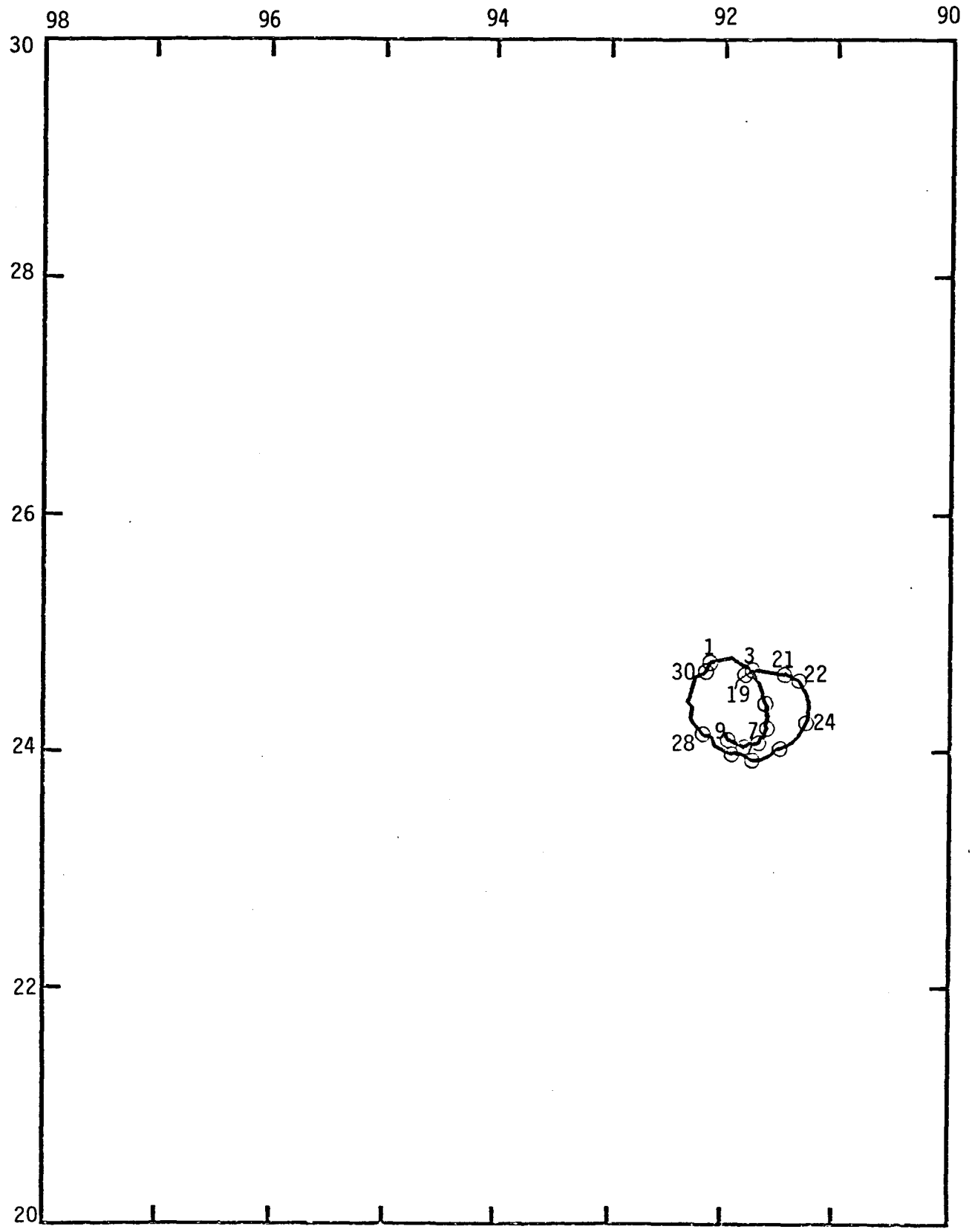

Fig. 3a. Buoy 1599 trajectory 19 Nov 80 - 9 Dec 80. The trajectories begin with the thin line and the circles correspond to position nearest to 0000 hrs (no circles on 20, 23, 29 Nov and 2, 8 Dec). Scales are longitude and latitude.

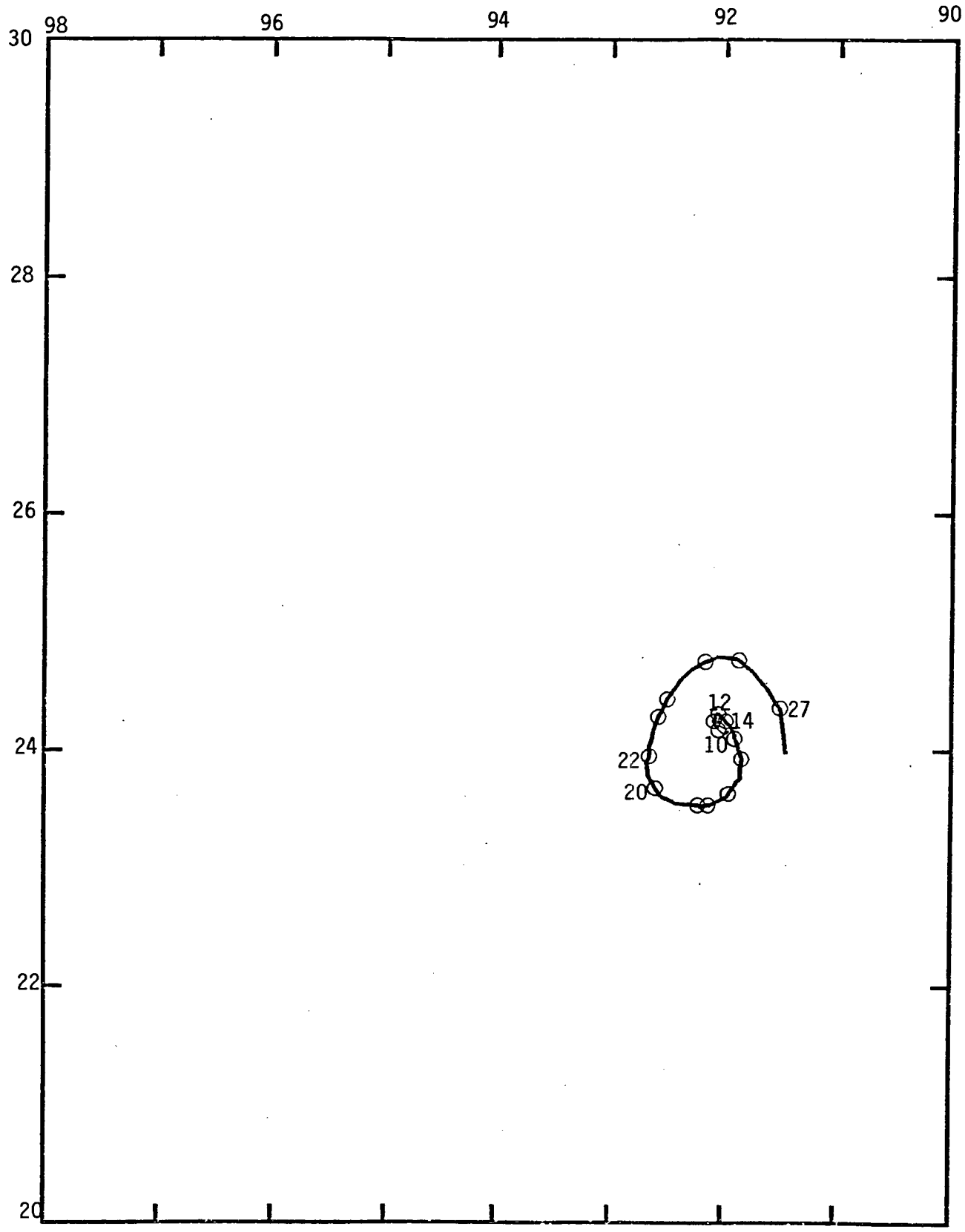

Fig. 3b. Buoy 1599 trajectory 10 Dec 80 - 27 Dec 80. The trajectories begin with the thin line and the circles correspond to position nearest to 0000 hrs (no circles 13 and 21 Dec). Scales are longitude and latitude.

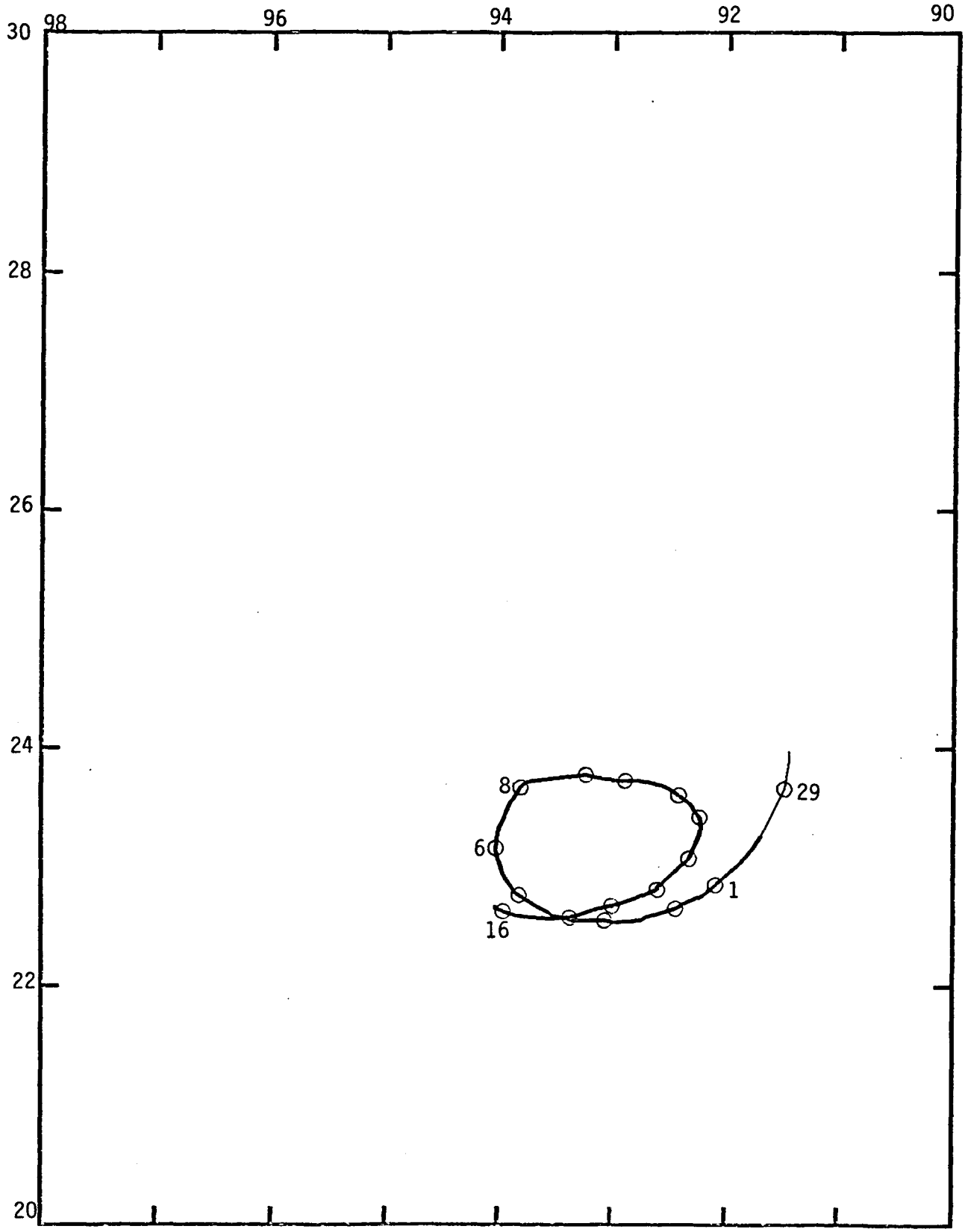

Fig. 3c. Buoy 1599 trajectory 28 Dec 80 - 16 Jan 81. The trajectories begin with the thin line and the circles correspond to position nearest to 0000 hrs (no circles 30, 31 Dec 80 and 7 Jan 81). Scales are longitude and latitude.

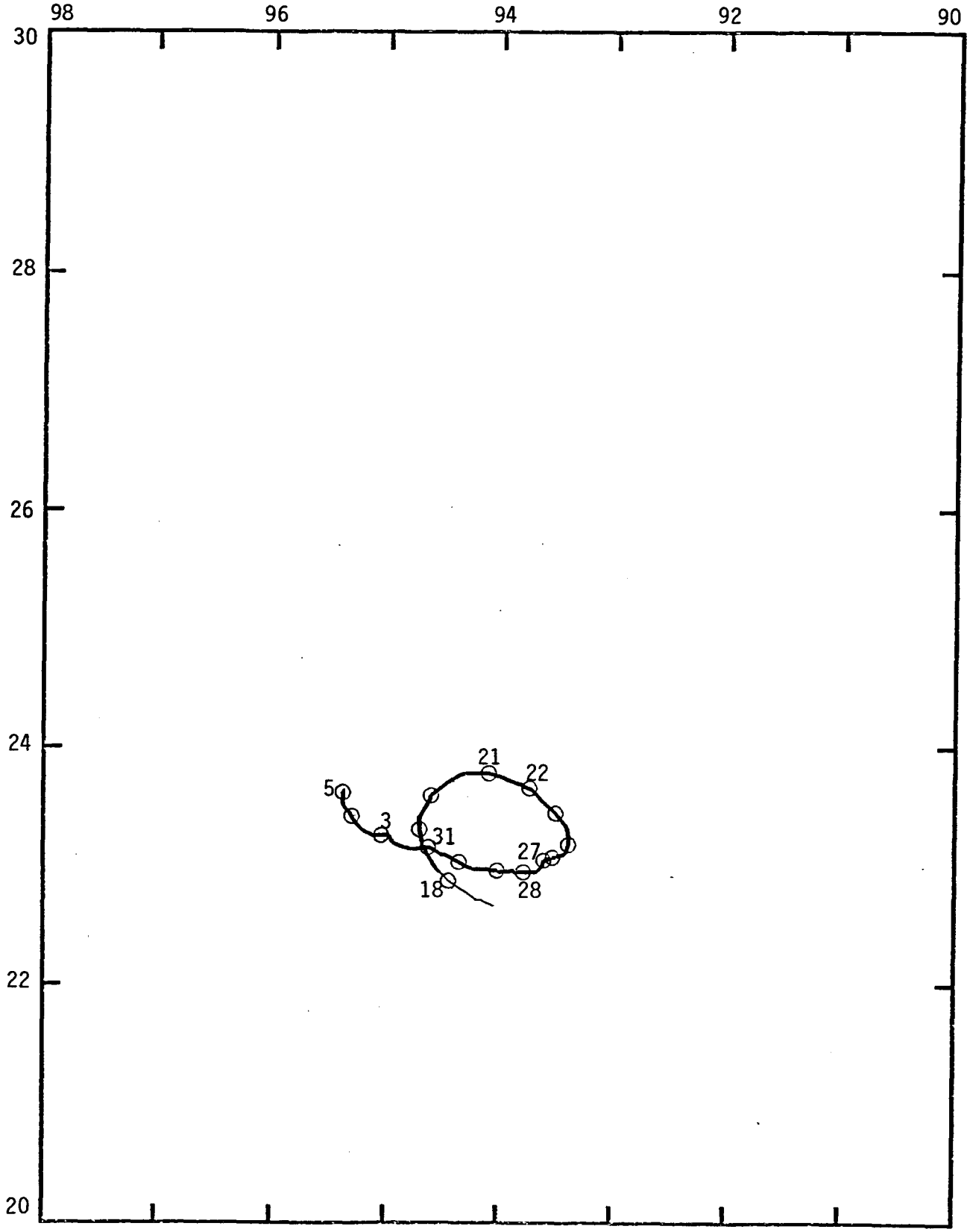

Fig. 3d. Buoy 1599 trajectory 17 Jan 81 - 5 Feb 81. The trajectories begin with the thin line and the circles correspond to position nearest to 0000 hrs (no circles 23, 28 Jan and 1 Feb). Scales are longitude and latitude.

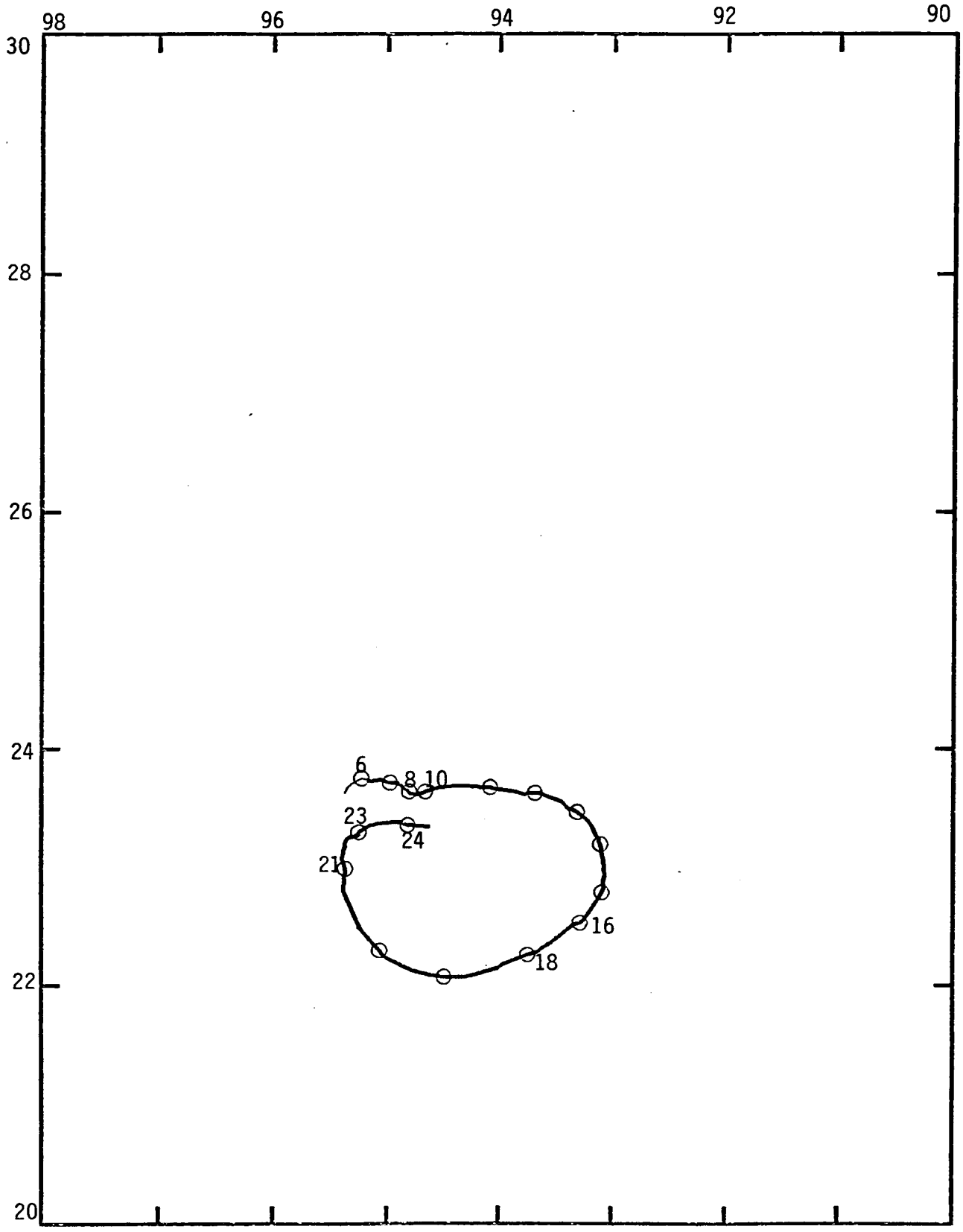

Fig. 3e. Buoy 1599 trajectory 5 Feb 81 - 24 Feb 81. The trajectories begin with the thin line and the circles correspond to position nearest to 0000 hrs (no circles 9, 17, 22 Feb). Scales are longitude and latitude.

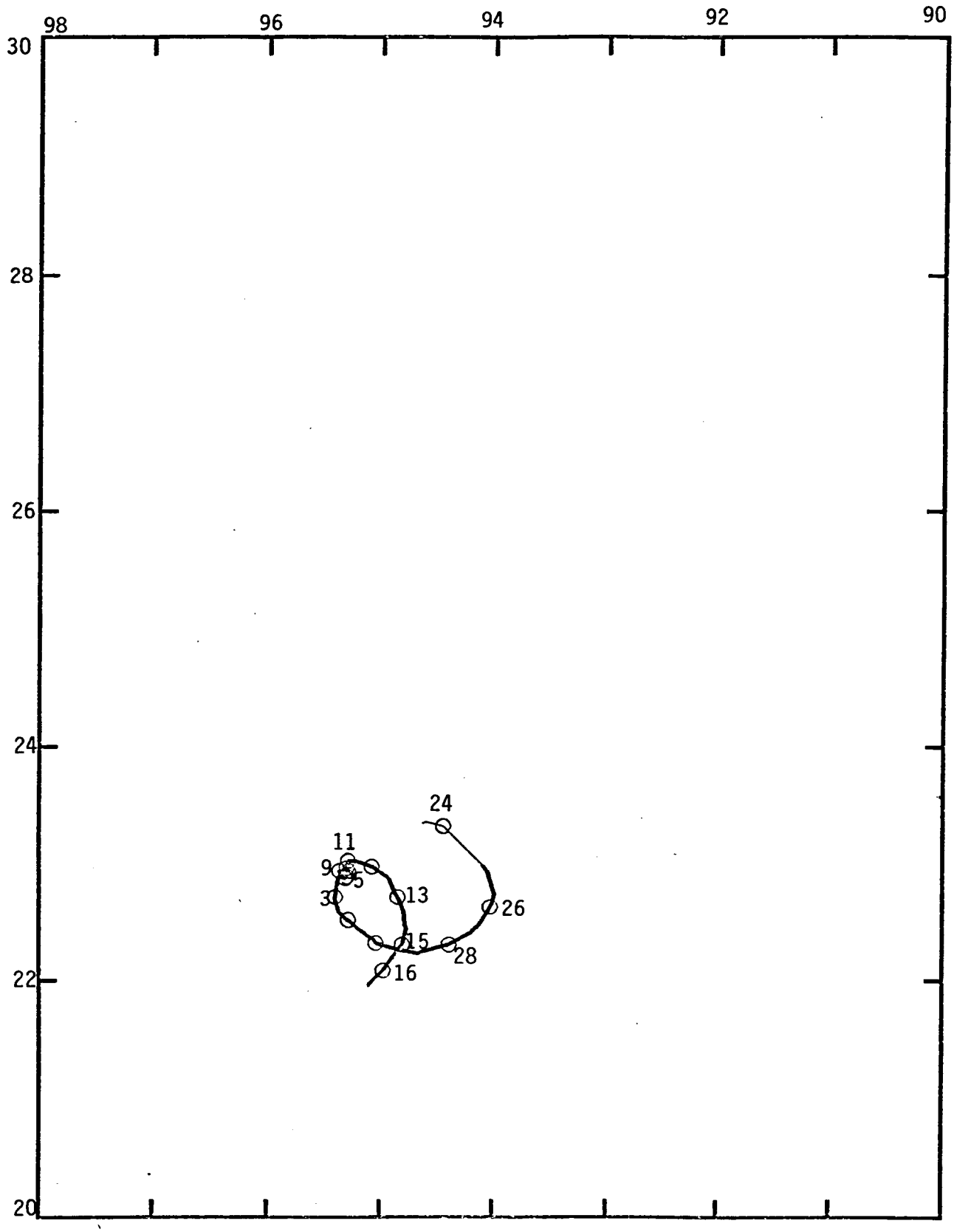

Fig. 3f. Buoy 1599 trajectory 24 Feb 81 - 16 Mar 81. The trajectories begin with the thin line and the circles correspond to position nearest to 0000 hrs (no circles 25, 27 Feb and 1, 10, 14 Mar). Scales are longitude and latitude.

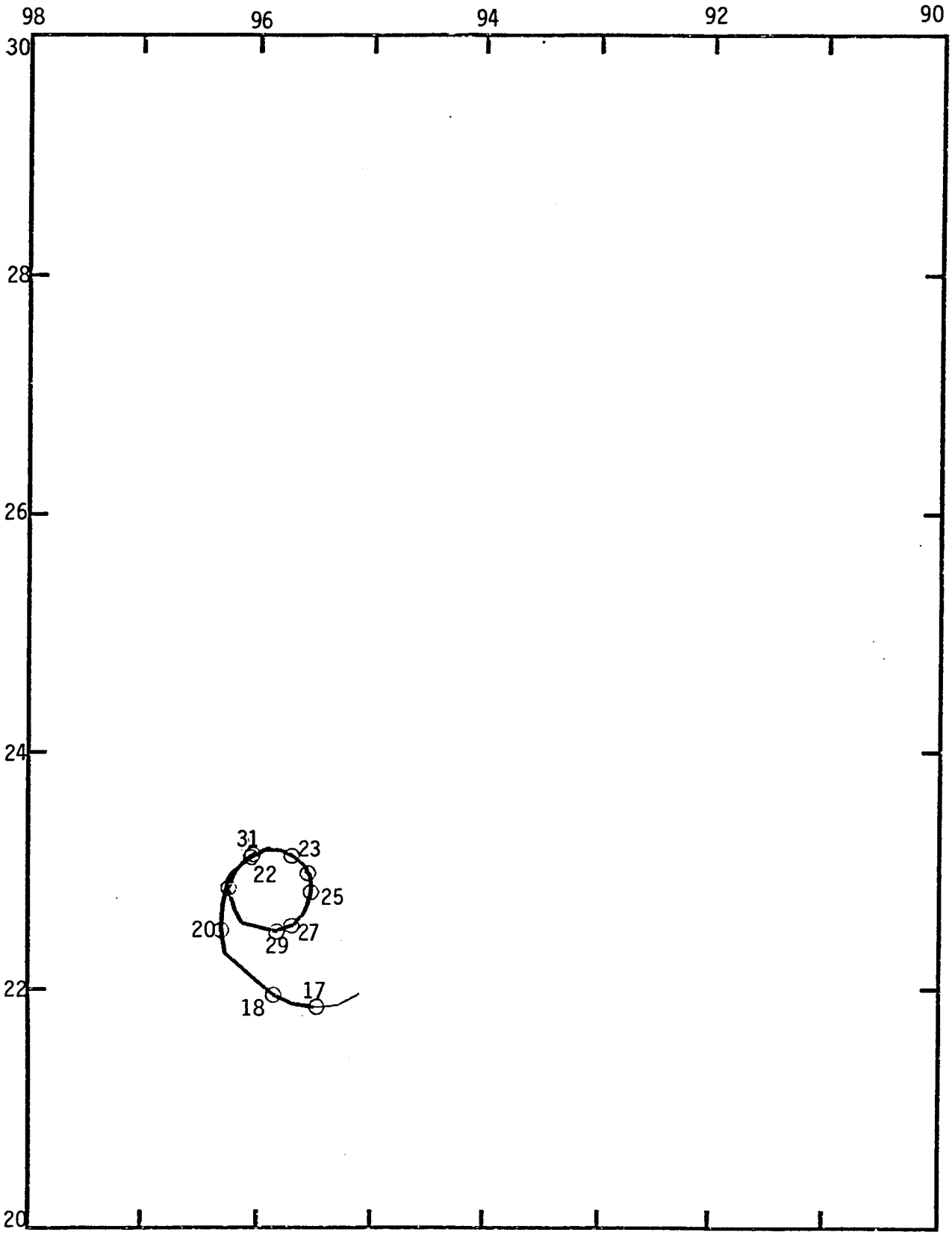

Fig. 3g. Buoy 1599 trajectory 17 Mar 81 - 31 Mar 81. The trajectories begin with the thin line and the circles correspond to position nearest to 0000 hrs (no circles on 19, 21, 26 Mar). Scales are longitude and latitude.

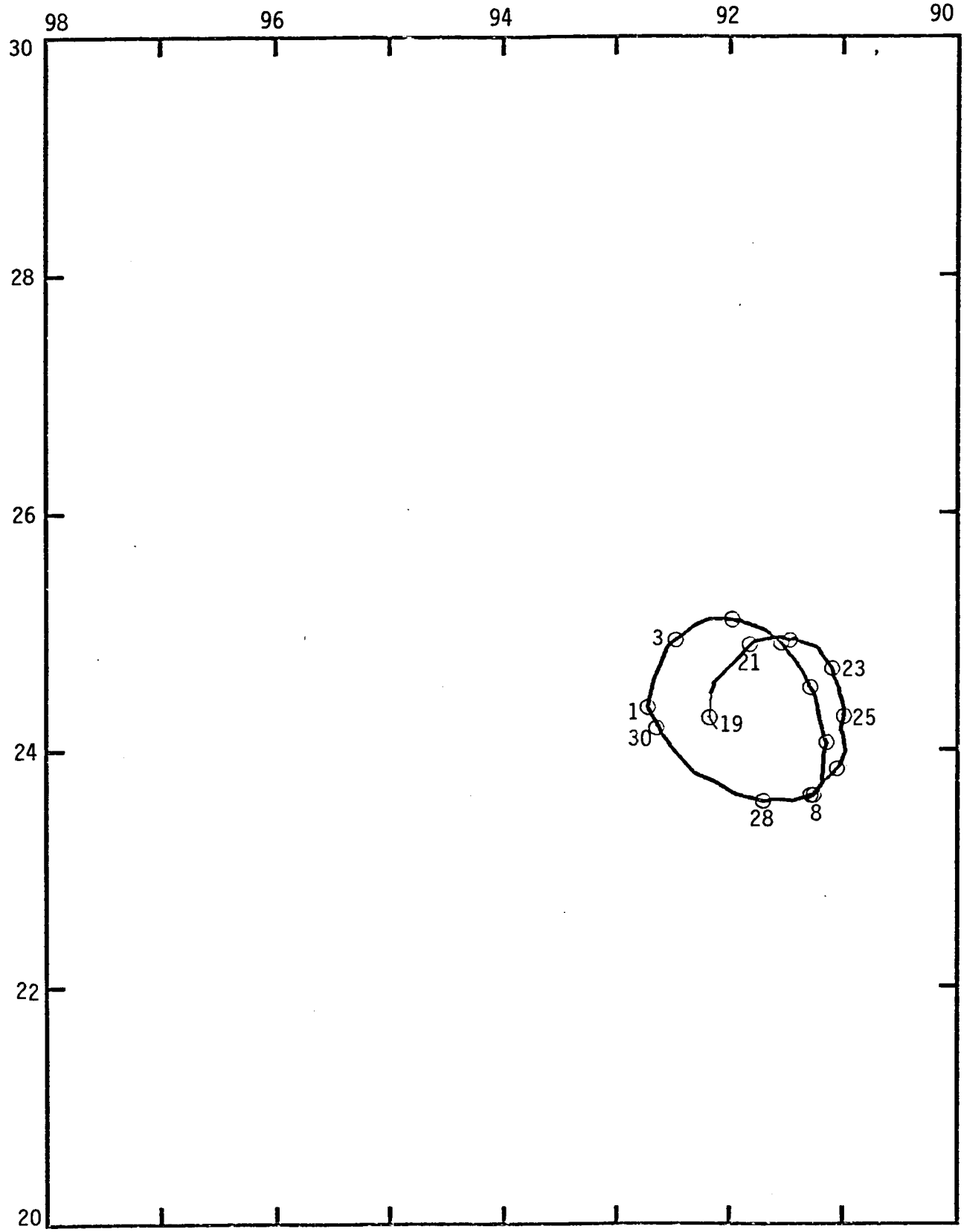

Fig. 4a. Buoy 1600 trajectory 19 Nov 80 - 8 Dec 80. The trajectories begin with the thin line and the circles correspond to position nearest to 0000 hrs (no circles on 20, 24, 29 Nov and 2 Dec). Scales are longitude and latitude.

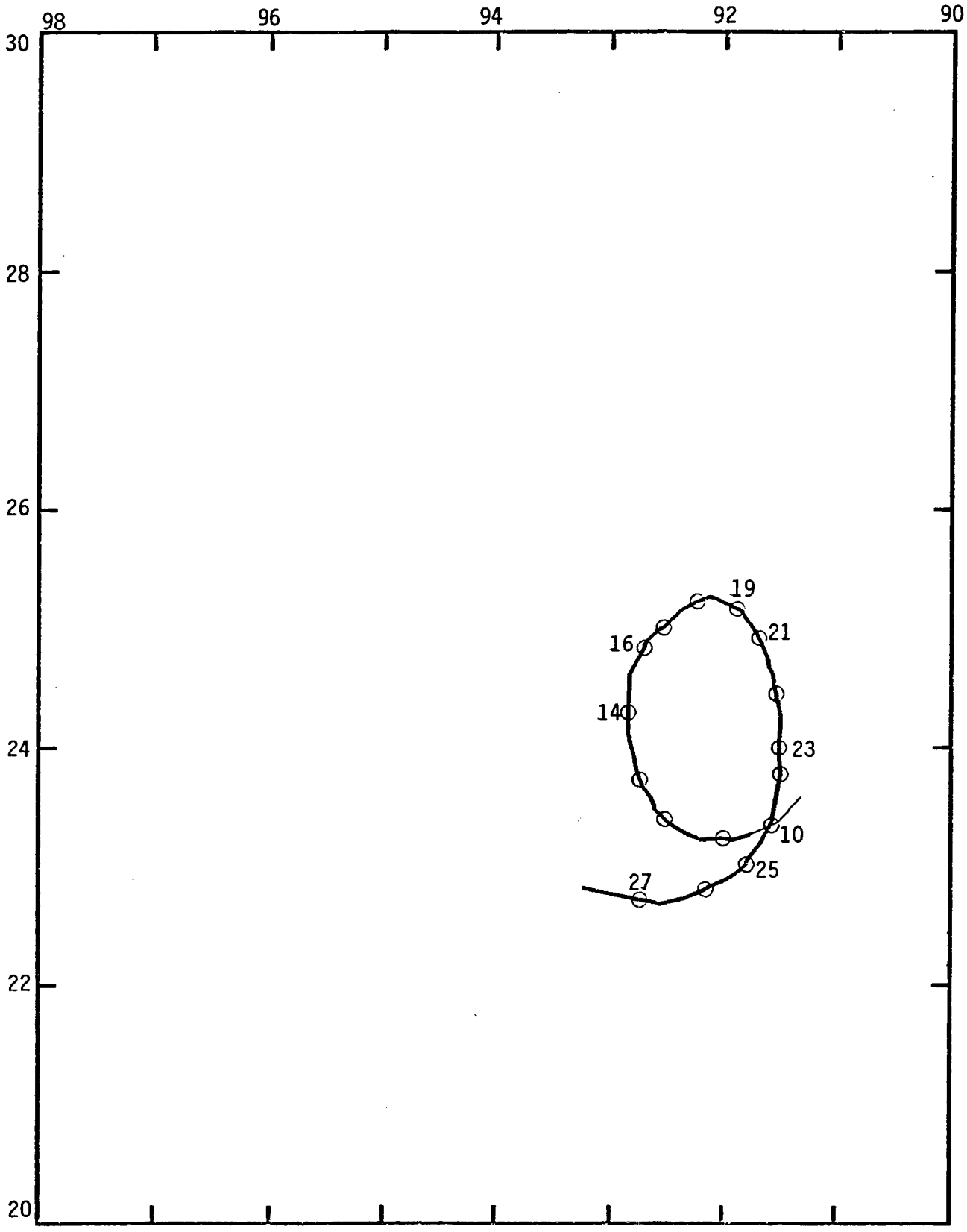

Fig. 4b. Buoy 1600 trajectory 9 Dec 80 - 27 Dec 80. The trajectories begin with the thin line and the circles correspond to position nearest to 0000 hrs (no circles on 15 and 20 Dec). Scales are longitude and latitude.

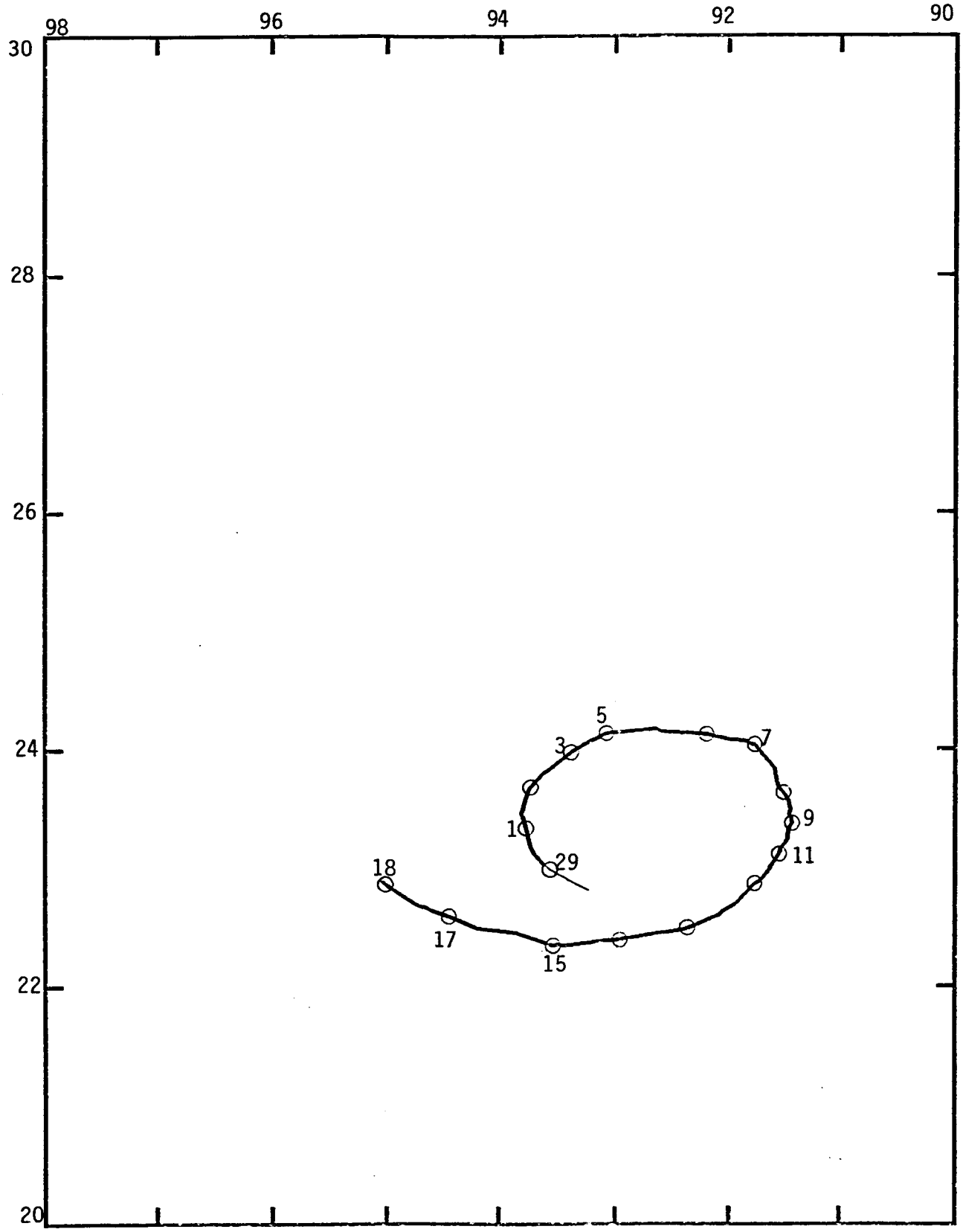

Fig. 4c. Buoy 1600 trajectory 28 Dec 80 - 18 Jan 81. The trajectories begin with the thin line and the circles correspond to position nearest to 0000 hrs (no circles on 30, 31 Dec 80 and 4, 10, 16 Jan 81). Scales are longitude and latitude.

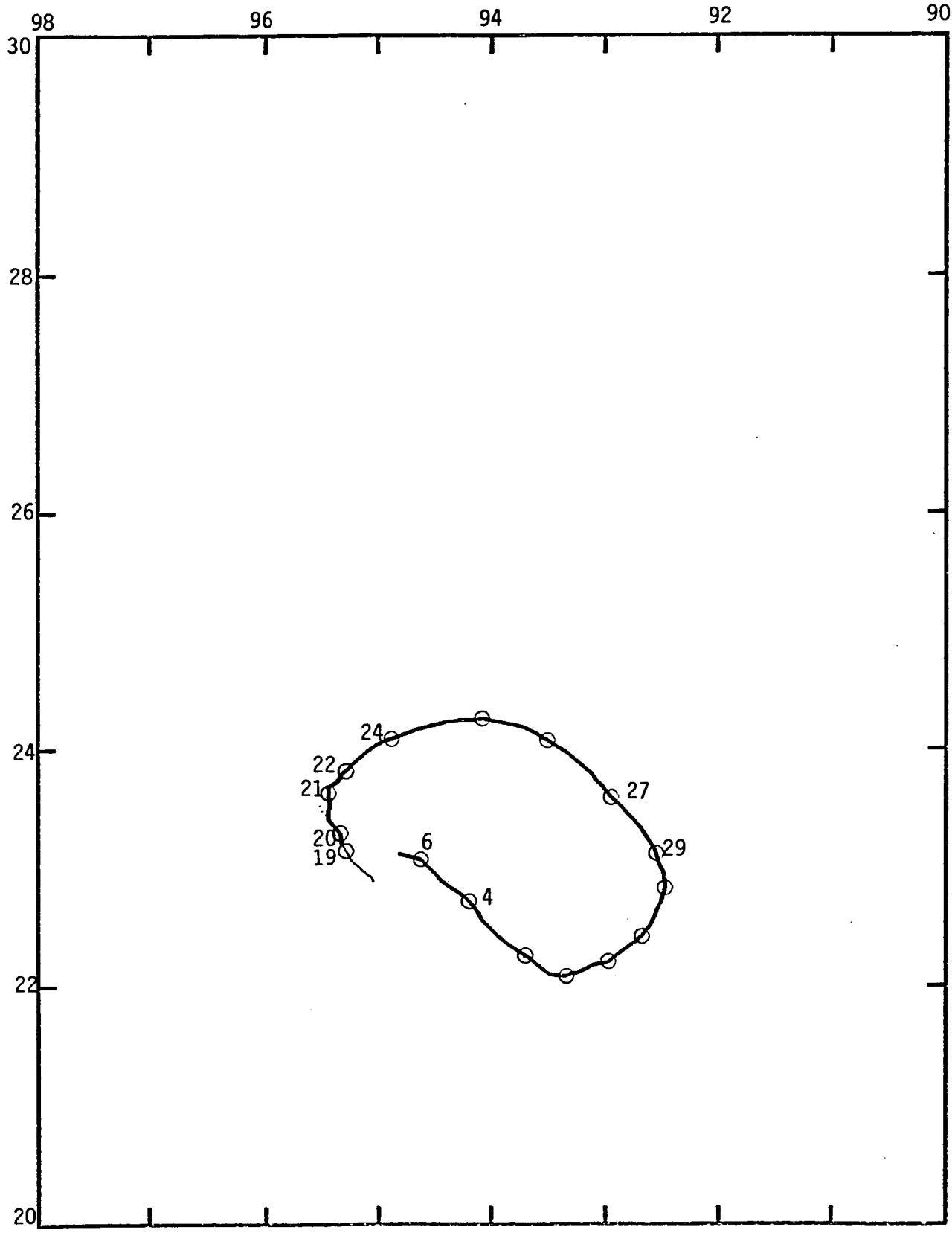

Fig. 4d. Buoy 1600 trajectory 18 Jan 81 - 6 Feb 81. The trajectories begin with the thin line and the circles correspond to position nearest to 0000 hrs (no circles on 23, 28 Jan and 5 Feb). Scales are longitude and latitude.

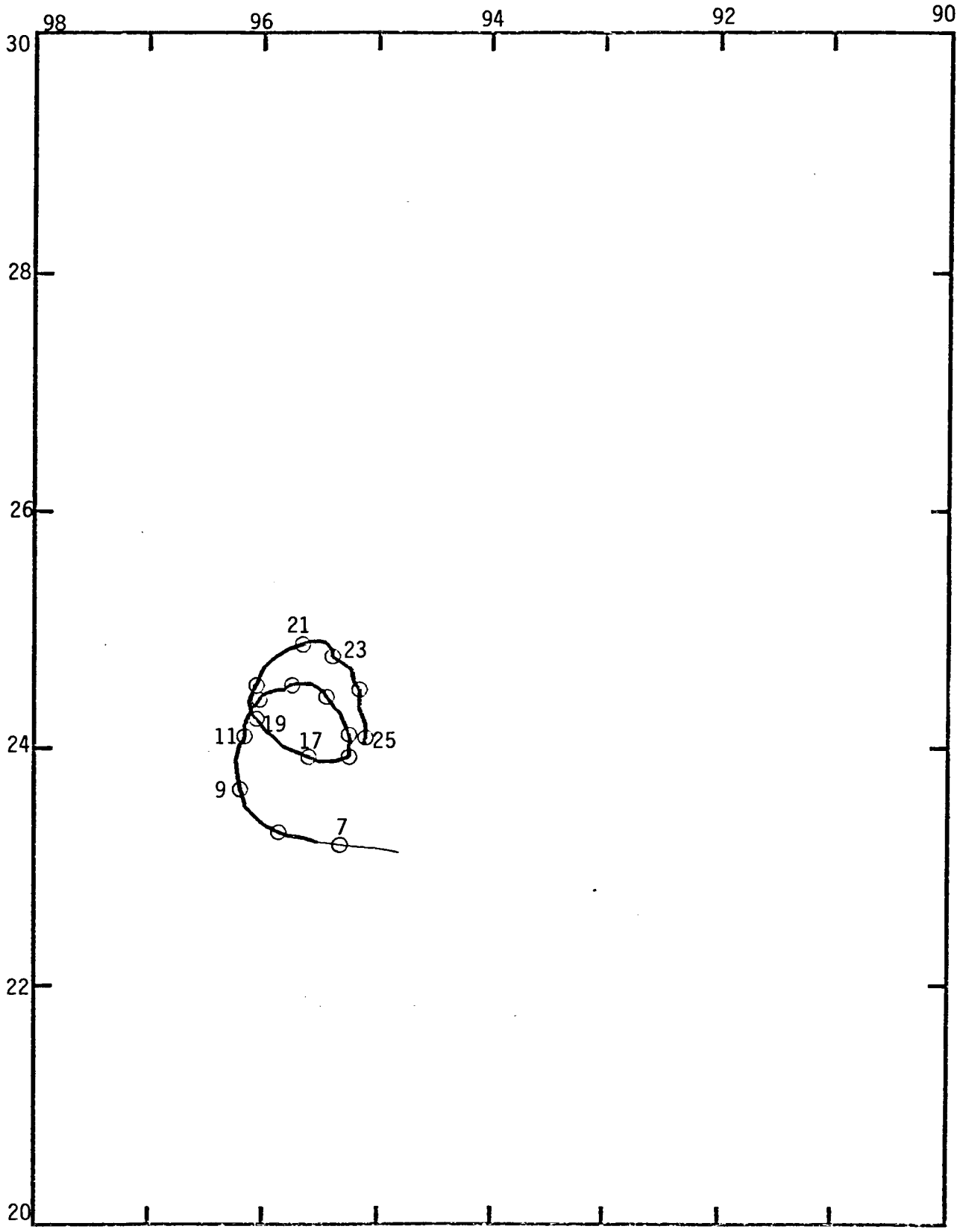

Fig. 4e. Buoy 1600 trajectory 6 Feb 81 - 25 Feb 81. The trajectories begin with the thin line and the circles correspond to position nearest to 0000 hrs (no circles on 10, 18 and 22 Feb). Scales are longitude and latitude.

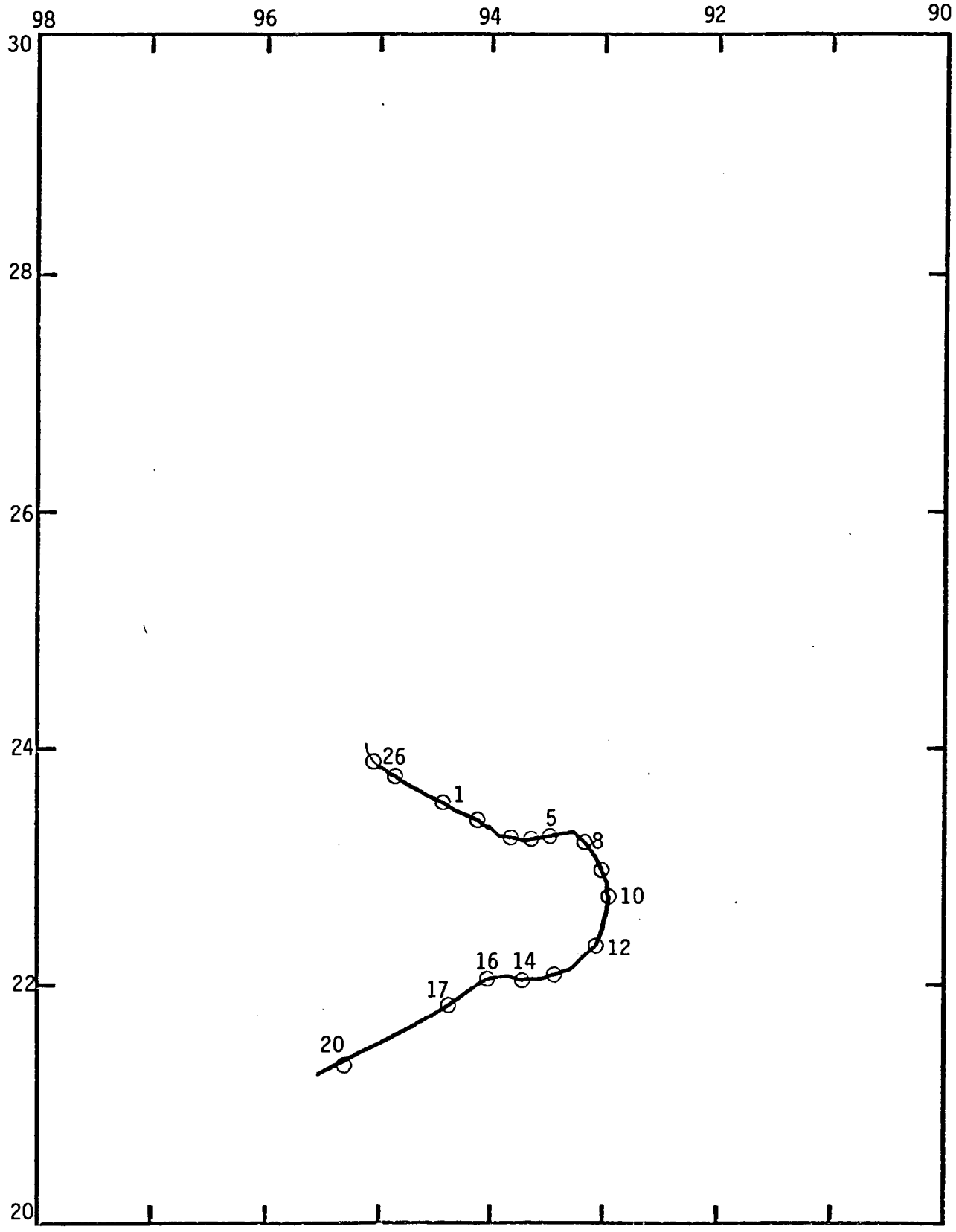

Fig. 4f. Buoy 1600 trajectory 25 Feb 81 - 20 Mar 81. The trajectories begin with the thin line and the circles correspond to position nearest to 0000 hrs (no circles on 28 Feb and 6, 7, 11, 15, 18, 19 Mar). Scales are longitude and latitude.

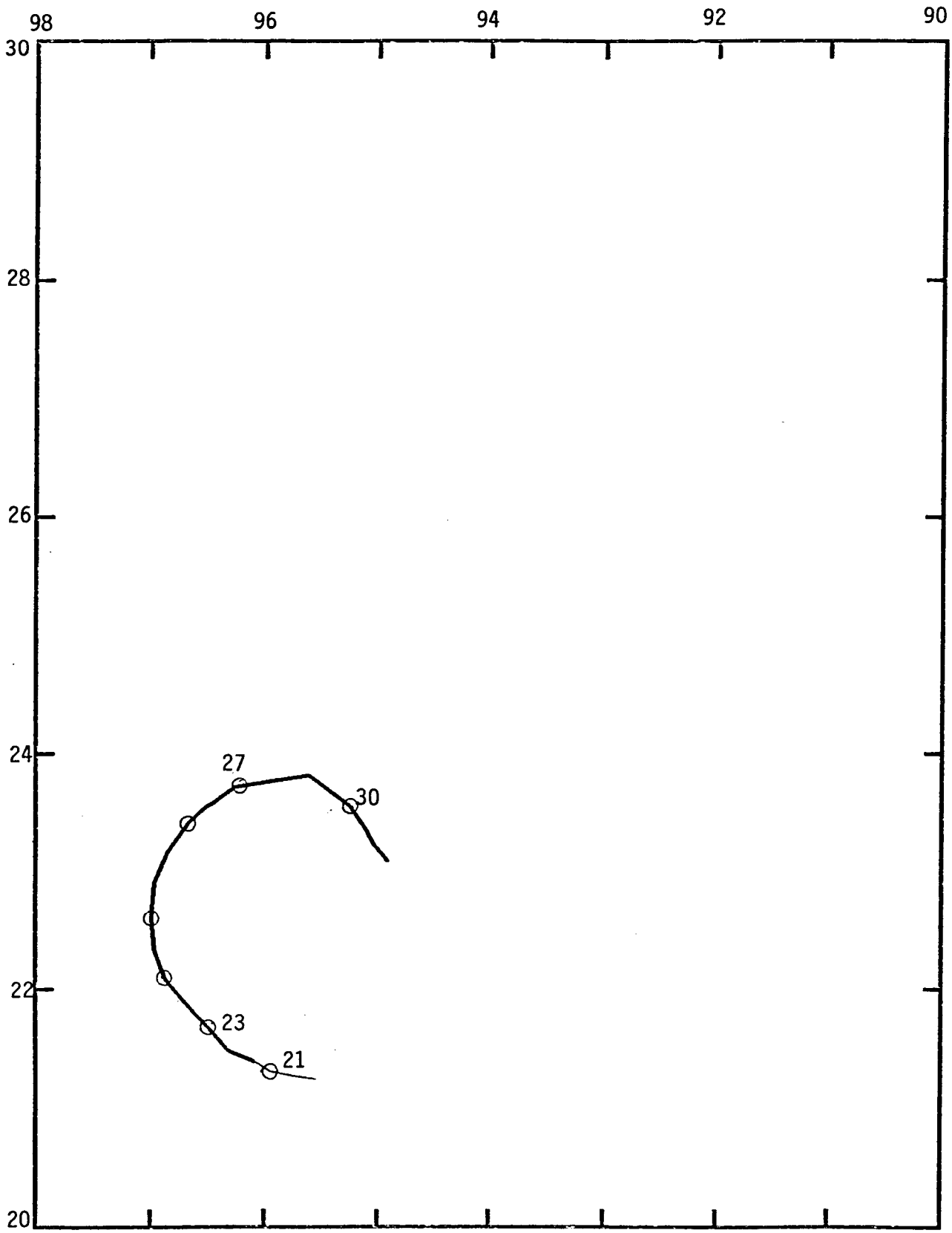

Fig. 4g. Buoy 1600 trajectory 20 Mar 81 - 30 Mar 81. The trajectories begin with the thin line and the circles correspond to position nearest to 0000 hrs (no circles on 22, 28, 29 Mar). Scales are longitude and latitude.

panels), 1598 apparently migrated to a greater distance from the ring center than 1599. The paths of both of these drifters show some northward translation of the ring. This is not inconsistent with the path of 1600; however, the ring translation effect on its path is considerably less relative to the swirl velocity. From 27 December 1980 through 17 January 1981, all three paths suggest some westward translation and some ring ellipticity with an east-west orientation. The (d) panels (17 January - 5 February) show that the paths for the three drifters form concentric ellipses with the major axis toward the WNW. The next 15 days show some inconsistencies in the paths. The (3) panels (5 February - 24 February) show 1598 and 1600 with a northern translation and 1599 with some southern movement. ID 1598 is still inside the path of 1600. Also, the small loop of 1598 near the end of the month suggests that its swirl velocity is close to the translation velocity. The (f) panels (21 February - 18 March) show that 1598 and 1600 turned back to the south in close vicinity of 1599. ID 1600 showed a curious eastward migration which was not seen in the other two drifters. The last panel shows the paths from 20 March - 30 March. These show three nearly concentric circular features.

There is remarkable consistency between the three drifter paths. ID's 1598 and 1599 were first located nearer the ring center than 1600. During the nearly 100 days of paths shown in Figure 2, 1598 moved father away from the ring center than did 1599. Still, in the (g) panels, the locations of the paths relative to the ring center of the three drifters is the same as it was in the (a) panels, over 90 days earlier. This is remarkable for three undrogued

drifters of this type.

4. Raw Absolute Velocity Records

The basic data set used in this study is the trajectory information supplied by NDBO and shown in Figs. 1a, 1b, and 1c in section 3. From this trajectory data set, velocity records for each of the drifters were calculated according to the formulae

$$u(t_k) = R \cos\theta \left[[\psi(t_{k+1}) - \psi(t_k)]/(t_{k+1} - t_k) + [\psi(t_k) - \psi(t_{k-1})]/(t_k - t_{k-1}) \right] /2$$

$$v(t_k) = R \left[[\theta(t_{k+1}) - \theta(t_k)]/(t_{k+1} - t_k) + [\theta(t_k) - \theta(t_{k-1})]/(t_k - t_{k-1}) \right] /2$$

where θ is the latitude and ψ is the longitude. In these last two equations, u and v represent the east and north components of the velocity, respectively. The subscript k for the time variable t refers to the k^{th} time the position of the drifter was observed by the ARGOS satellite. Finally, R is the mean radius of the earth (6371.2 km). These formulae are central finite difference algorithms for the instanteous velocity.

The absolute drifter velocities for buoys 1598, 1599 and 1600 are shown in Figs. 5, 6 and 7, respectively. Three things are apparent in these figures. The first is the large velocities associated with the motion of the ring. Component speeds are of the order of 50 cm/s. Direct measurements of currents this high have not been reported previously in this part of the Gulf of Mexico. The second is the periodic nature in the u and v signals of all three drifters. This arises from the anti-cyclonic motion of the drifters as they rotate in the ring. The third feature is

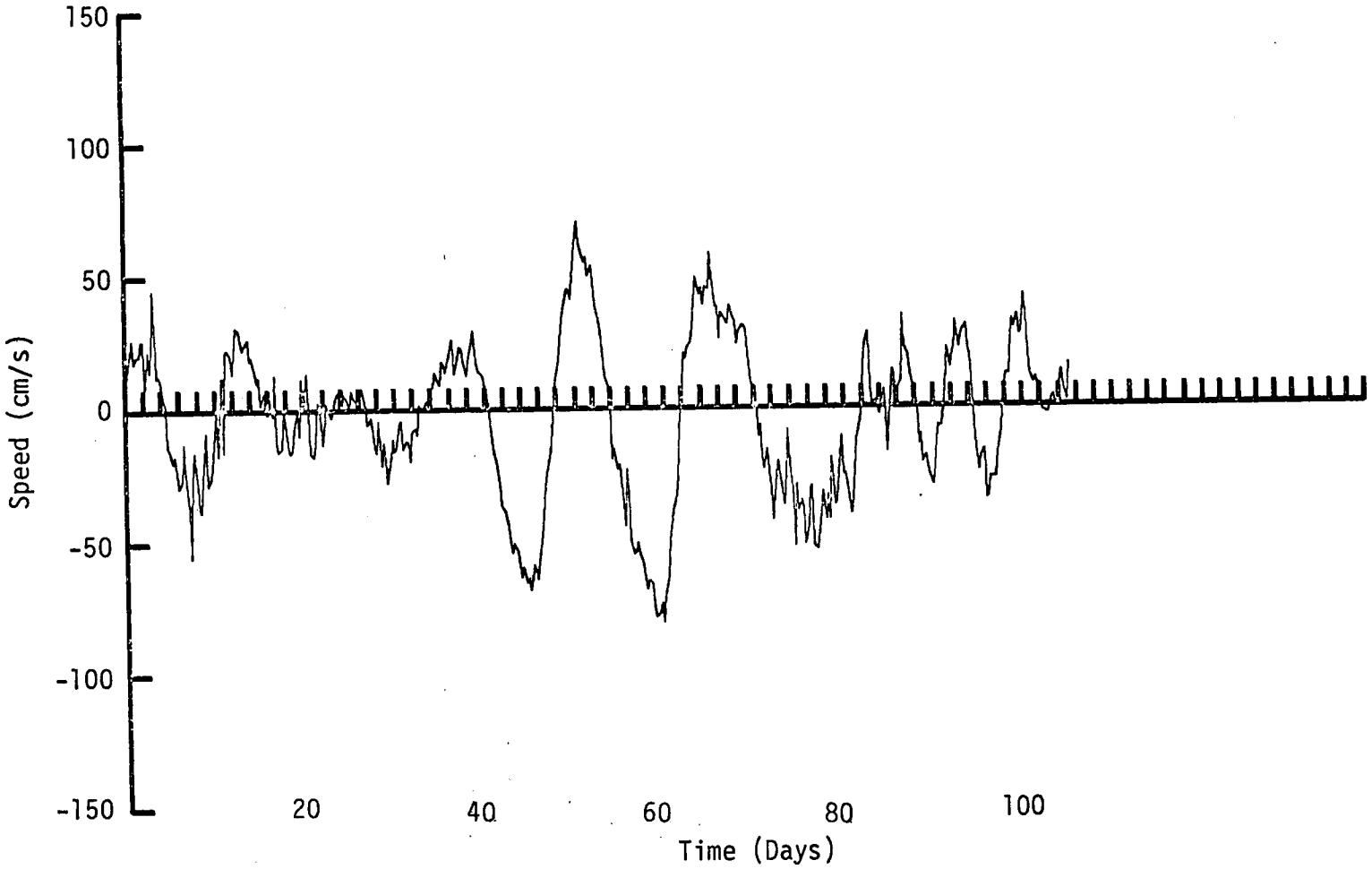

Fig. 5a. The time history of the absolute u velocity component for buoy 1598.

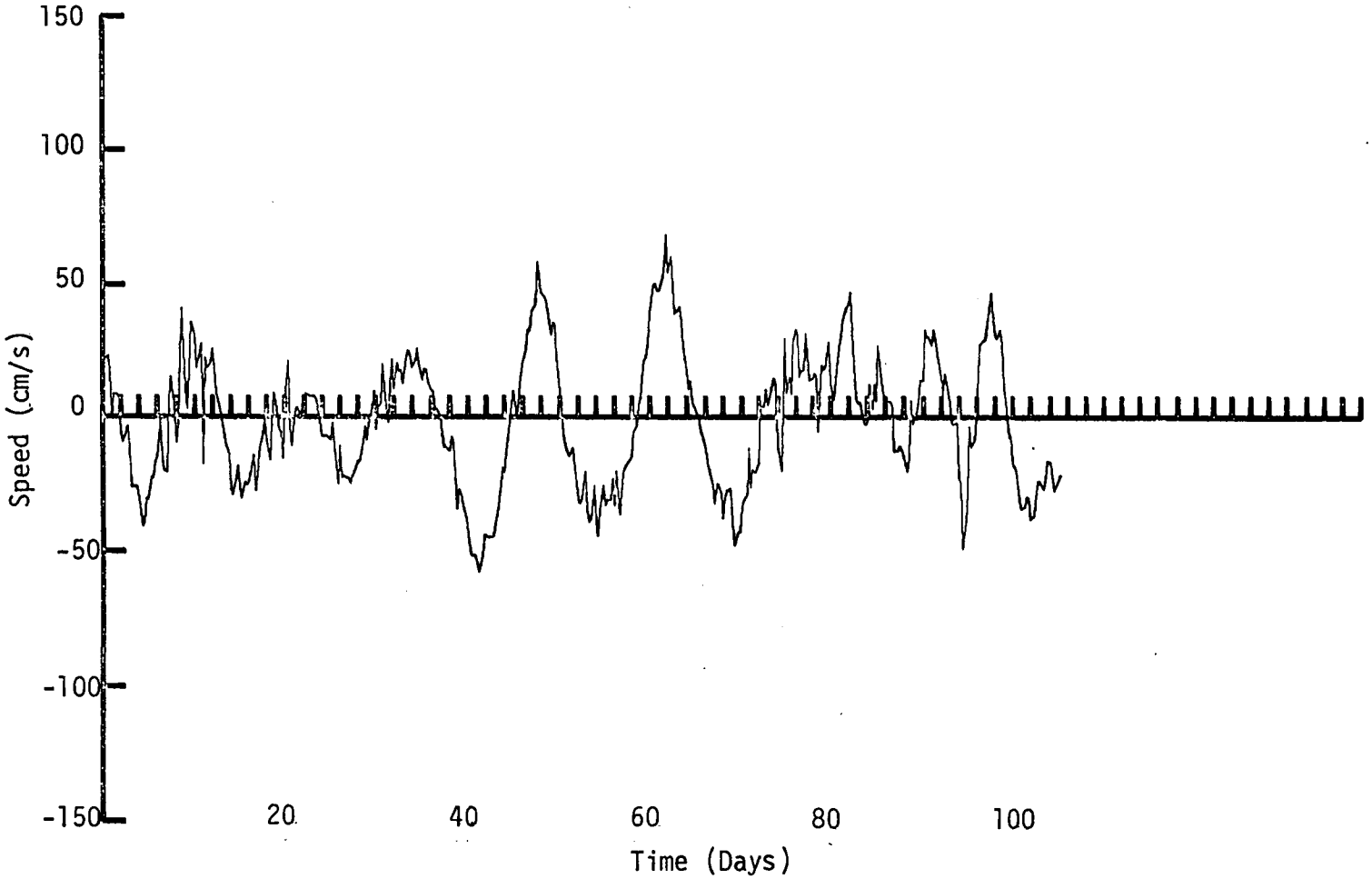

Fig. 5b. The time history of the absolute v velocity component for buoy 1598.

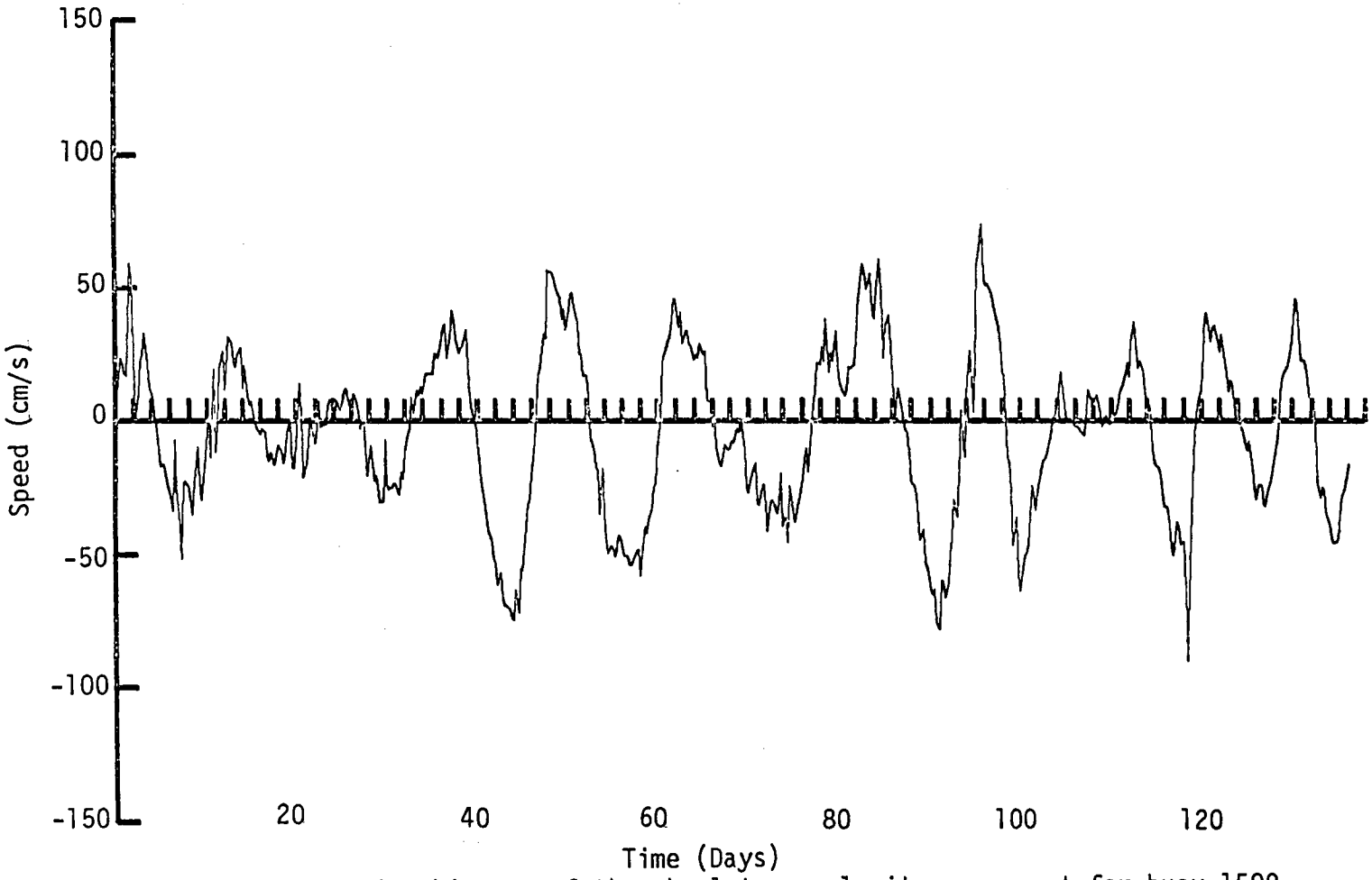

Fig. 6a. The time history of the absolute u velocity component for buoy 1599.

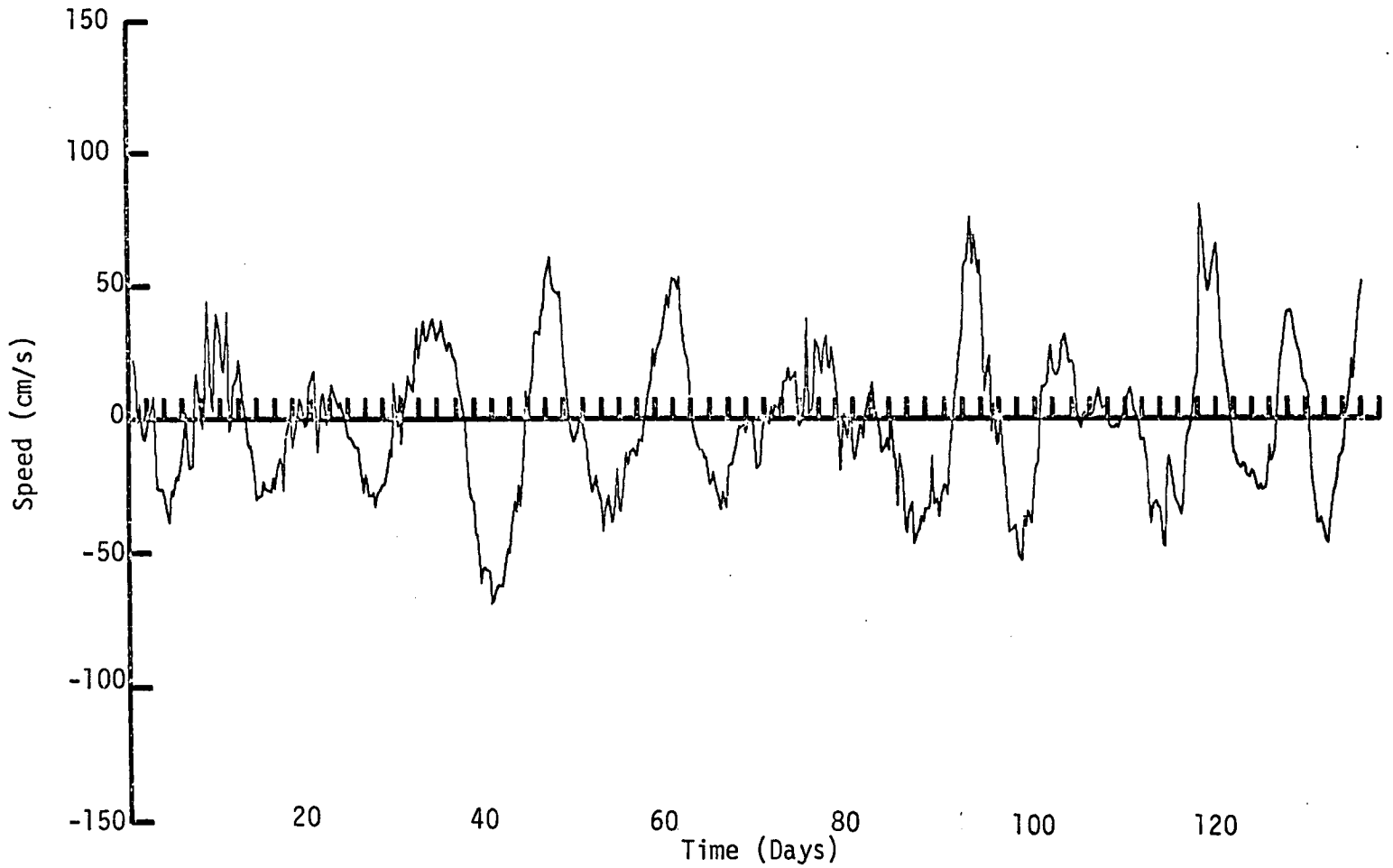

Fig. 6b. The time history of the absolute v velocity component for buoy 1599.

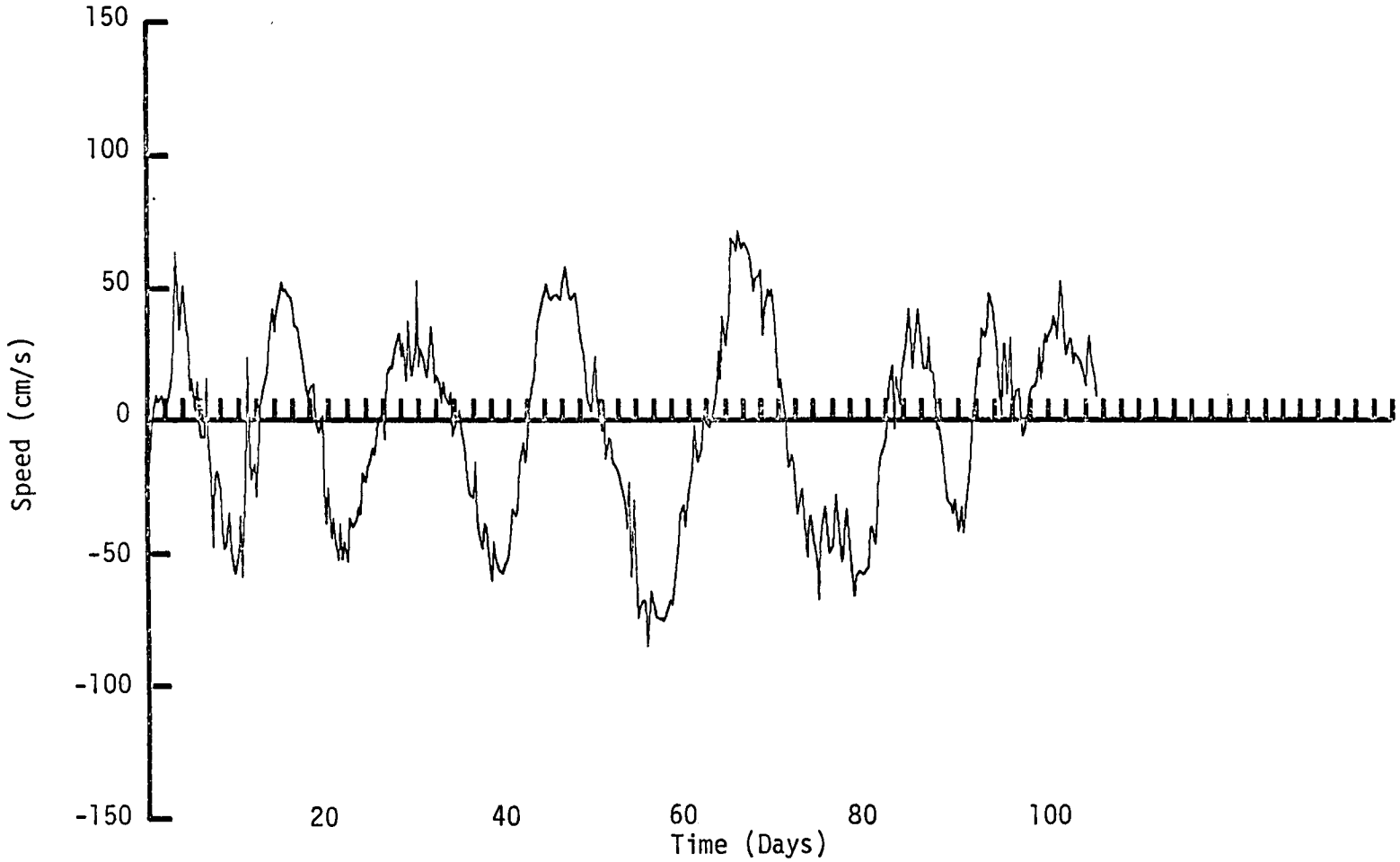

Fig. 7a. The time history of the absolute u velocity component for buoy 1600.

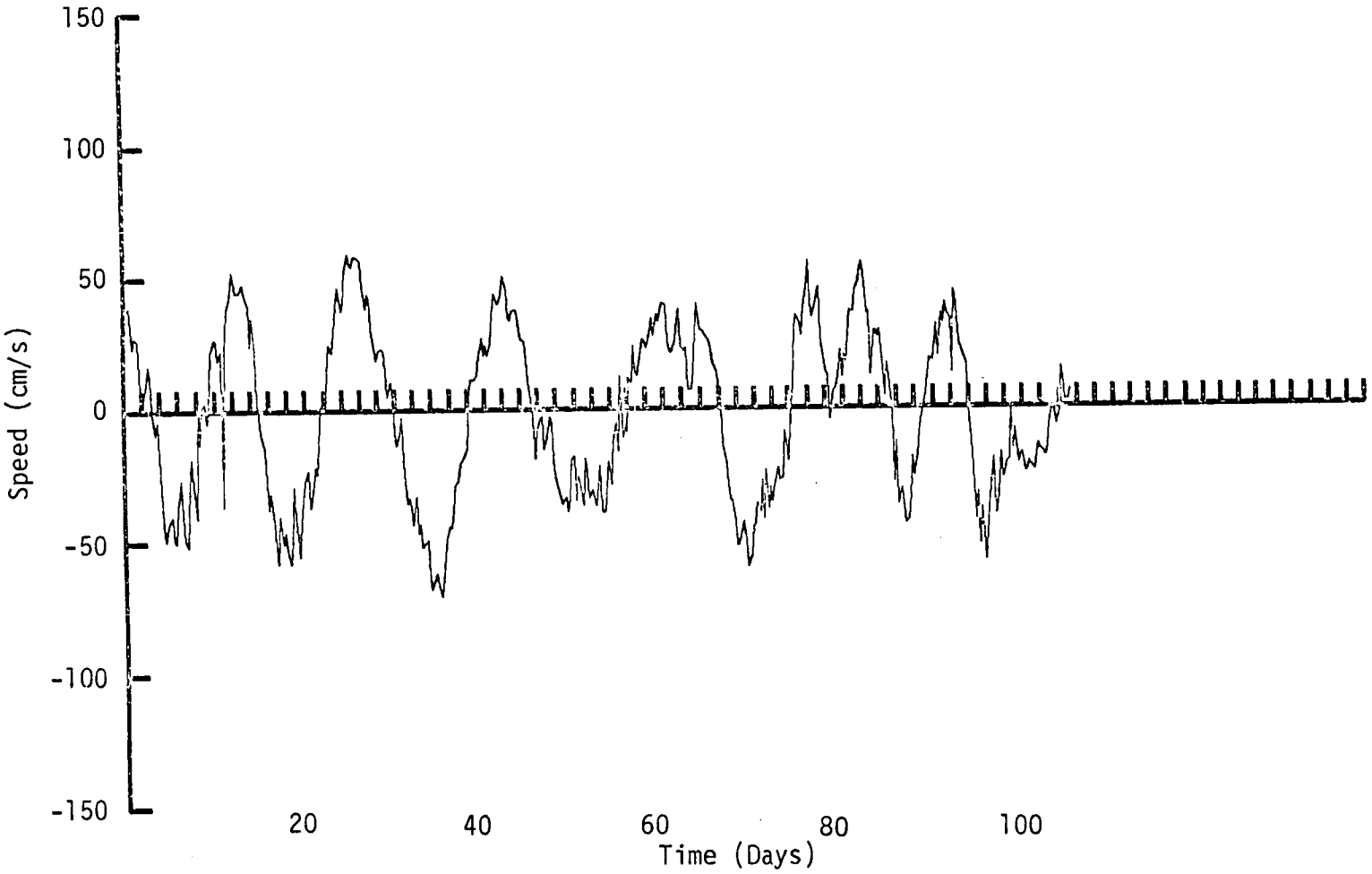

Fig. 7b. The time history of the absolute v velocity component for buoy 1600.

the "high frequency noise", 10 to 20 cm/s, with periods less than 24 hours. This phenomena was completely unexpected. There is no precedent in other velocity observations from the Gulf of Mexico or from other drifter observations that we have worked with.

The primary interest of this study is the lower frequency motion associated with the ring. The amplitudes are of the order of 50 cm/s and the periods are of the order of two weeks. Thus, the presence of the high frequencies in the velocity records produces a classic example of aliasing. Determining the cause of the noise and filtering it out require some special and non-routine analysis which are described in the next section.

5. Analysis of High Frequency Velocity Components

5.1 Background

As indicated in section 4, high frequency noise in the velocity records has aliased the calculations of the DKP. It is important then to identify the cause(s) of the high frequency fluctuations and to remove their effects from the DKP analysis.

To this end, the following sources were considered:

. Slippage resulting from wind and wave action on the buoy.

. Satellite position error resulting in velocity uncertainities.

. Shingles. These are small scale (~10 km) cyclonic features which often develop at the edge of strong fronts. Because of their cyclonic flow characteristics and small scale, they could induce high frequency velocity fluctuations.

. Tides.

. Inertial Oscillations.

Broadly speaking, these sources have distinctive characteristics which conceivably can be determined by spectral analysis. Specifically, slippage should be closely correlated with the local wind field. There is no reason to expect this to produce a consistent sense of rotation.

In practice it may be difficult to document slippage effects with the restricted data base available. This is because strong surface winds may also induce an Ekman response. This, however, is to the right of the surface wind so that there may be some anticyclonic characteristics associated with this.

Position error effects have been studied by G. McNally

of Scripps Institute of Oceanography. He has found (private communication) that the dominant effect is centered in the $8 \cdot 10^{-3}$ cph to 1 cph range. The dominate peak occurs at about $4 \cdot 10^{-2}$ cph with no consistent sense of rotation.

Fluctuations associated with shingles are the least well documented of the candidate source mechanisms. The frequencies are probably of the order of 10^{-2} cph and, in the present case, should exhibit cyclonic rotation.

The dominant tide components in the Gulf of Mexico are diurnal and semi-diurnal. In addition, Reid and Whitaker (1981) have shown that there is a basin tidal resonance at around 30 hrs ($3 \cdot 10^{-2}$ cph) and a less energetic gravity mode at 7 hrs (0.14 cph). The peaks for each of these should be very narrow.

For the Gulf of Mexico, inertial oscillations should have a period of ~28 hours. Also, the sense of rotation is anti-cyclonic. These motions are usually produced by strong winds and frontal passages.

It appears from this discussion that a thorough spectral analysis should indicate which sources are operating and how their effects can be best removed from the calculations of the DKP. The spectral analysis for each buoy velocity component was conducted using the following procedure:

1) the method of splines was used to create a data set of speeds at 2 hr intervals from the raw data set of speeds. Plots of the data set at 2 hr intervals were compared with plots of

the raw data sets for quality assurances.

2) the 2 hr data sets were analyzed using power spectral techniques. In addition, corresponding u and v data sets were analyzed using rotary spectral techniques.

5.2. Discussion of Spectra

Figures 8-10 show the u and v spectra for the velocity records shown in Figures 5-7. The general characteristics of the spectra for all three drifters are quite similar. ID's 1598 and 1599 showed strong energy peaks at about 14 days, while ID 1600 showed a peak at 17 days. As 1600 was farther from the ring center than the other two drifters, this shows a non-rigid body rotation of the ring. It is also noteworthy that the strong mesoscale signal that is apparent in this figure is rarely seen in current meter records. The reason for this is that the Lagrangian measurements follow flow-specific features whereas current meter measurements require the features to pass over the mooring.

All three spectra indicate some structure at about one week. Comparisons with surface winds from NOAA weather buoys moored in the Gulf of Mexico suggest that this is mostly meteorological. Also, there appears to be some energy at about 32 hours. It is speculated that this may be associated with the tidal resonance predicted by Reid and Whitaker (1981). Diurnal tides are clearly seen in the u components but less clearly seen in the v. The semi-diurnal tidal components are barely above the background level. Finally, the u components show some structure around 7 hours. Reid and Whitaker found a free gravity mode at this period.

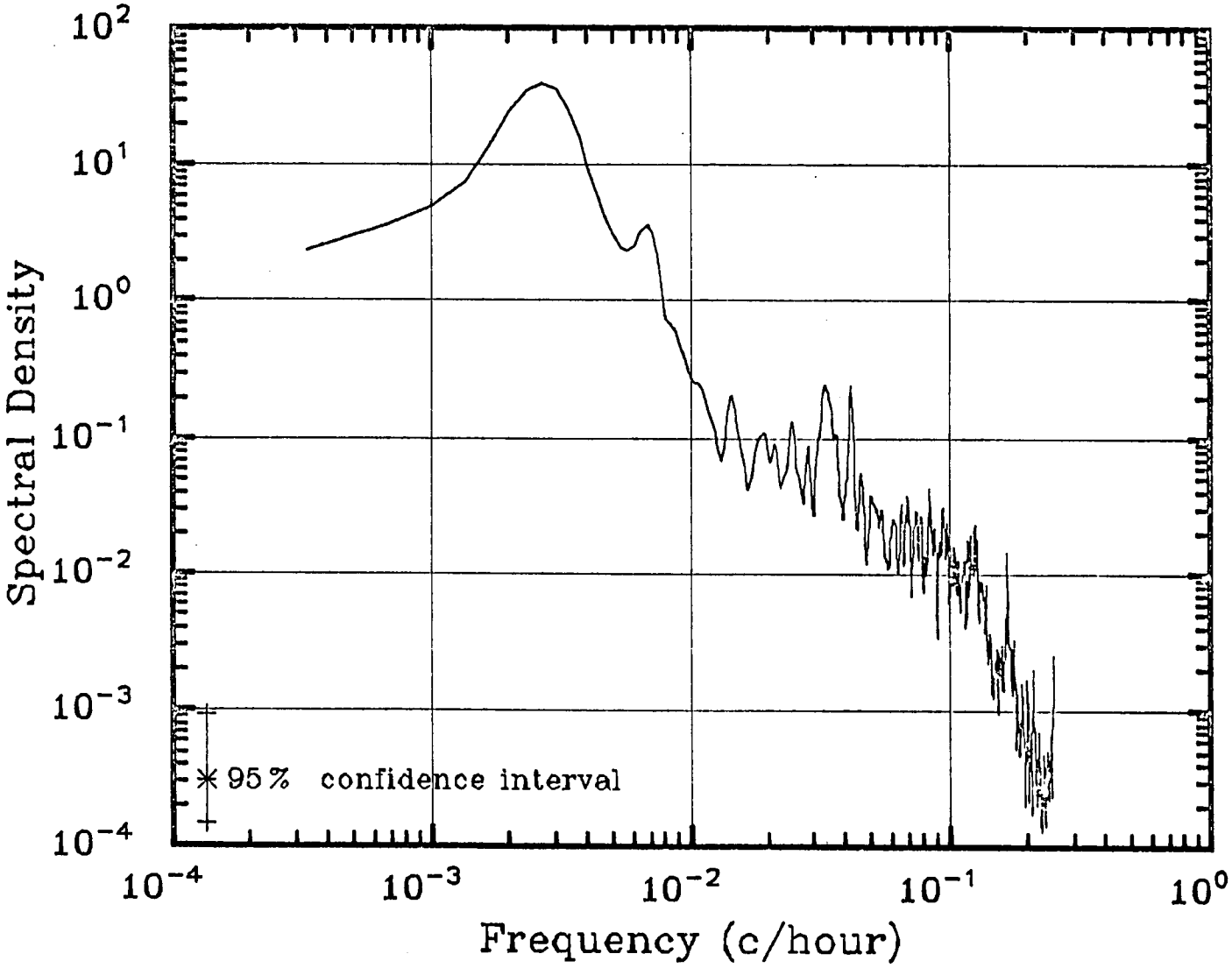

Fig. 8a. Power spectrum for the absolute u velocity component of buoy 1598.

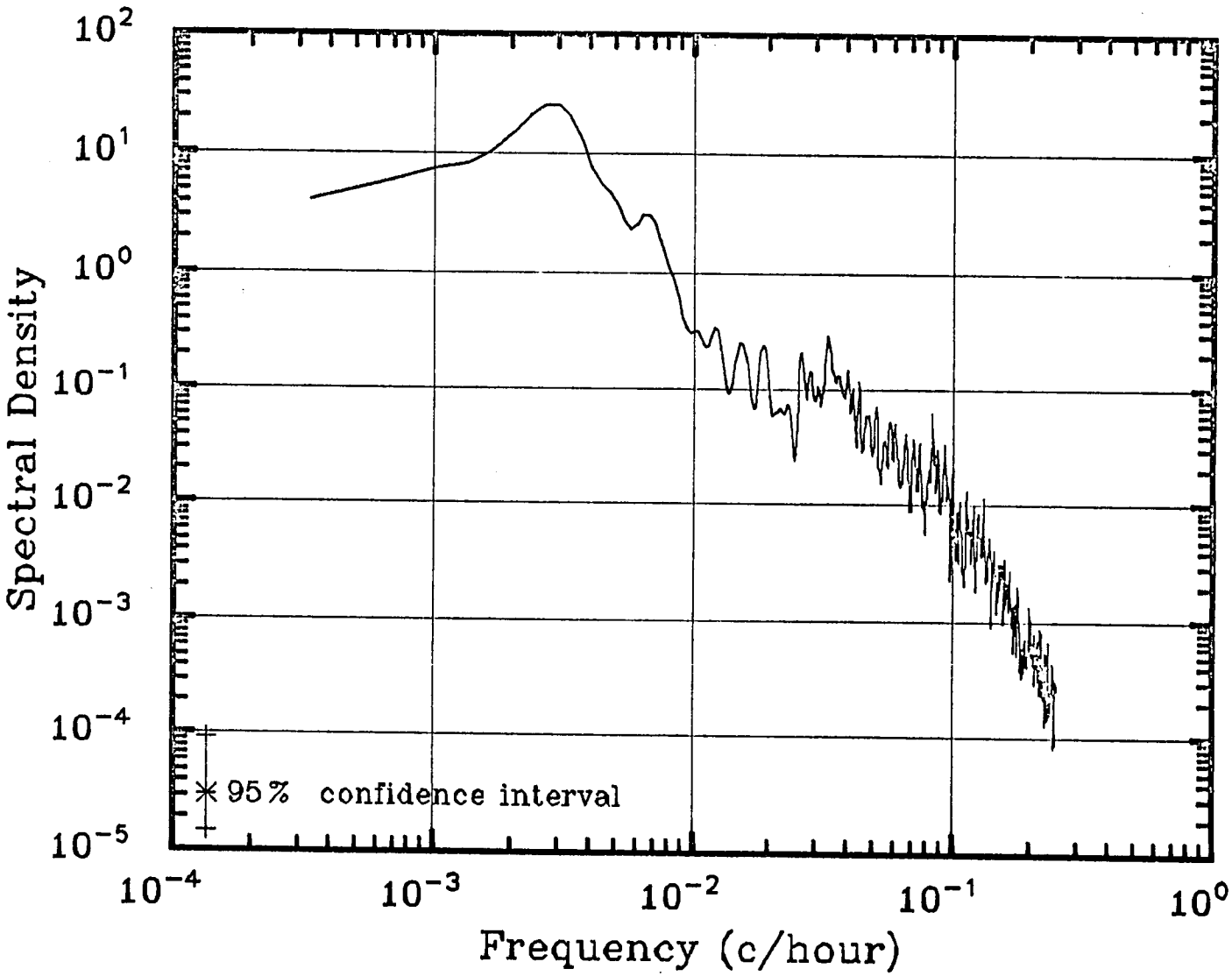

Fig. 8b. Power spectrum for the absolute v velocity component of buoy 1598.

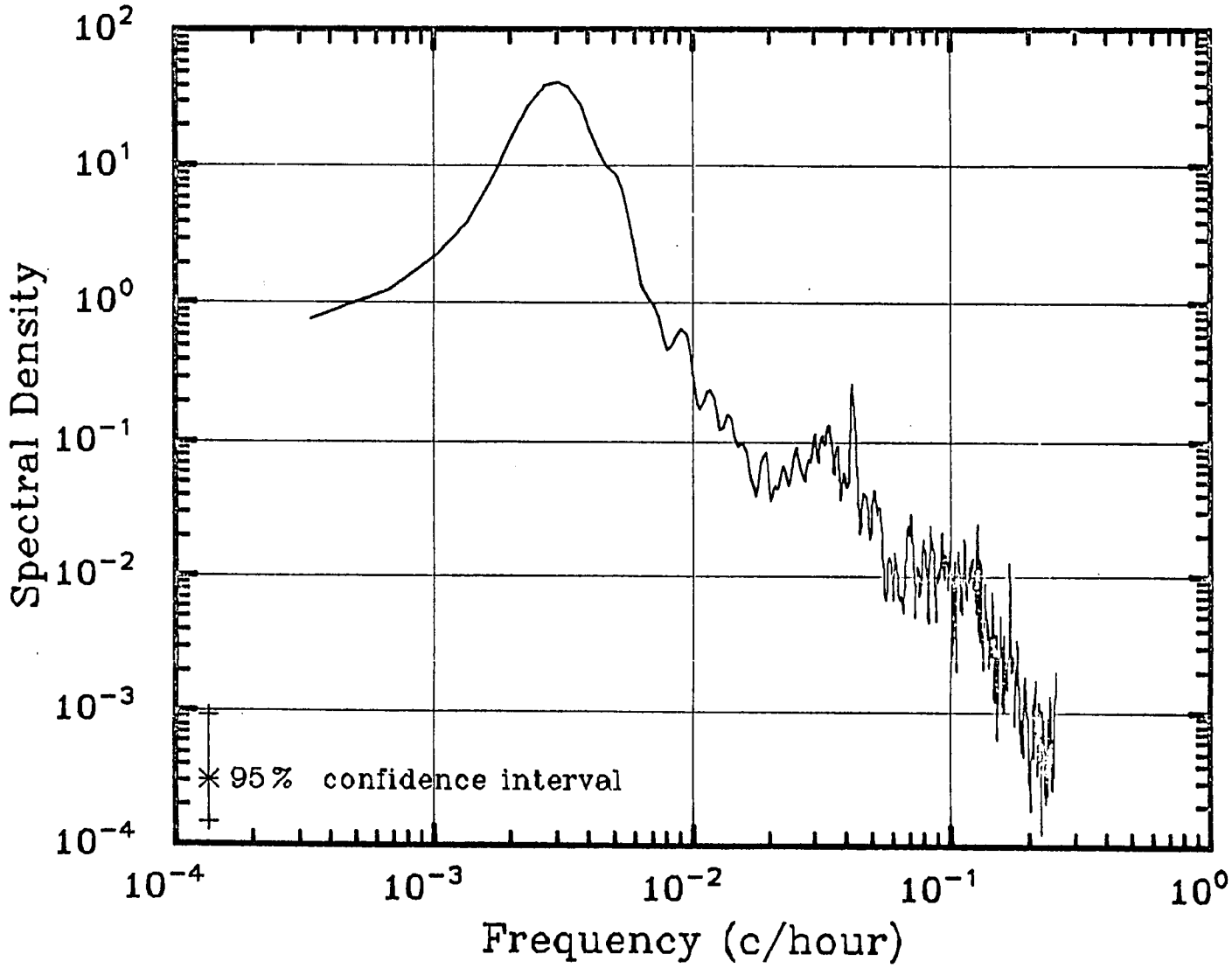

Fig. 9a. Power spectrum for the absolute u velocity component of buoy 1599.

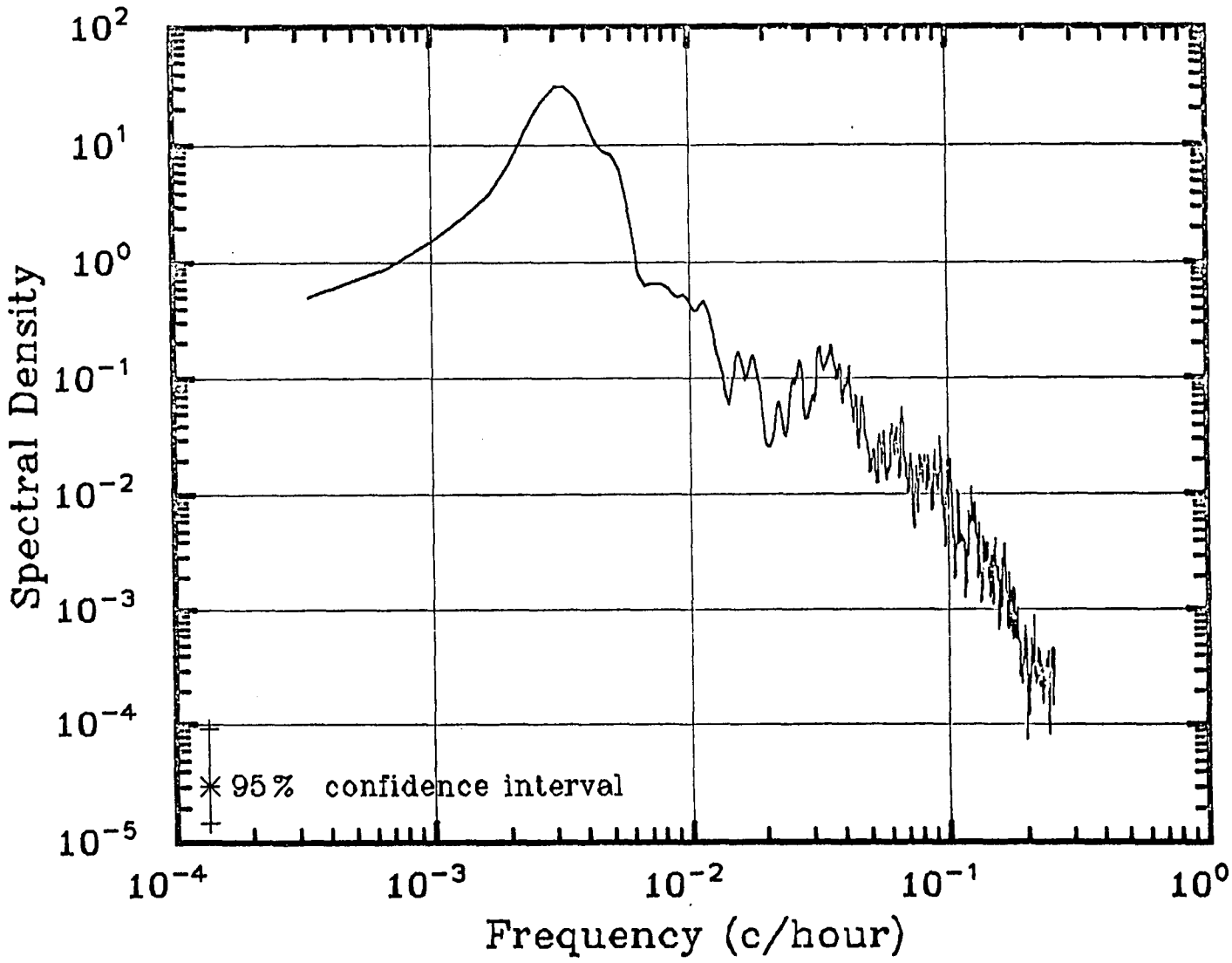

Fig. 9b. Power spectrum for the absolute v velocity component of buoy 1599.

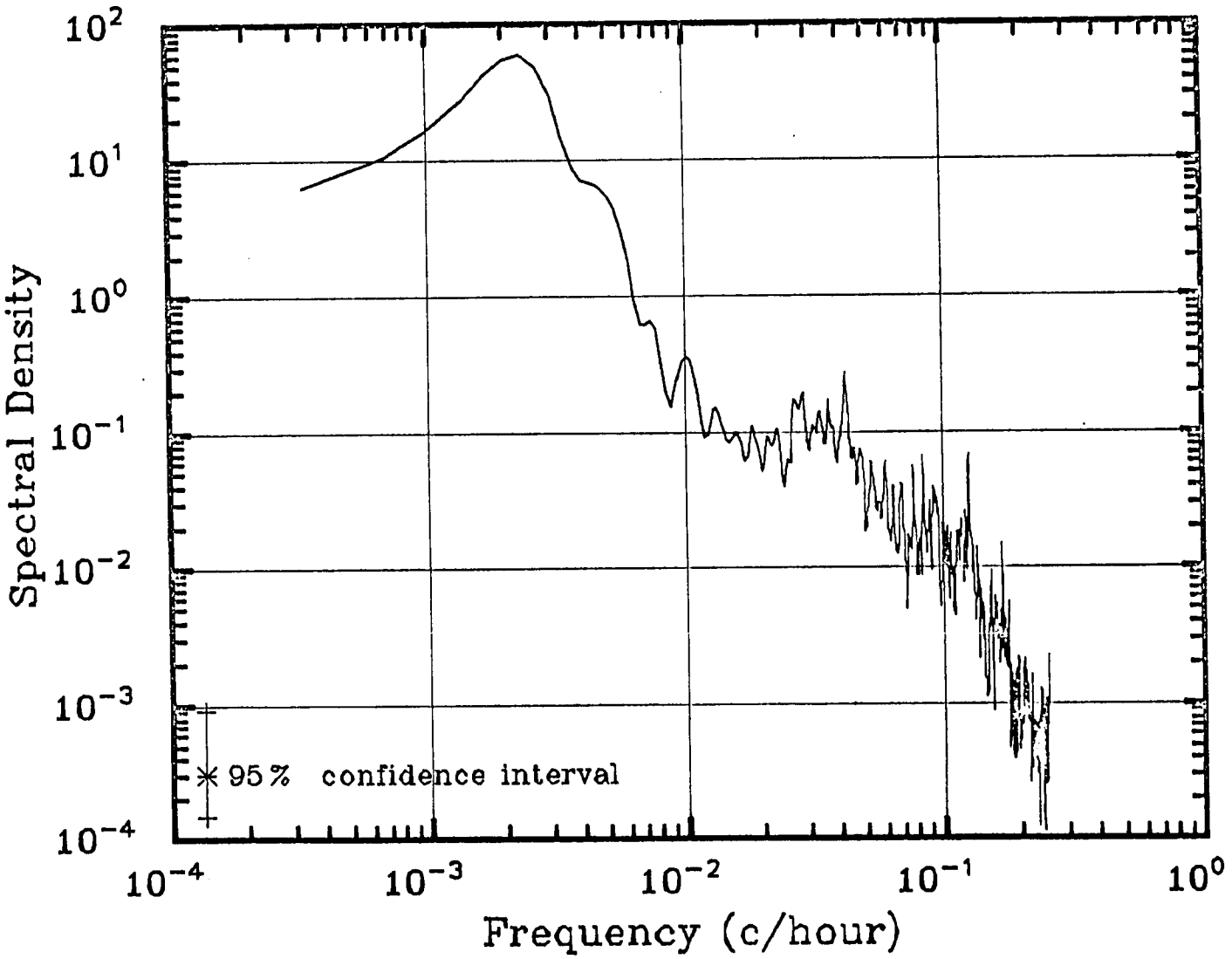

Fig. 10a. Power spectrum for the absolute u velocity component of buoy 1600.

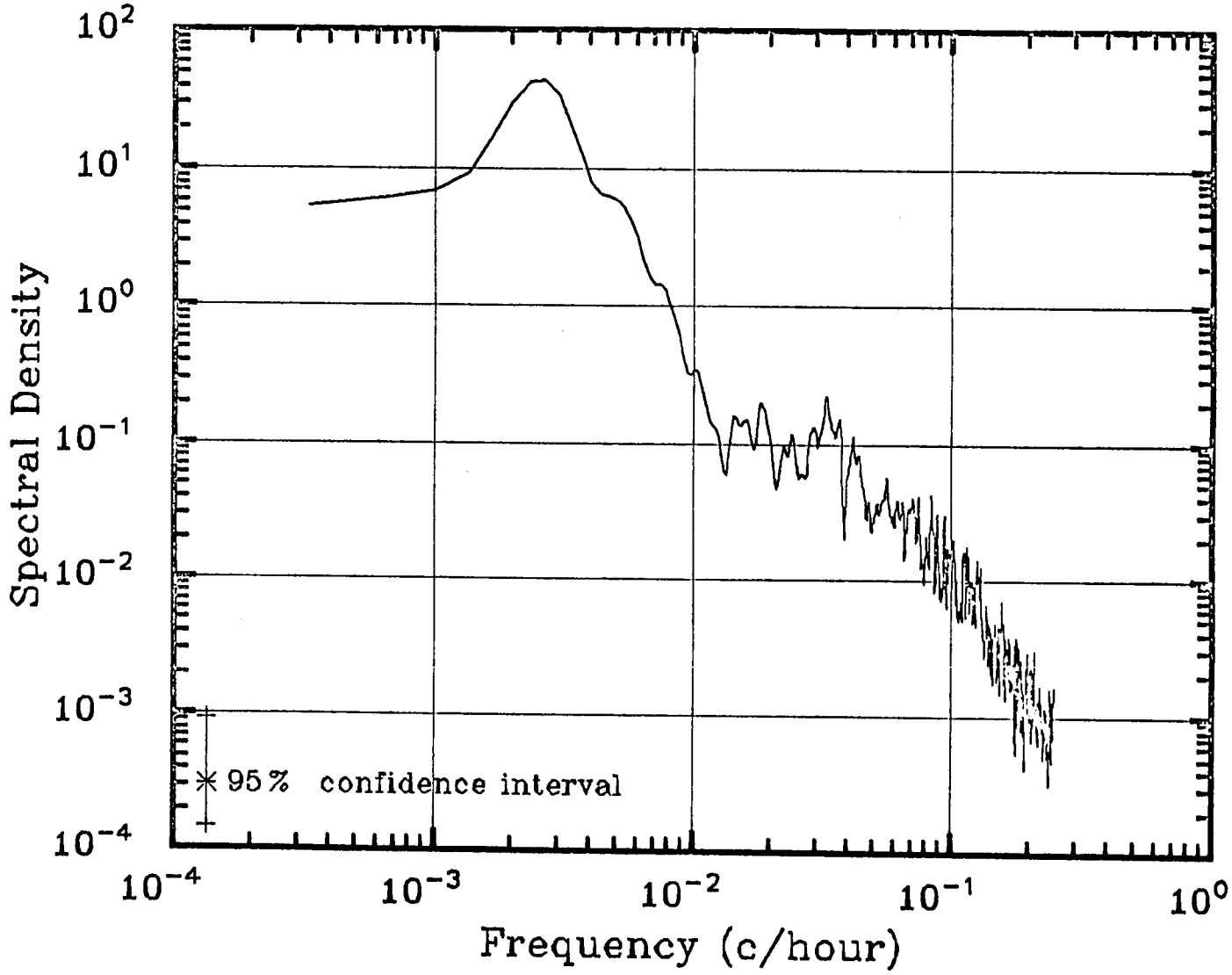

Fig. 10b. Power spectrum for the absolute v velocity component of buoy 1600.

Figures 11-13 show the rotary spectra for the three drifters. From this it is seen that the mesoscale peak is clearly anticyclonic which is, of course, consistent with the warm core character of the ring. The meteorological signal is anticyclonic in 1598 but this sense is not so clear in the other two spectra. The 33-hour resonance is clearly anticyclonic and the diurnal tide is cyclonic. It would appear from 1598 and 1600 that the semi-diurnal tide is anticyclonic. The tidal model studies of Mungall, et al (1978) show the drifters spent considerable time in a region with anticyclonic semi-diurnal motions and cyclonic diurnal flows. Also, the 7-hour signal in 1600 is anticyclonic but this is not substantiated with the other two drifters.

Figures 14-16 show the coherence between the speed components of the three drifters. It is seen that it is quite high down to about 0.9×10^{-2} cph, or roughly 5 days. Significant peaks in the coherence also occur at 33 hours and at the diurnal tide. The phase (not shown) is quite stable up to 0.9×10^{-2} cph, varying between -90° to -120° (i.e., u leads v).

5.3 Design of Filters for Removing High Frequency Fluctuations

From the discussion above, it seems that meteorologically induced slippage/Ekman current may be associated with the one week fluctuation. The tidal signals given by the drifters are in general agreement with the model studies of Mungal, et al. The 7 hour signal could be produced by satellite position error or it could be the free mode found by Reid and Whitaker (1981). It is interesting to note that the energy at the inertial frequencies

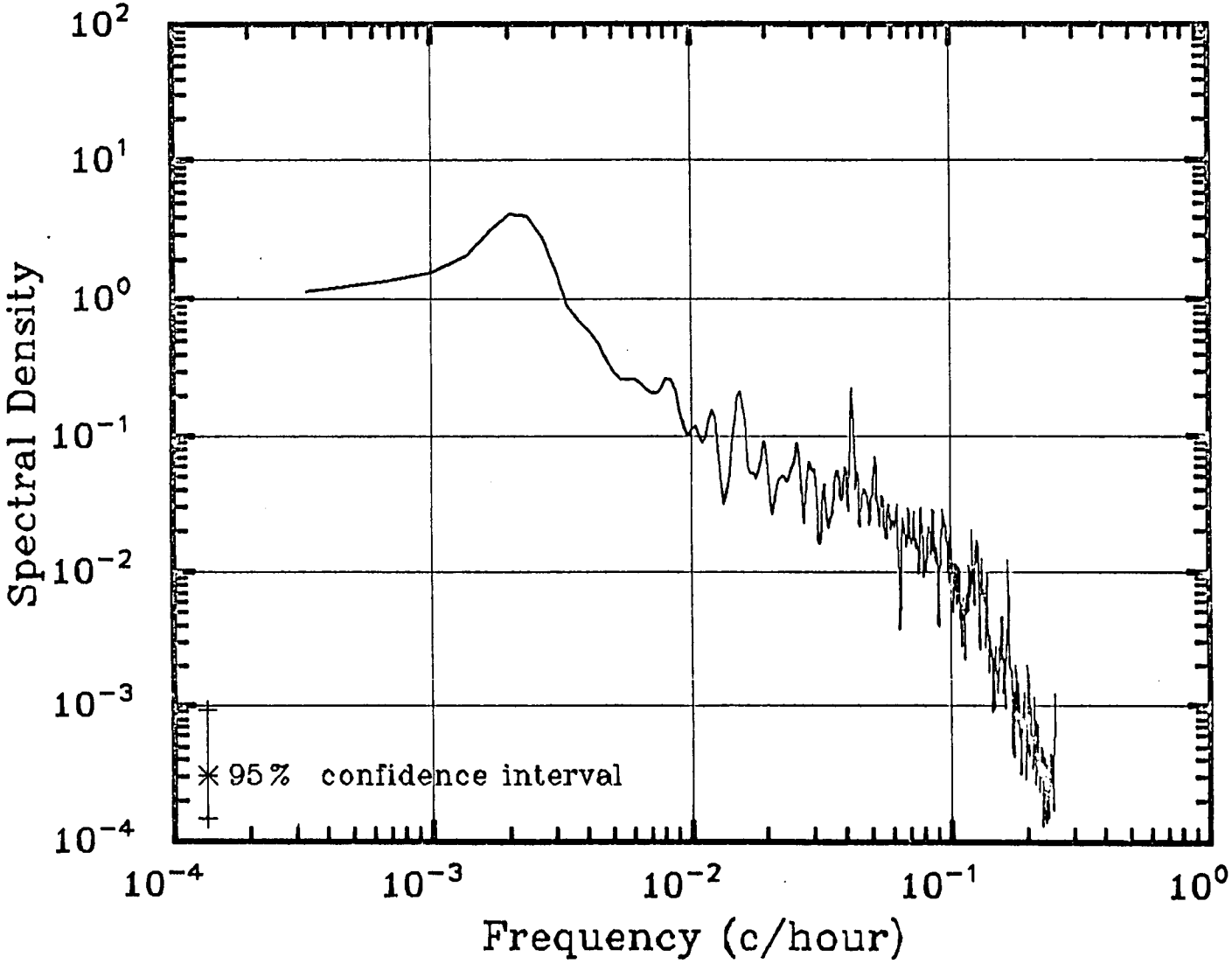

Fig. 11a. Power spectrum for the cyclonic rotary component of buoy 1598.

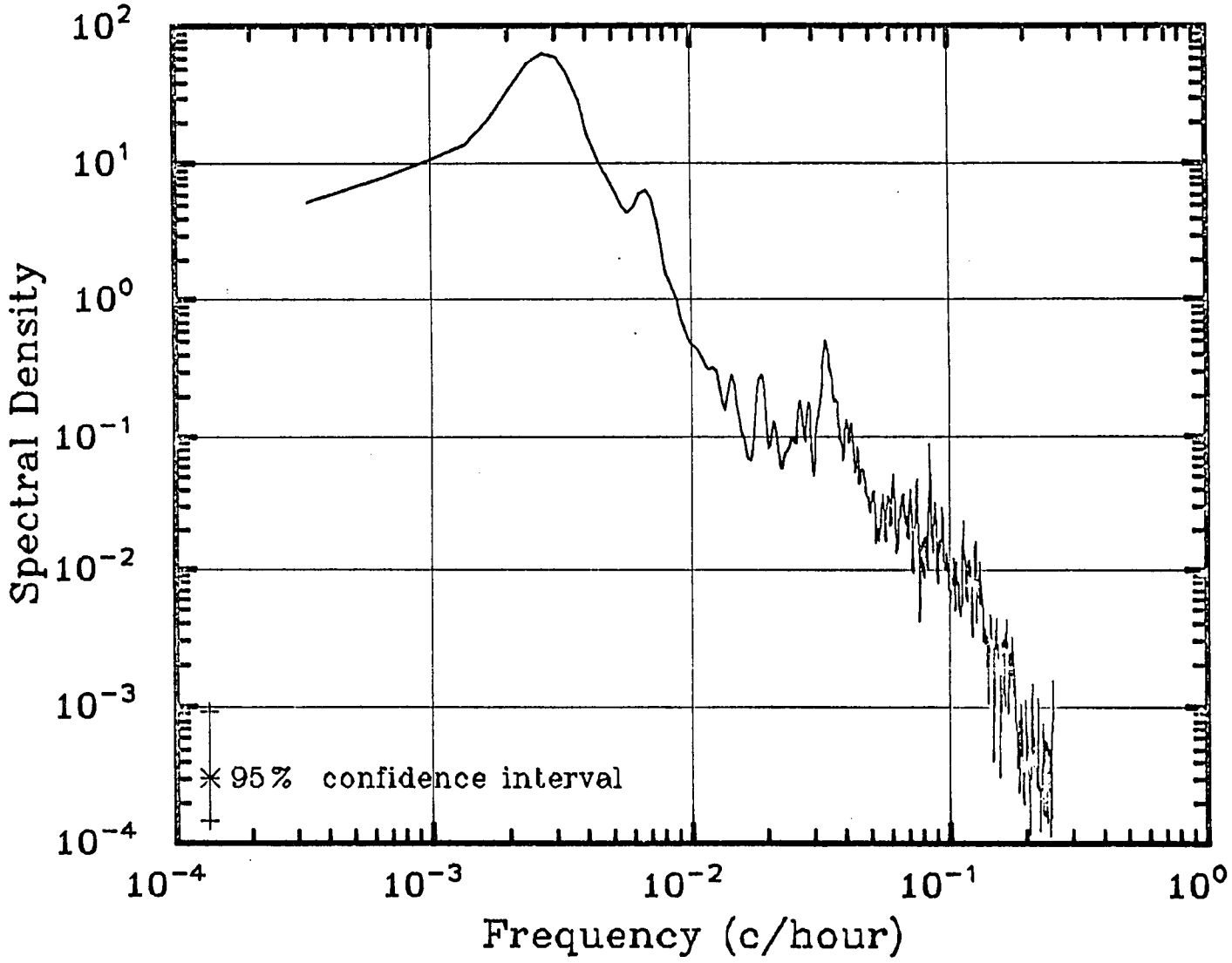

Fig. 11b. Power spectrum for the anticyclonic rotary component of buoy 1598.

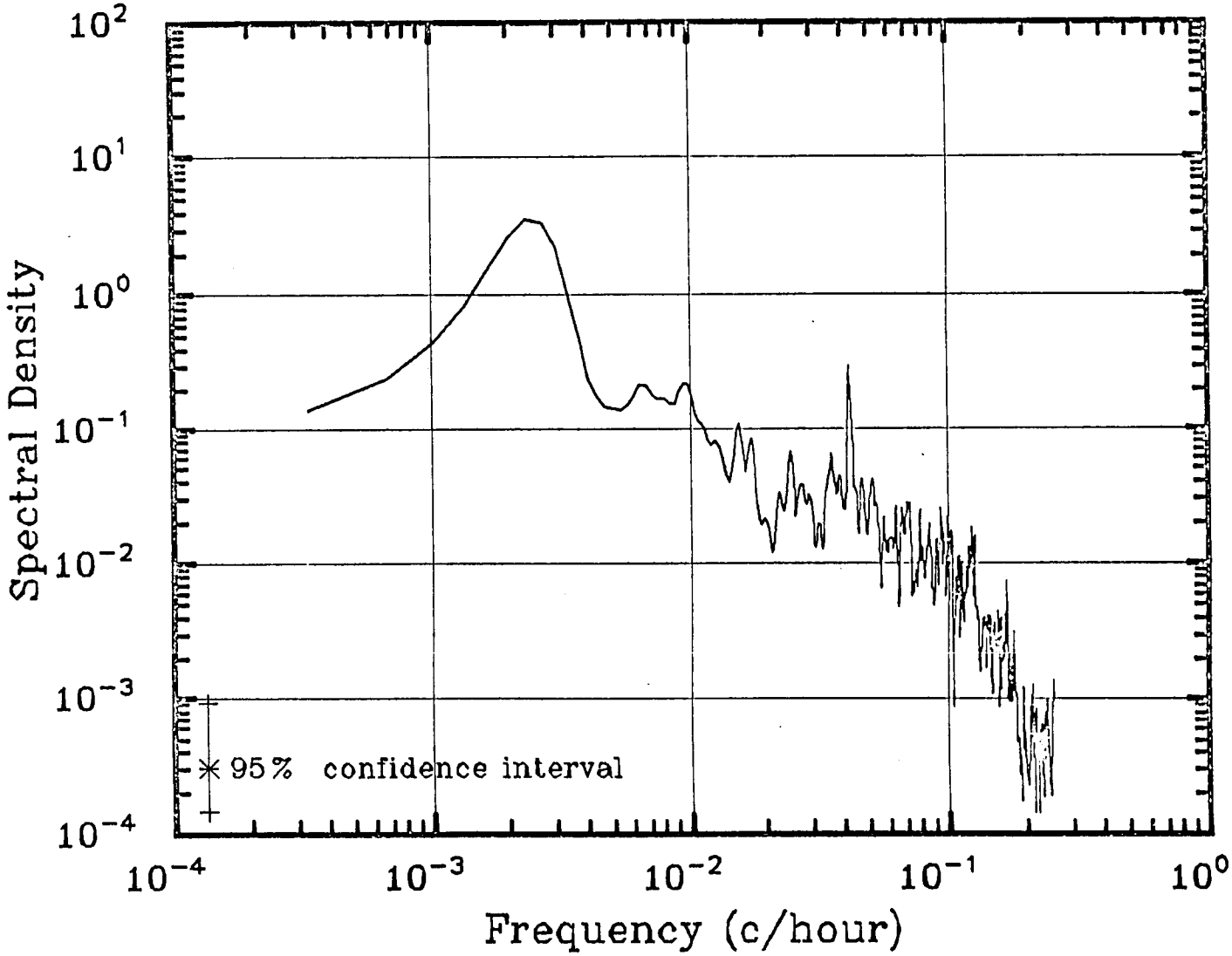

Fig. 12 a. Power spectrum for the cyclonic rotary component of buoy 1599.

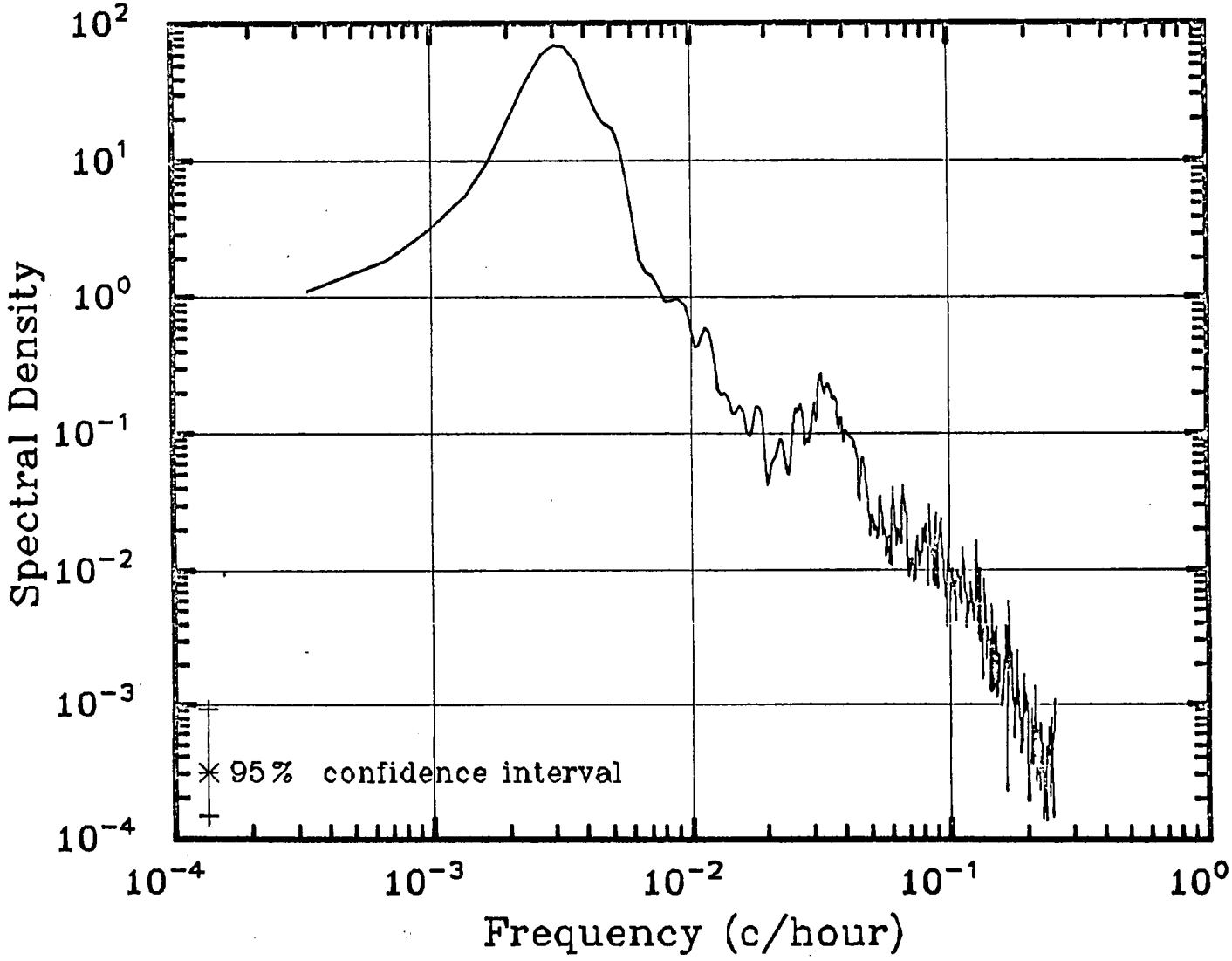

Fig. 12b. Power spectrum for the anticyclonic rotary component of buoy 1599.

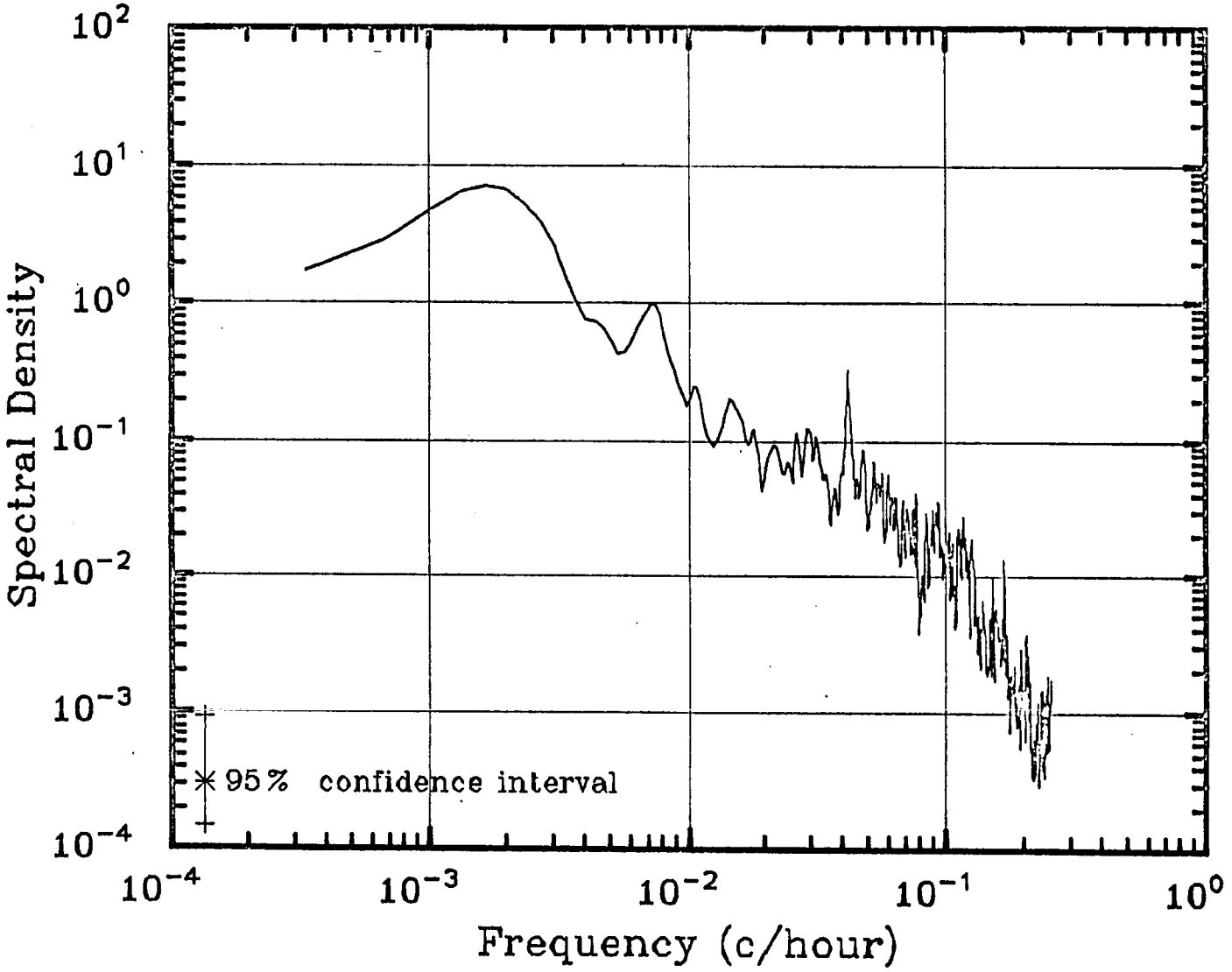

Fig. 13a. Power spectrum for the cyclonic rotary component of buoy 1600.

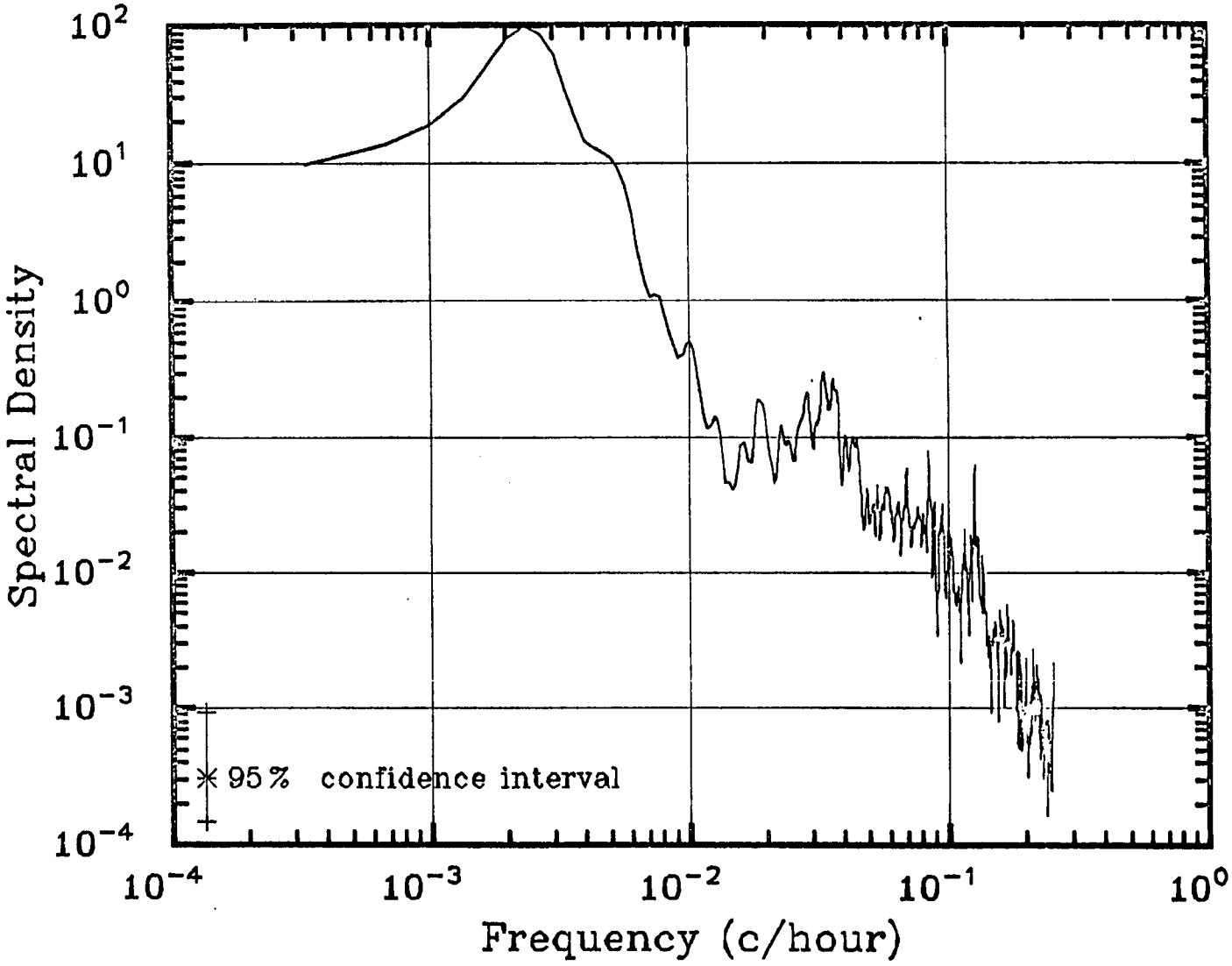

Fig. 13b. Power spectrum for the anticyclonic rotary component of buoy 1600.

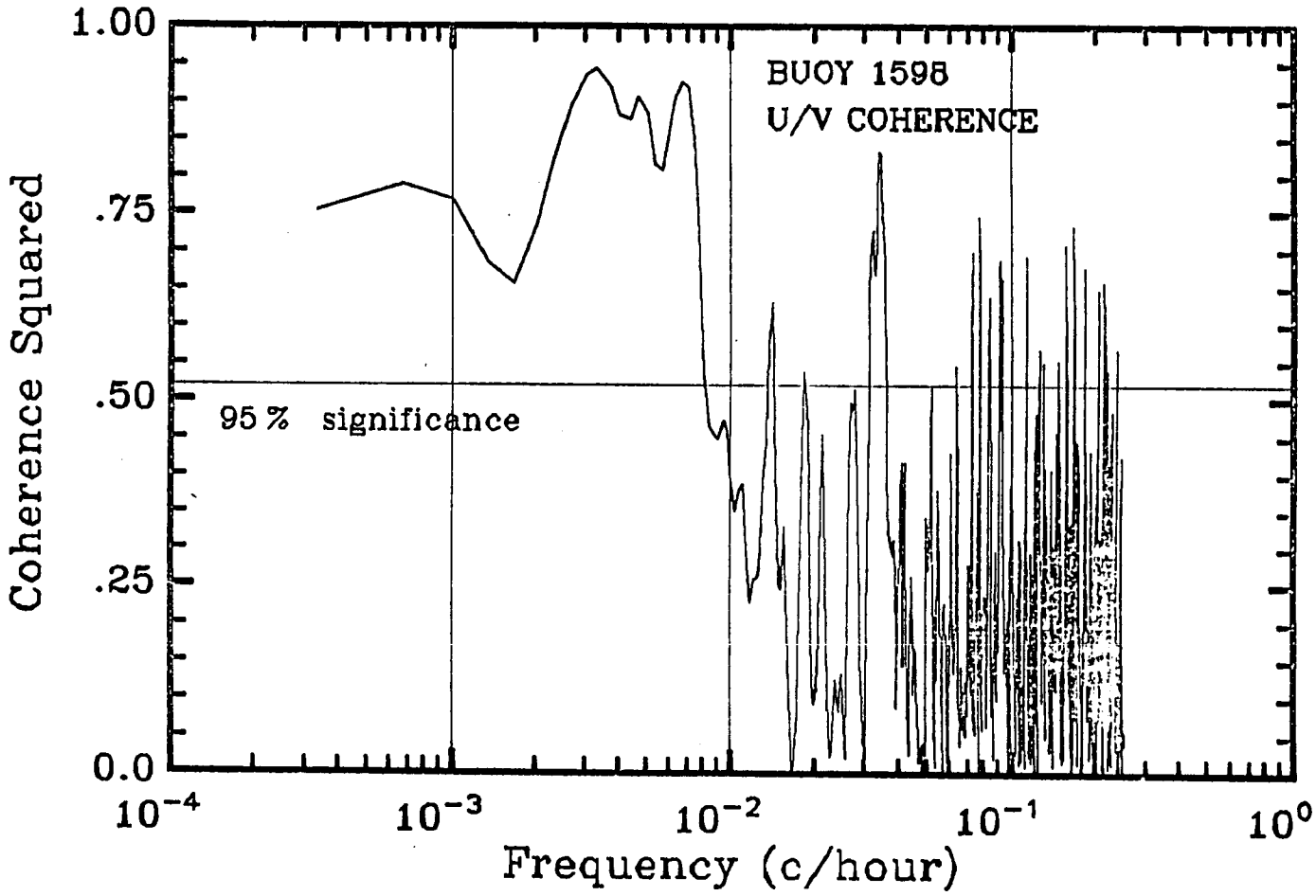

Fig. 14. Coherence spectrum for the u and v components of buoy 1598.

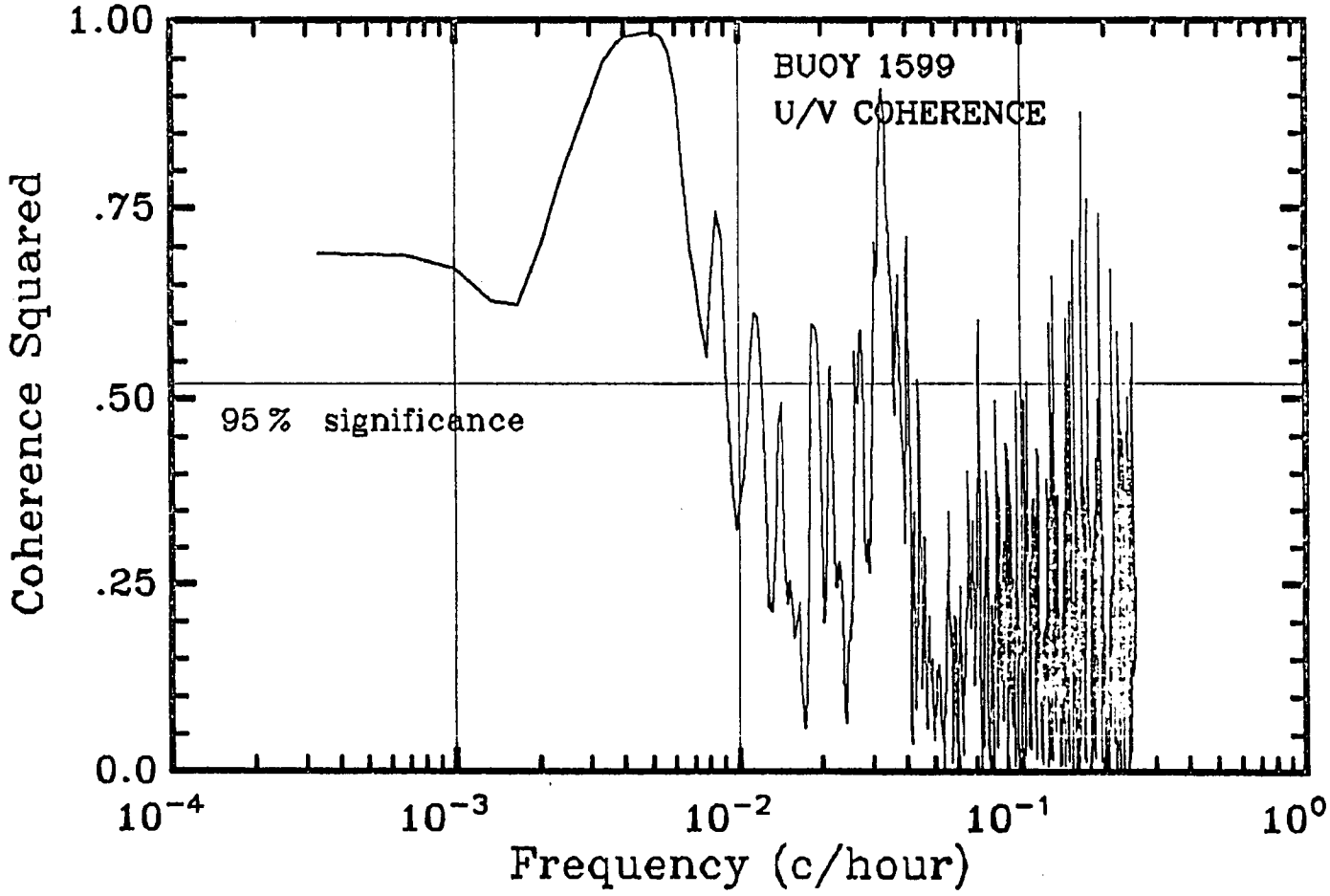

Fig. 15. Coherence spectrum for the u and v components of buoy 1599.

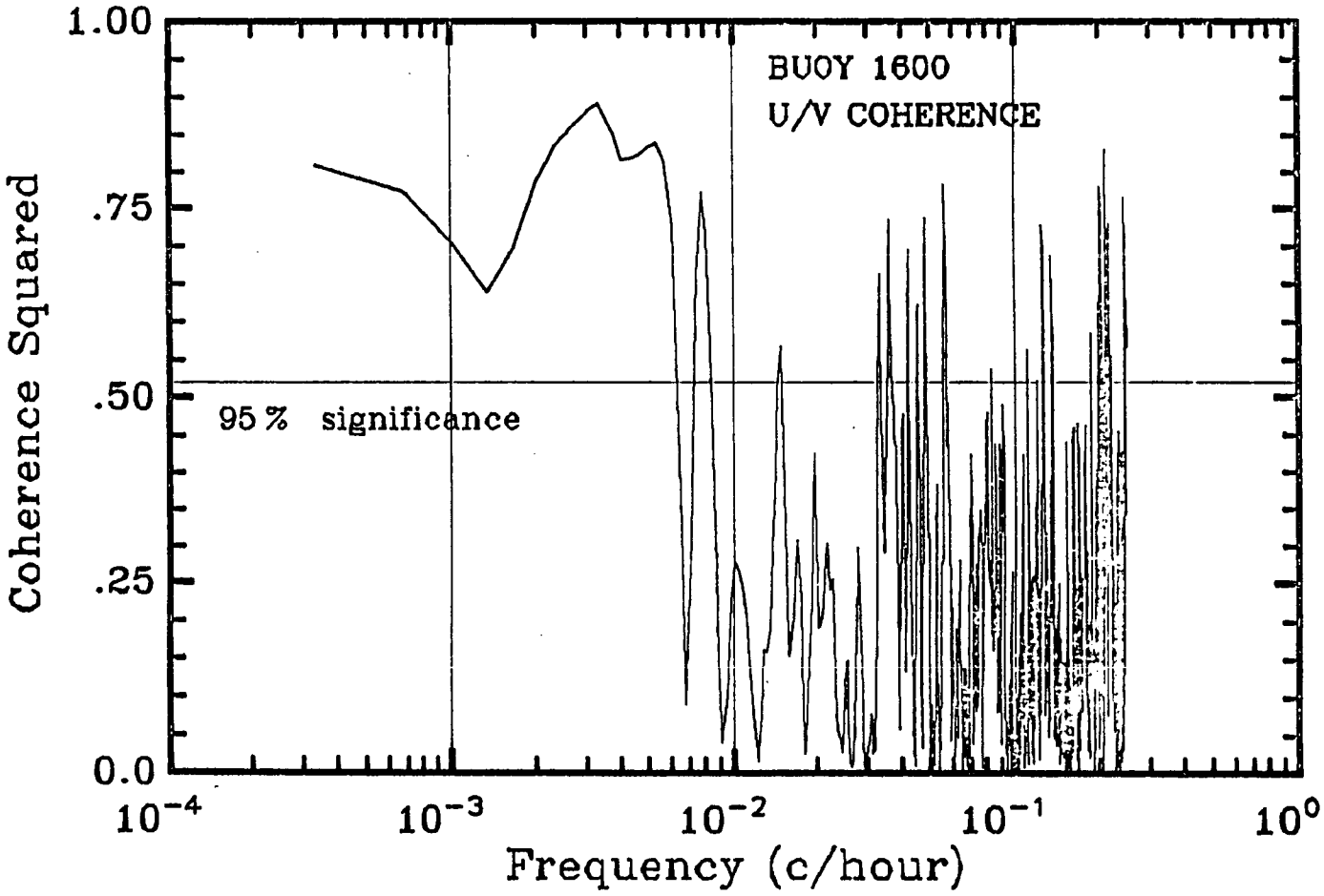

Fig. 16. Coherence spectrum for the u and v components of buoy 1600.

were broad-banded as opposed to the sharp spikes that are typically found. Also, no effect of shingles was detected.

This analysis suggests that standard filtering is sufficient to remove the fluctuations induced by the meteorology and tides. Thus, a 100 hr (½ power point), lowpass filter was generated to filter the velocity data. The filter was symmetric and used a Lanczos taper on the ends of the velocity data sets.

The filtered velocity records are shown in Figures 17-19. Comparison with the absolute velocity records (Figures 5-7) shows that the high frequency fluctuations have been removed and that no phase distortion was induced by the filtering operation.

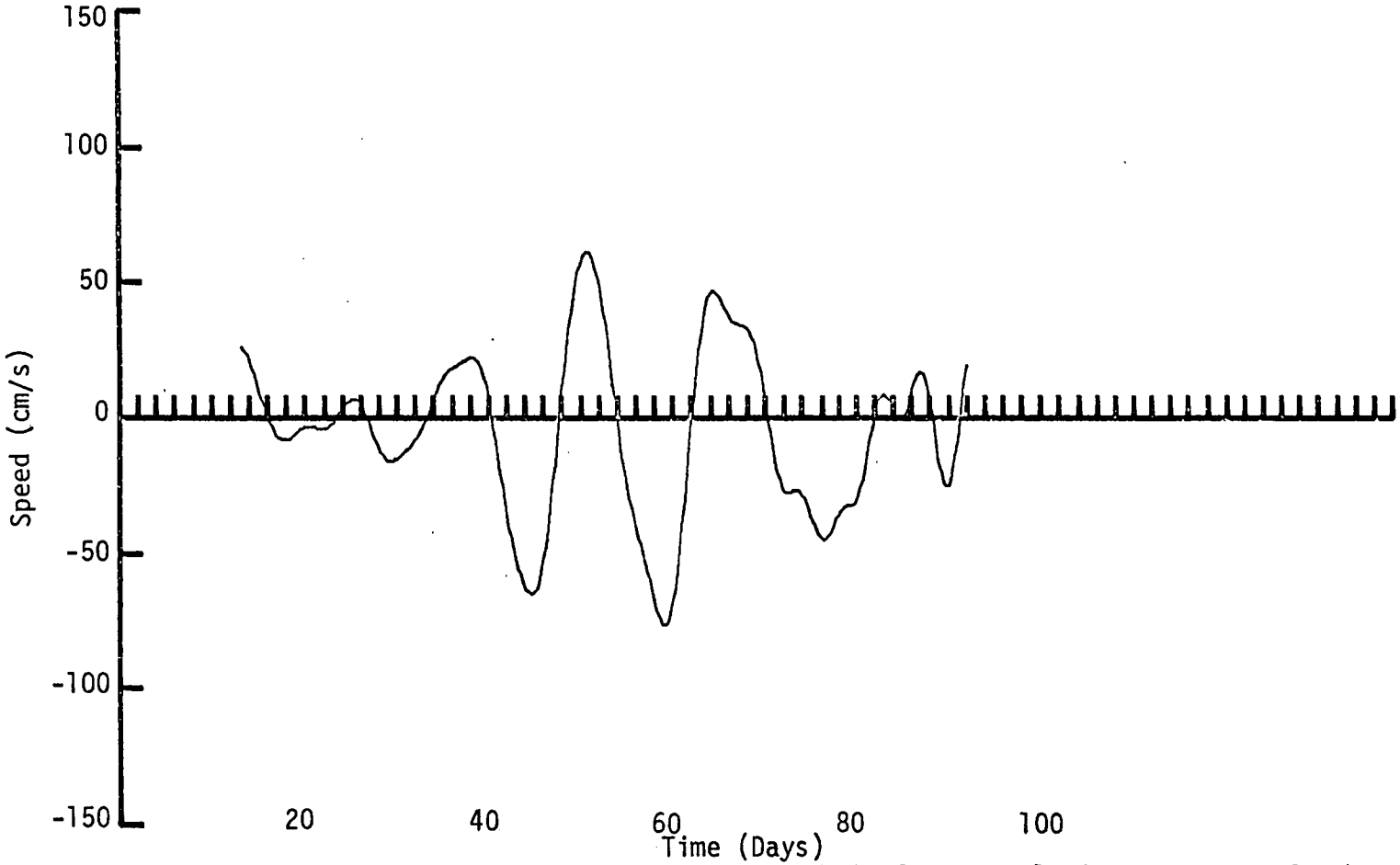

Fig. 17a. The time history of the filtered absolute u velocity component for buoy 1598.

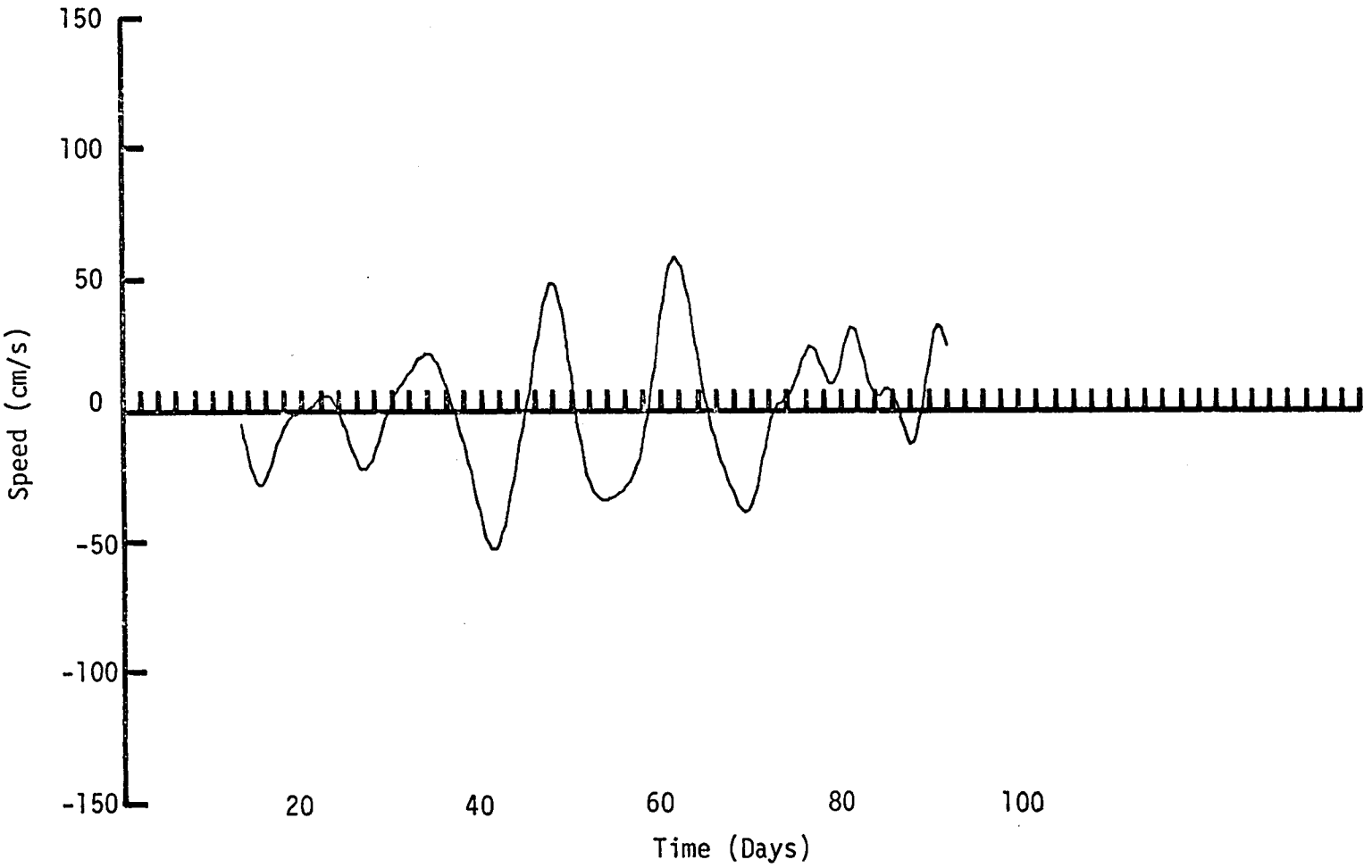

Fig. 17b. The time history of the filtered absolute v velocity component for buoy 1598.

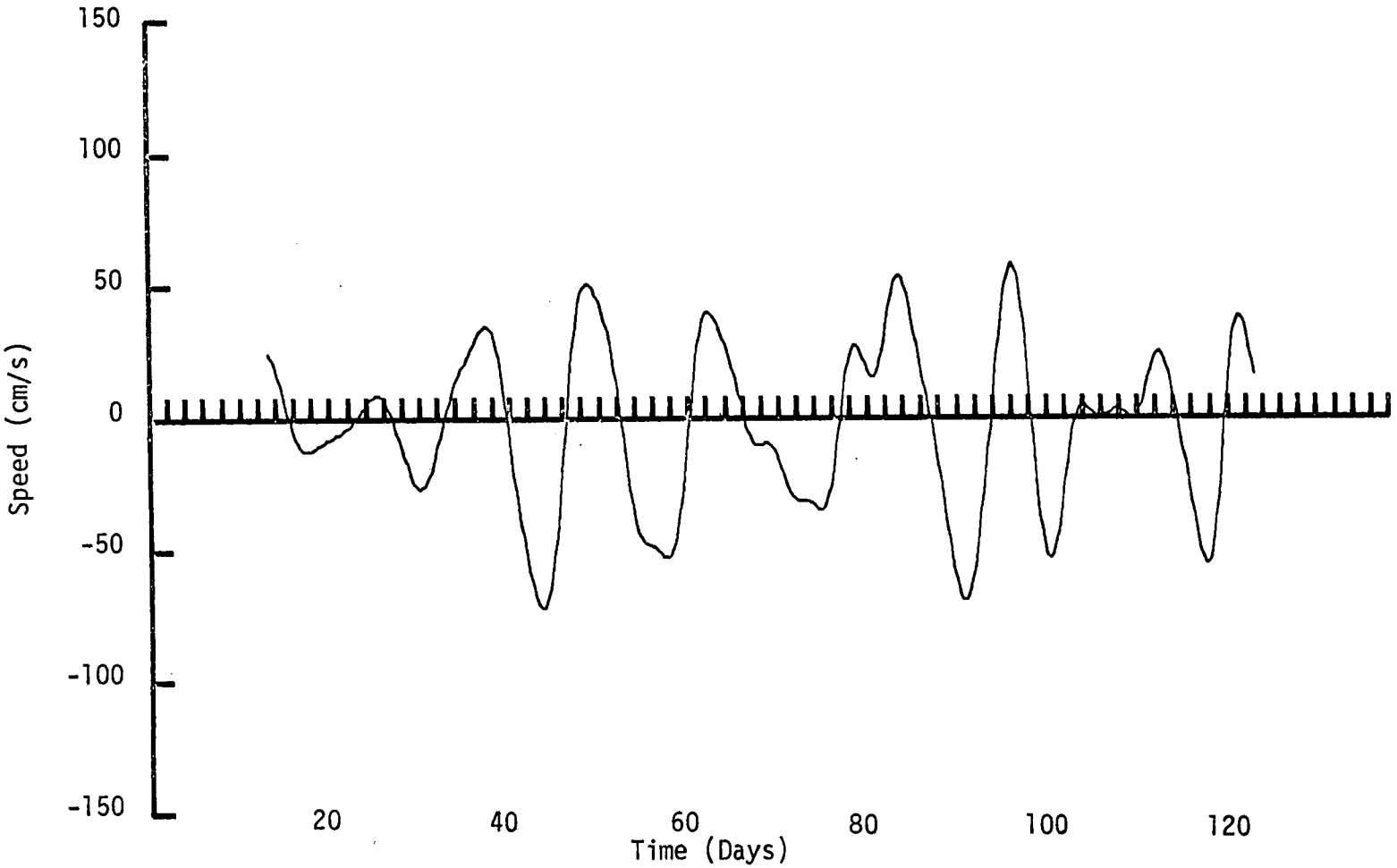

Fig. 18a. The time history of the filtered absolute u velocity component for buoy 1599.

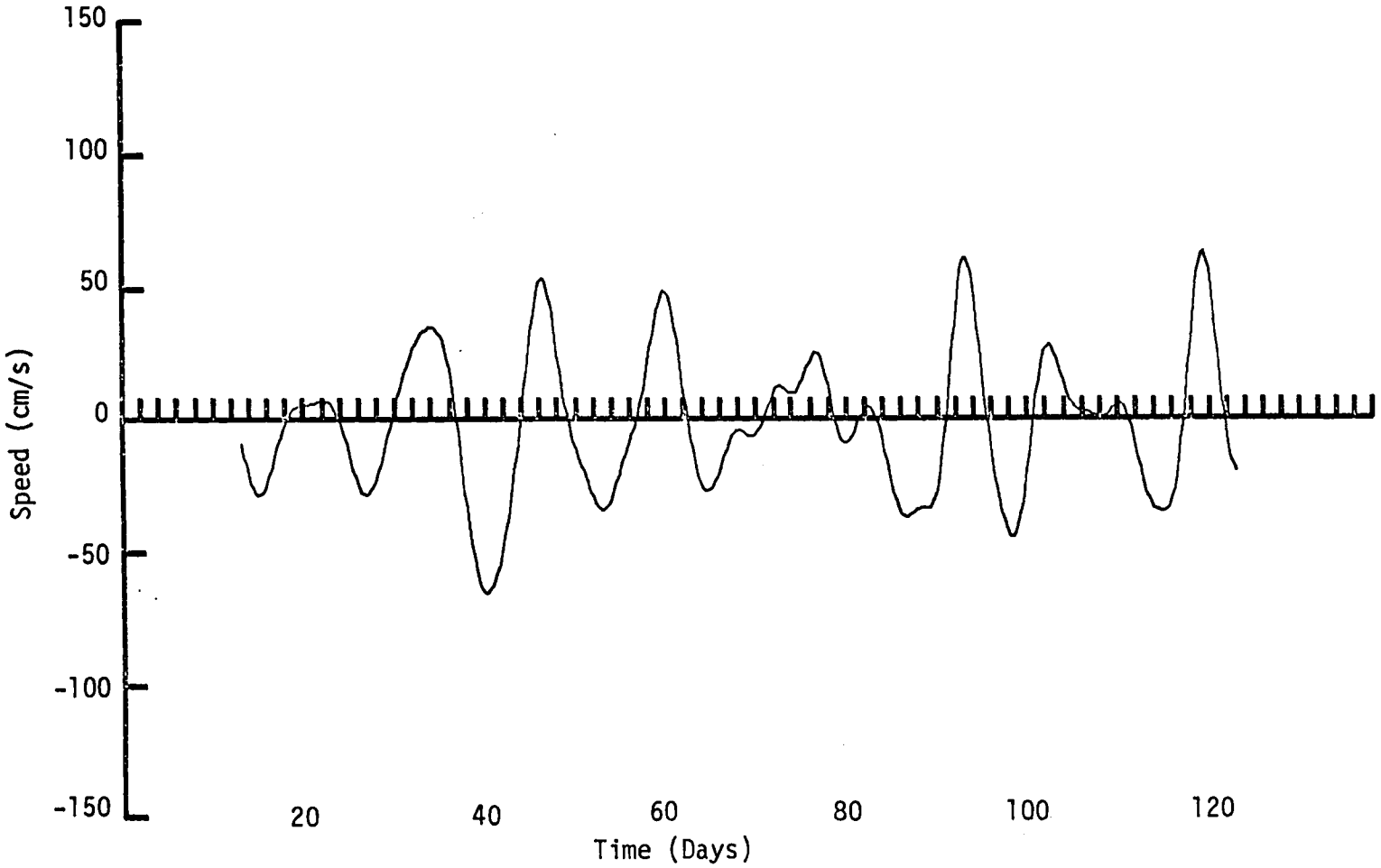

Fig. 18b. The time history of the filtered absolute v velocity component for buoy 1599.

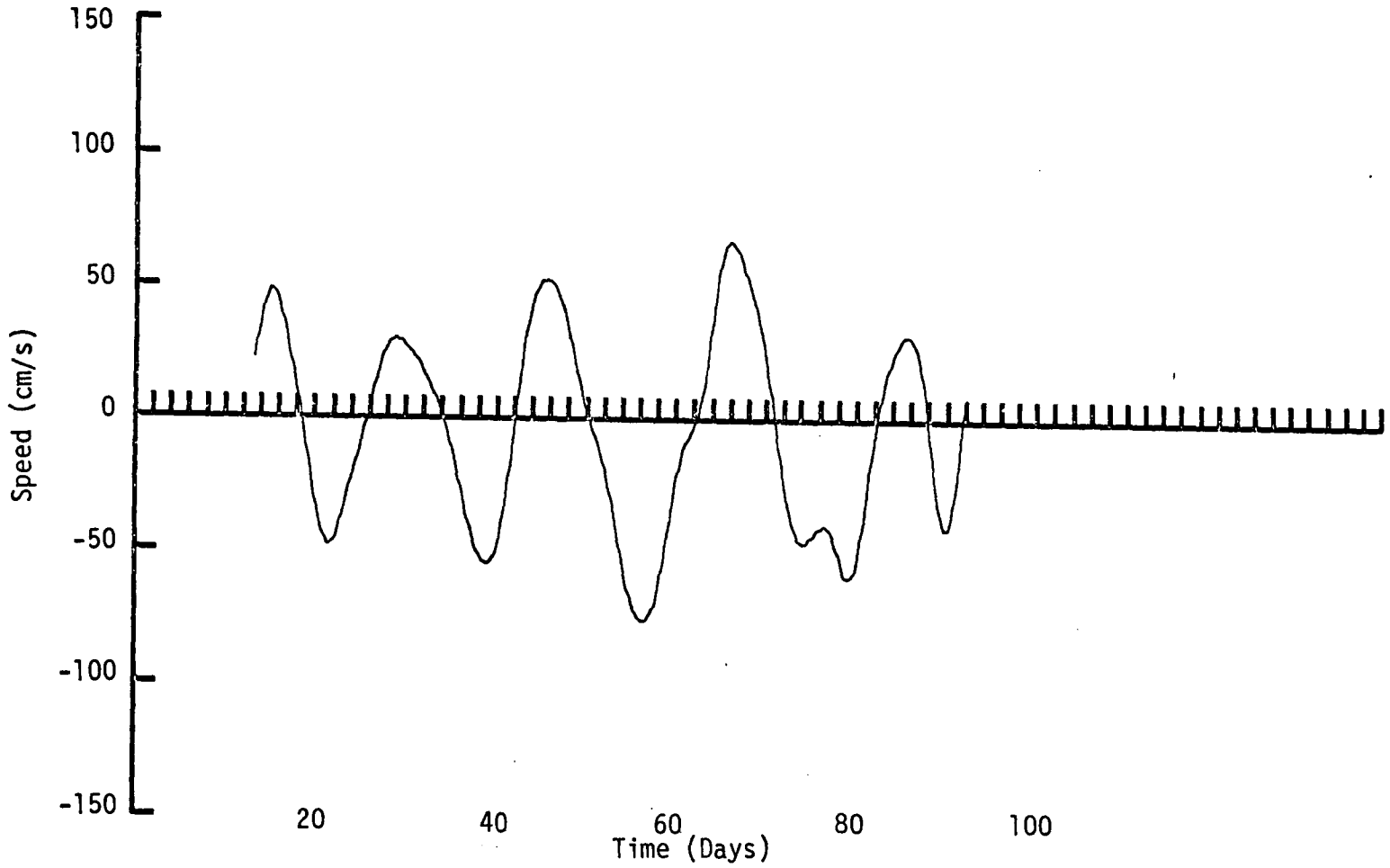

Fig. 19a. The time history of the filtered absolute u velocity component for buoy 1600.

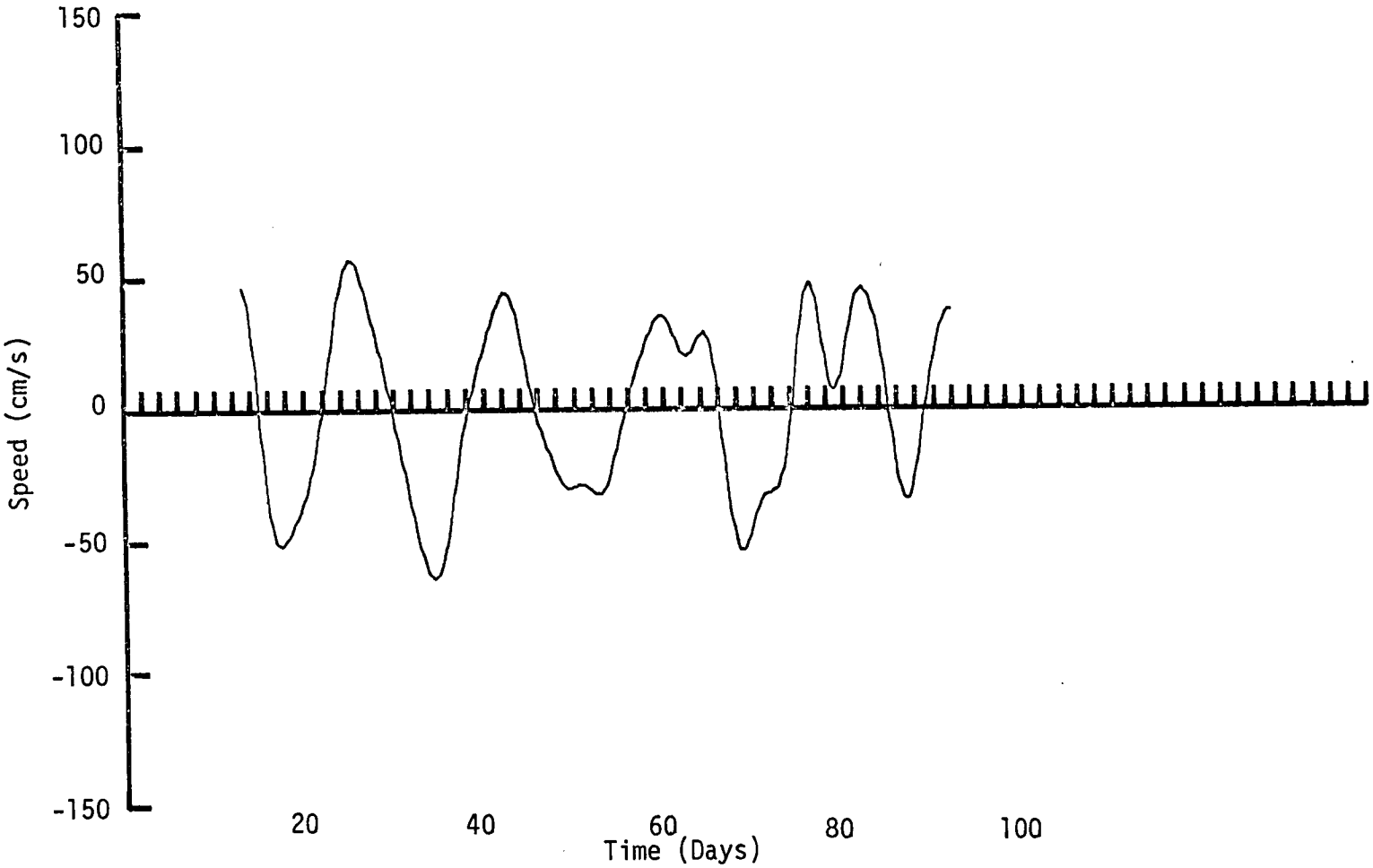

Fig. 19b. The time history of the filtered absolute v velocity component for buoy 1600.

6. Translation and Swirl Velocities

The translation velocities as inferred independently from the three drifters are shown in Figure 20. The calculations presented in this figure show remarkable consistency. All three drifters indicate a westward translation between 5 and 10 cm/s for almost the entire record. Only 1600 shows eastward movement during the period 8-23 February. This was noted previously. All three drifters also indicate an initial southward translation. All three also show a change to a northward translation about the middle of December. All three indicate a de-acceleration to the north, with 1599 and 1600 actually moving briefly to the south.

Considering the crudeness of the model and the uncertainties in regard to the slippage, the agreement on the translation velocities of all three drifters is considered to be quite good. With the exception of brief periods, the drifters all indicate the same velocities to within 5 cm/s. This is considerably more accurate than the velocity measurement itself.

The swirl velocities are shown in Figure 21. Component values are of the order of 40 cm/s with peak values approaching 75 cm/s. The east/west swirl component for 1600 is generally higher than that for the other two drifters. However, the east/west swirl component for 1598 and 1599 show great similarity with differences at most of the order of 20 cm/s.

The average values of the north swirl component of the three drifters is about the same as that of the east swirl component. However, the extremes of the north swirl component are considerably less than those of the east swirl component.

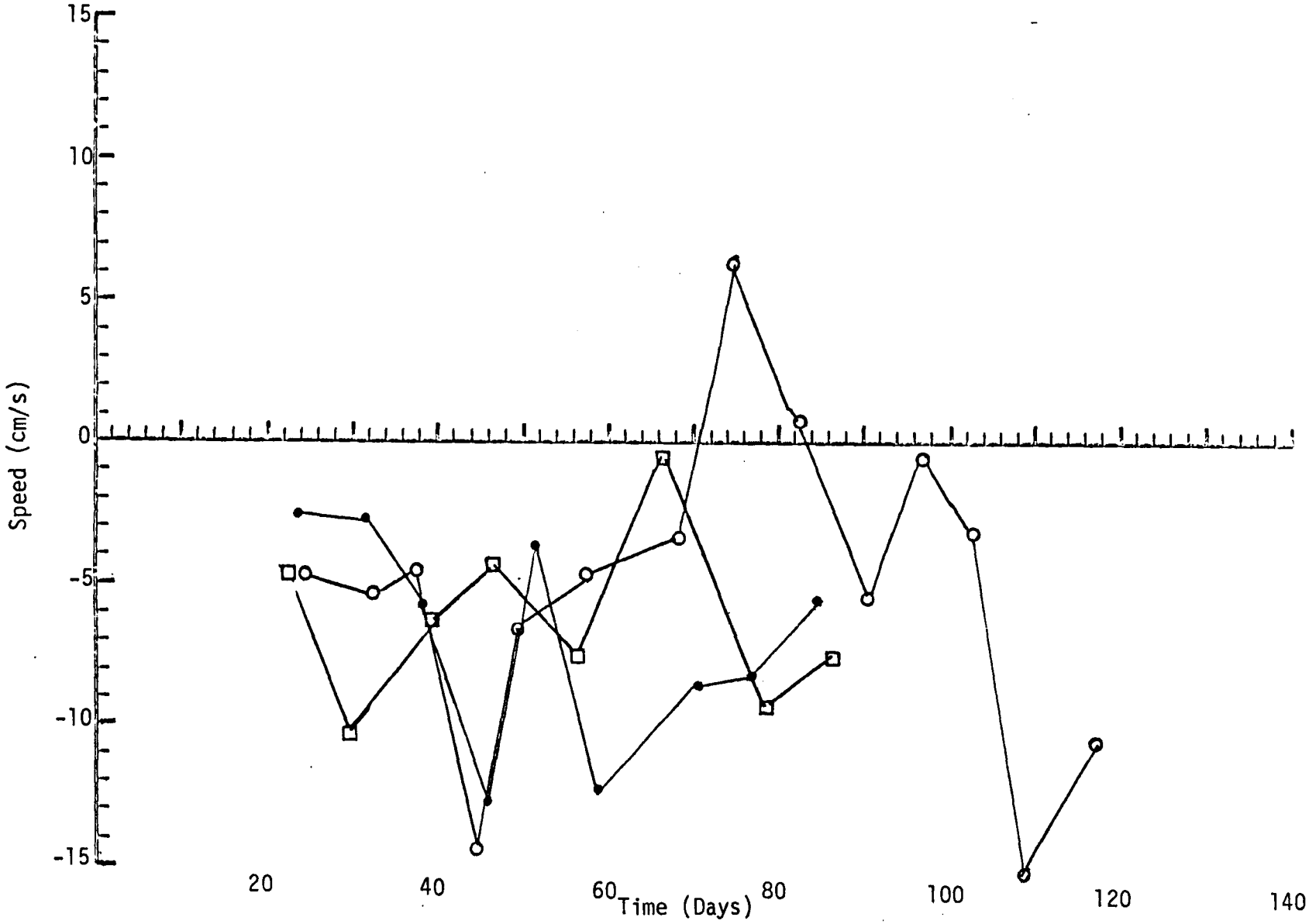

Fig. 20a. Time histories of the east/west component of the ring translation. For ID's 1598 (dot), 1599 (circle) and 1600 (box).

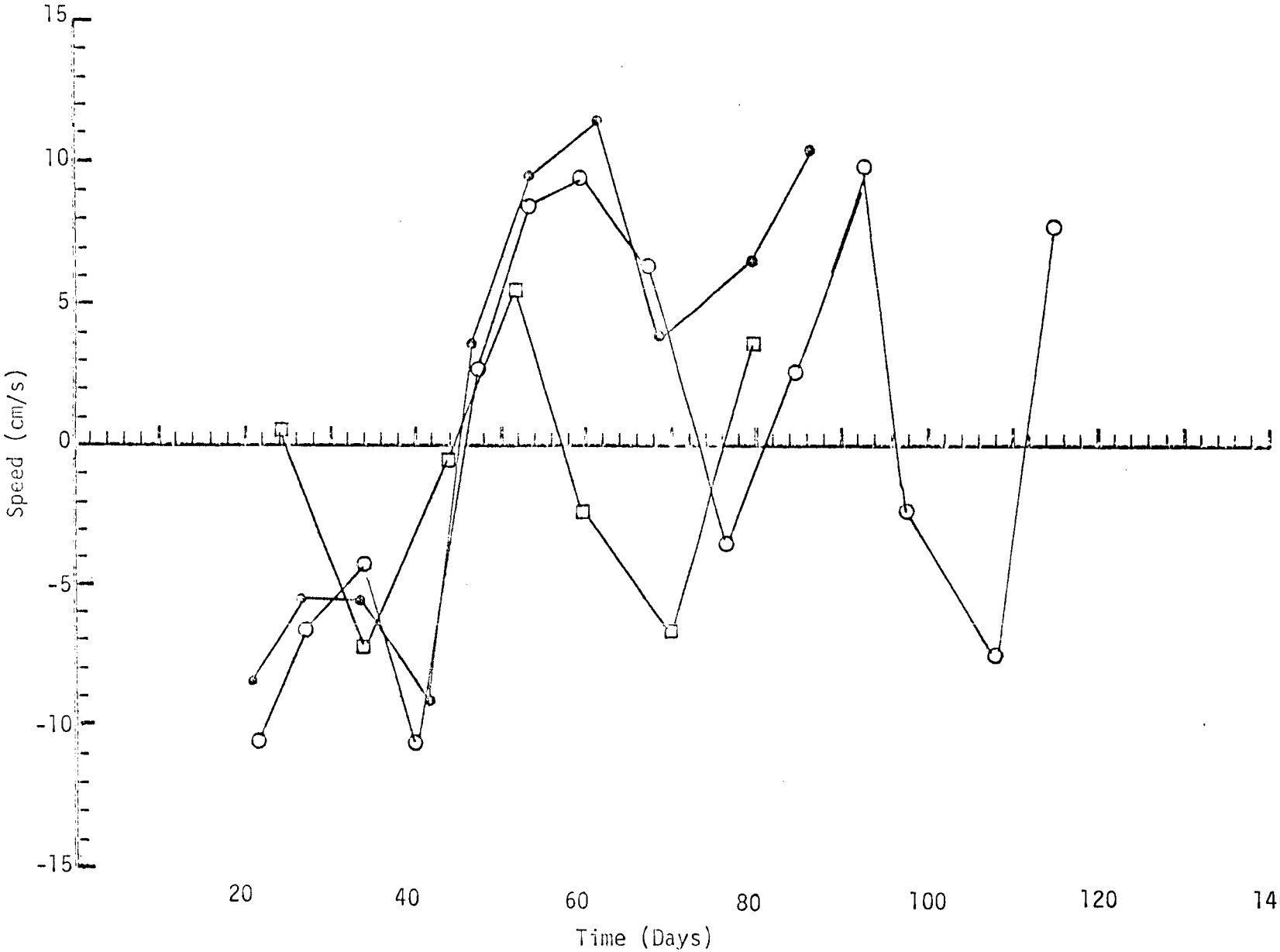

Fig. 20b. Time histories of the north/south component of the ring translation. For ID's 1598 (dot), 1599 (circle) and 1600 (box).

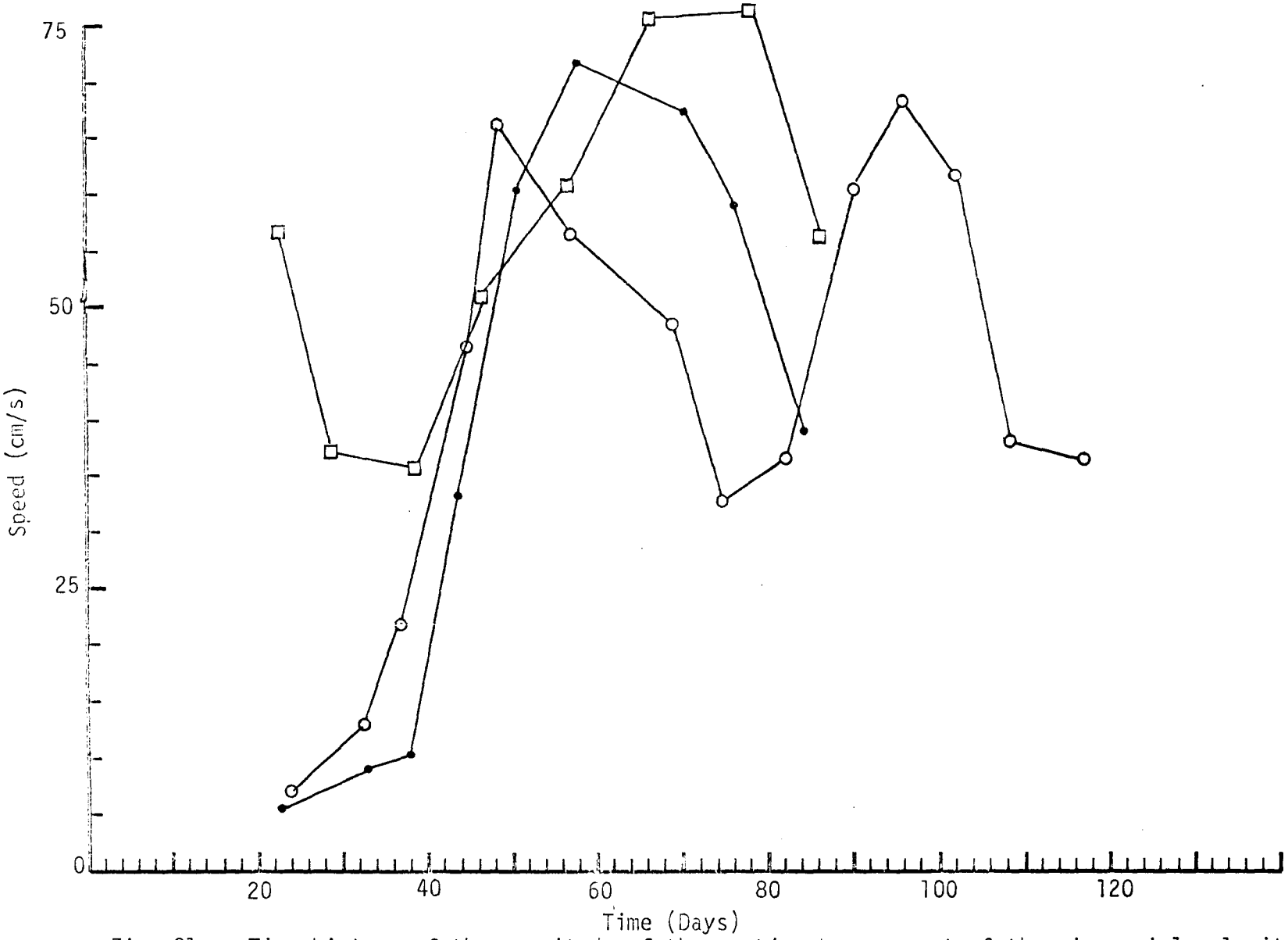

Fig. 21a. Time history of the magnitude of the east/west component of the ring swirl velocity. For ID's 1598 (dot), 1599 (circle) and 1600 (box).

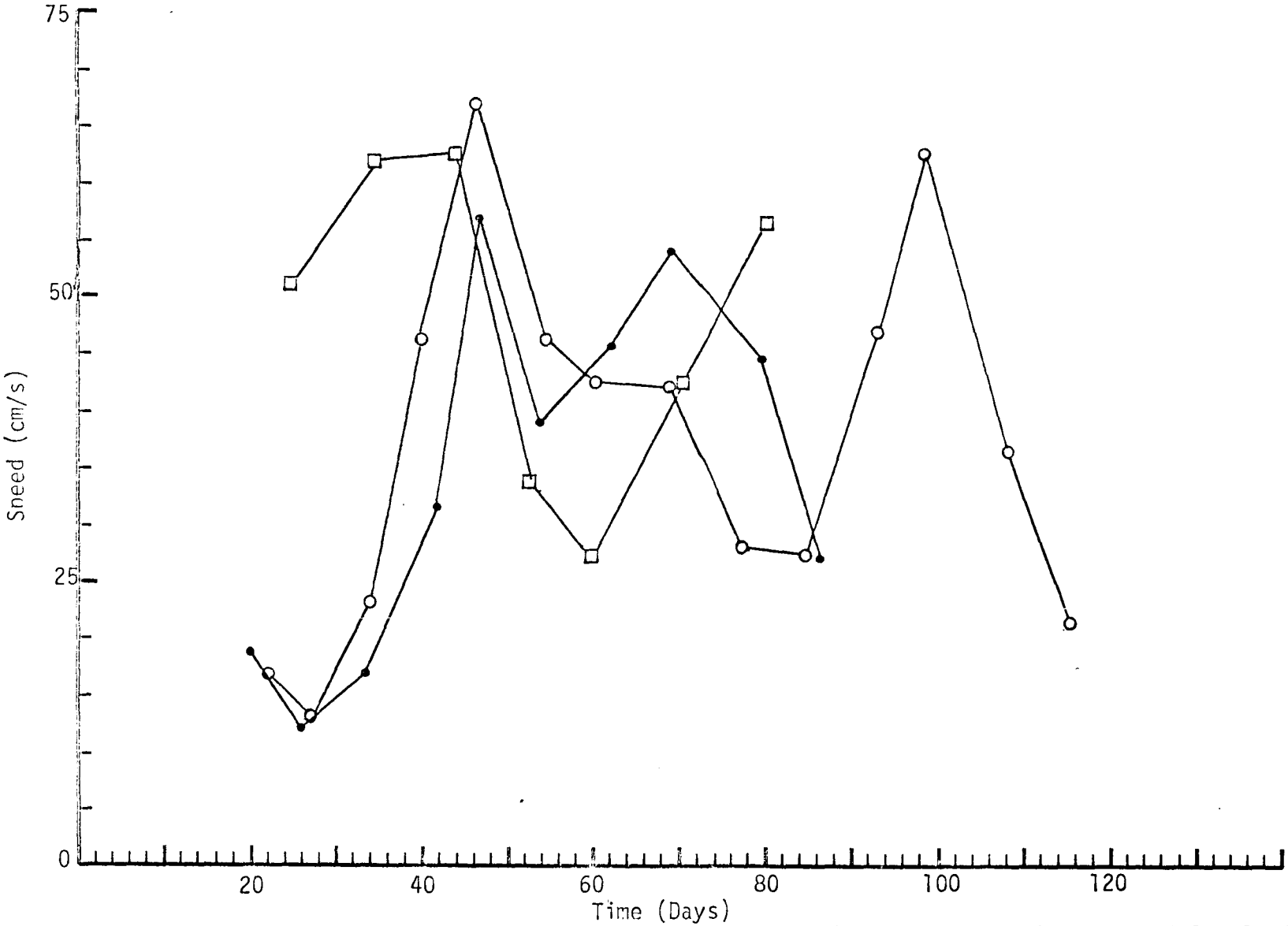

Fig. 21b. Time history of the magnitude of the north/south component of the ring swirl velocity. For ID's 1598 (dot), 1599 (circle) and 1600 (box)

Both 1598 and 1599 show an increase in the swirl velocity during the late-December - mid-January period. This coincides with the apparent increase in size of the ring noted in the discussion of the trajectories.

Figure 22 shows the time series of the ring rotation frequency ($\gamma/2$). The agreement between the estimates the u and v determined from speed components is very encouraging in that the differences are less than our expected errors. There seems to be little difference between the rotation frequency between 1598 and 1599, a fact which is consistent with the analysis of the trajectories given in section 3. The rotation frequency for 1600 is somewhat smaller than that calculated for the other two drifters. However, this is consistent with its location relative to the center and the spectral analysis discussed in section 4.

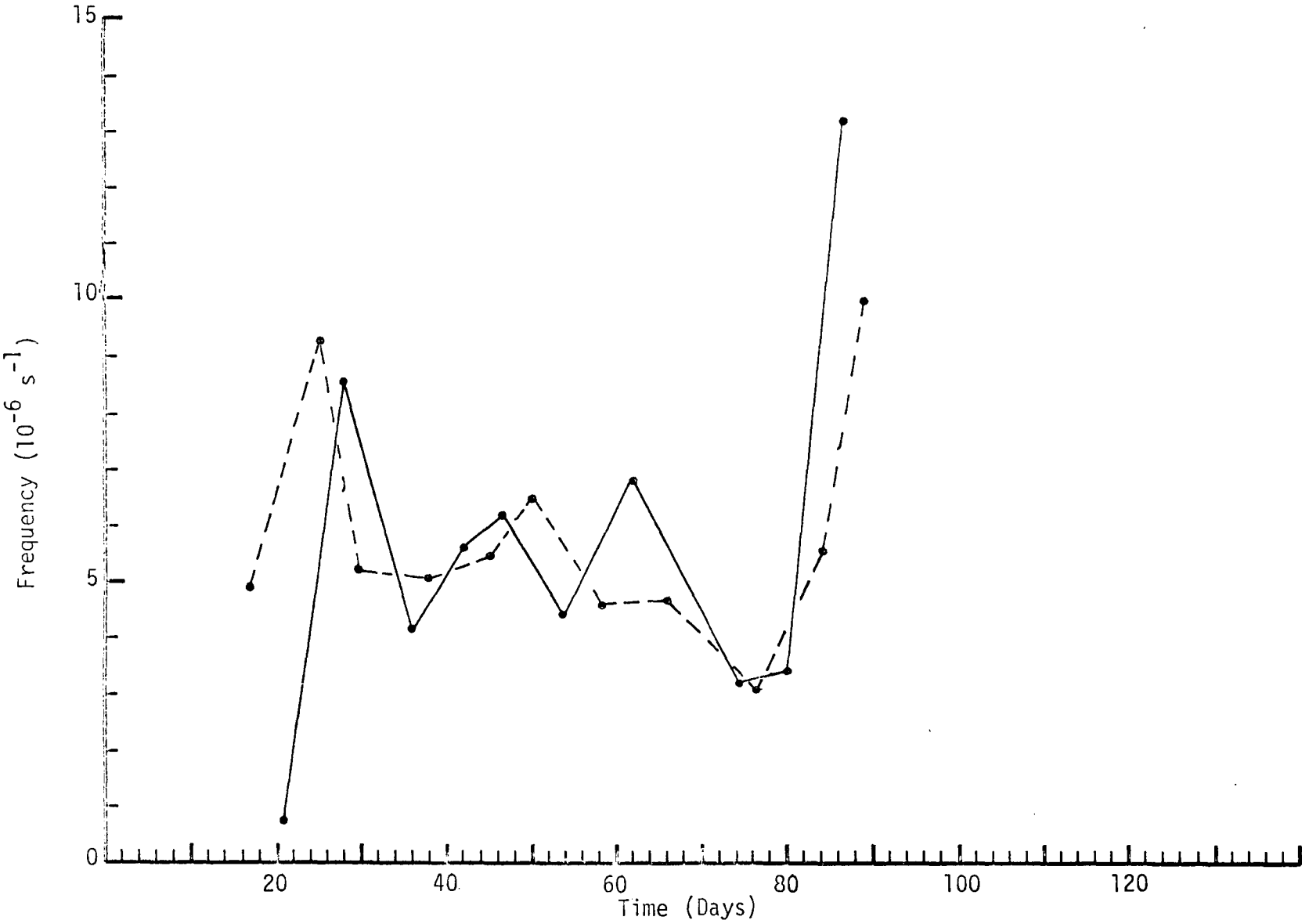

Fig. 22a. The ring rotation frequency $\gamma/2 \times 10^{-6}$, from the east-west speeds (solid) and from the north-south speeds (dashed) for ID 1598.

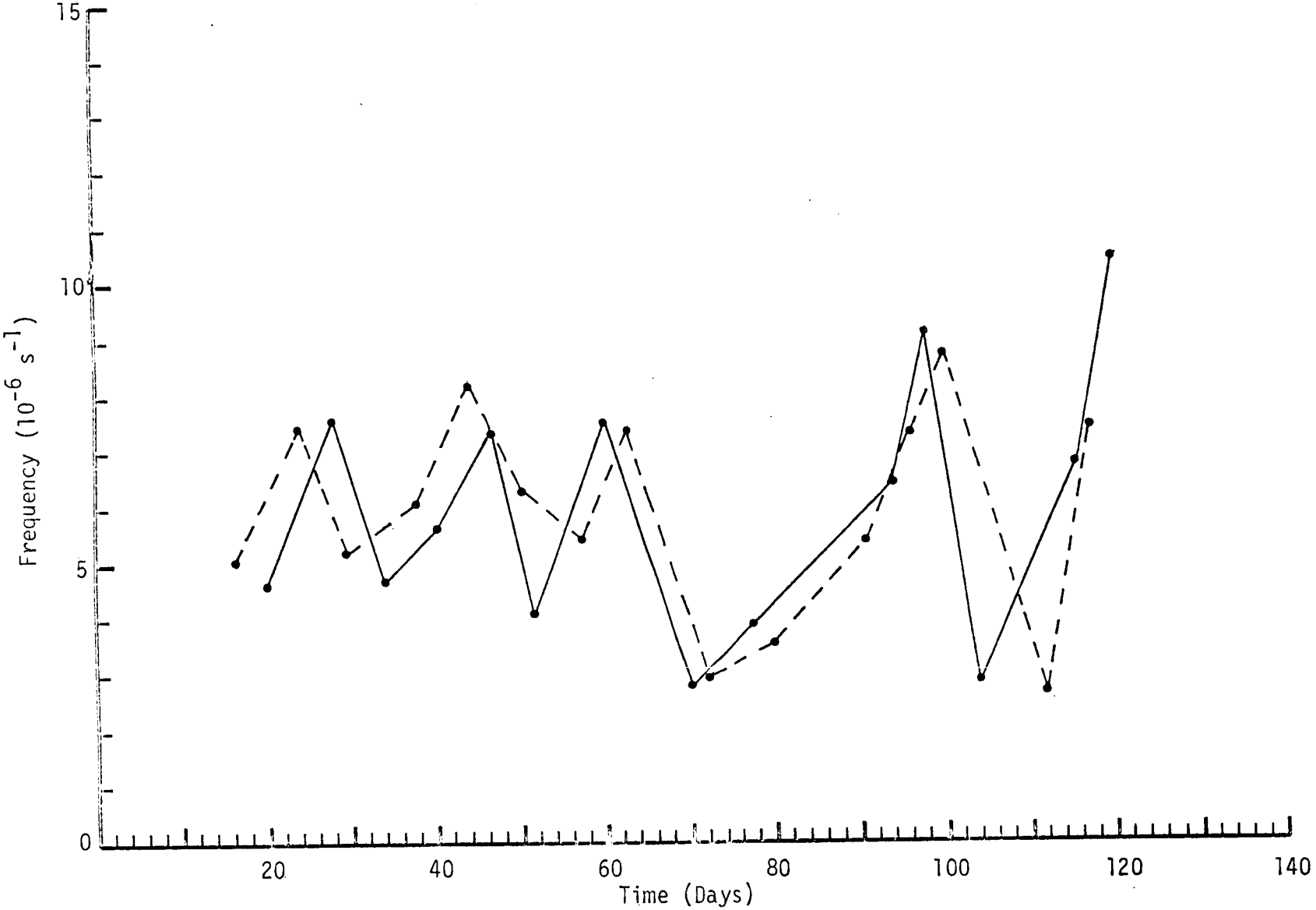

Fig. 22b. The ring rotation frequency $\gamma/2 \times 10^{-6}$, from the east-west speeds (solid) and from the north-south speeds (dashed) for ID 1599.

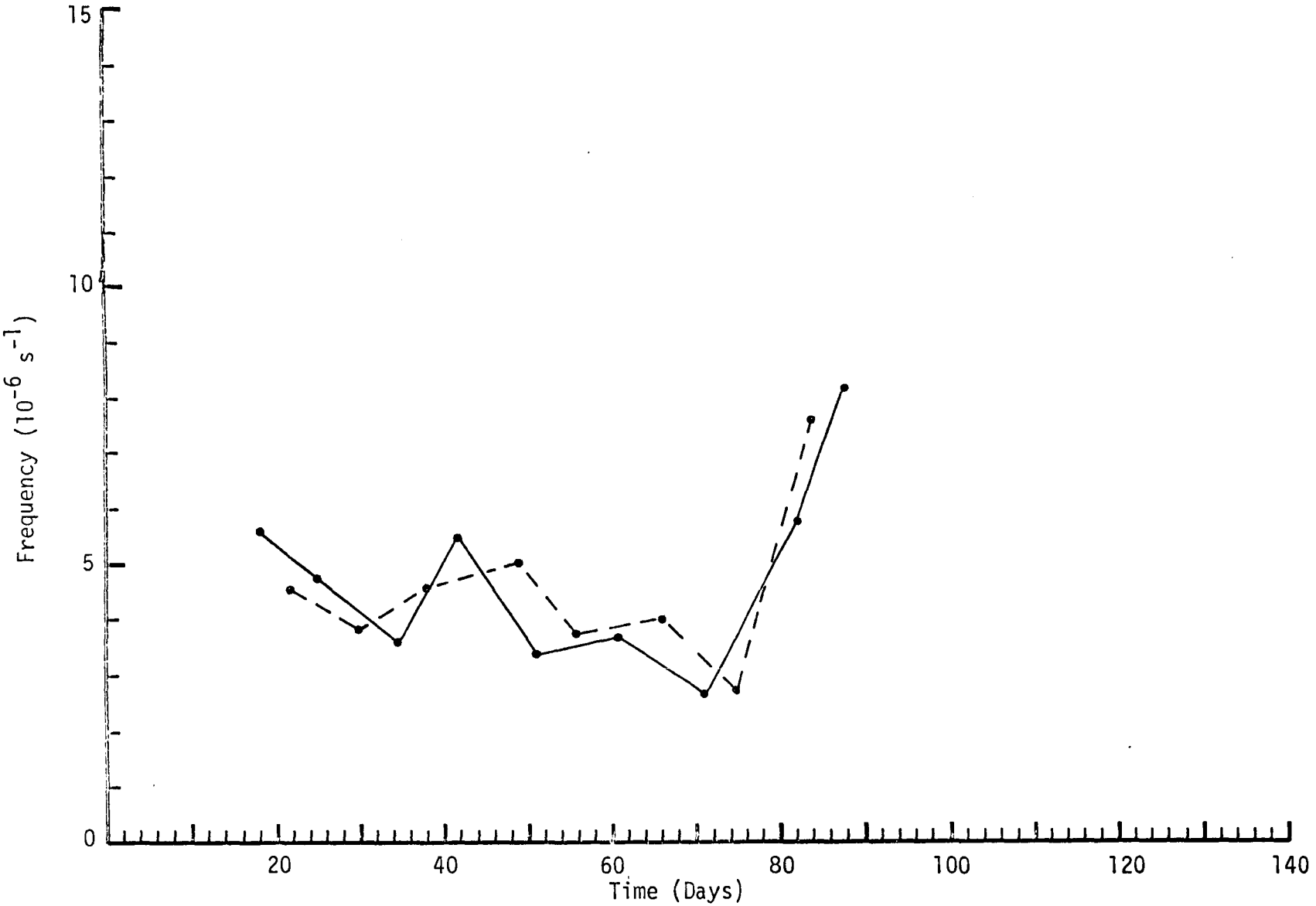

Fig. 22c. The ring rotation frequency $\gamma/2 \times 10^{-6}$, from the east-west speeds (solid) and from the north-south speeds (dashed) for ID 1600.

7. Calculation of DKP and Ring Shapes

7.1 Calculation of DKP

The general relations between the DKP and the swirl velocity amplitudes and the phase difference between the velocity components is given in section 2.6. The purpose here is to document the details of the calculations.

To illustrate the sequence of calculations and the time intervals, and the time intervals over which particular values of the DKP for a specific drifter apply, consider the following sequence of critical times:

T_1 - time of maximum u

T_2 - time of minimum v

T_3 - time of minimum u

T_4 - time of maximum v

T_5 - time of maximum u

T_6 - time of minimum v

Since the sequence of maxima and minima is periodic, it is not critical that the analysis start with a maximum u.

As explained in section 2, times T_1, T_3 and T_5 were used to calculate $\gamma/2$ for u and times T_2, T_4 and T_6 were used to calculate $\gamma/2$ for v. Furthermore, these times were also used to calculate the phase differences. Thus, there are phase differences for the sequences $T_1 - T_3$, $T_2 - T_4$, etc. Section 2 and Appendix A also document how the amplitudes and divergences were calculated. In brief, the calculation procedure provides an A_u and D for the time period $T_1 - T_5$ and B_v and D for the time period $T_2 - T_6$. The

calculations are then repeated for the next sequence of critical times, starting with T_2 and ending with T_7 (time of minimum u).

From the above it is seen that the A_u applies to the time period T_1 - T_5 and the B_v applies to the time period T_2 - T_6. Thus, the characteristic times for A_u and B_v are the respective midpoints of these intervals. Furthermore, there is an overlap of the time intervals, T_2 - T_5. The midpoint of this interval is used as the characteristic time for ζ, N and S. Note that this characteristic time deviates slightly from that of the divergence since this coincides with that of the amplitudes.

With the amplitudes, phase differences, and characteristic times thus determined, L, ζ, N and S were calculated in accordance with (2.19) - (2.20). After each calculation, the critical times were advanced by one and the calculations repeated. In this way, a time series of DKP were built up.

7.2 Discussion of DKP

Divergence

The divergences for the three drifters as determined from the u and v time series are shown in Figures 23 a and b. A comparison of the two panels indicates that the magnitudes of the divergences as calculated independently from the two components are usually less than 1×10^{-6} s^{-1}.

A comparison of the time series for individual drifters reveals some curious contrasts. At the one extreme, the two panels show that the divergences for 1599 are remarkably consistant. Values are quite comparable as are the trends. In this regard, note

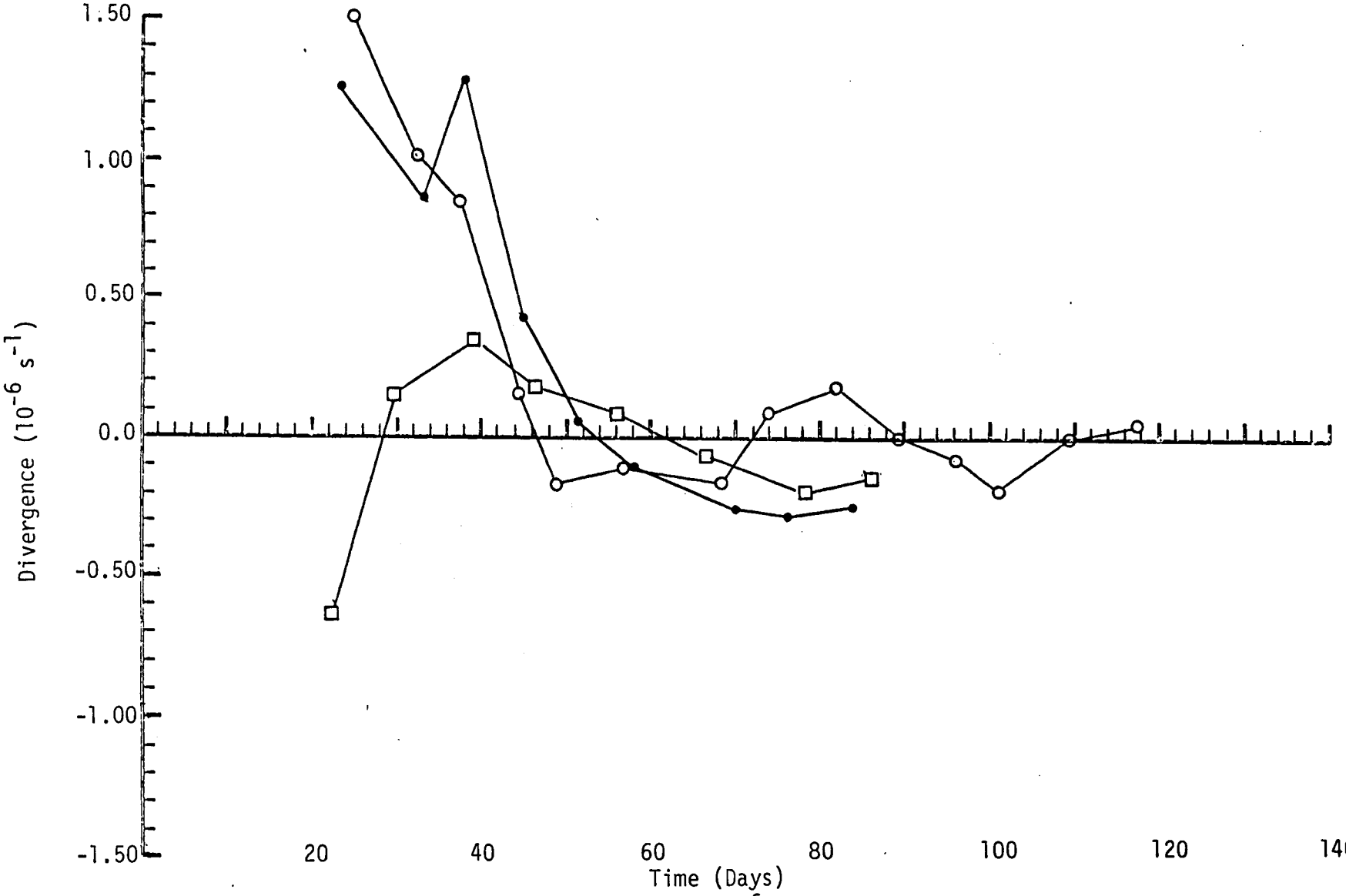

Fig. 23a. Time histories of divergence, D x 10^{-6}, computed from east-west speeds for ID's 1598 (dot), 1599 (circle) and 1600 (box).

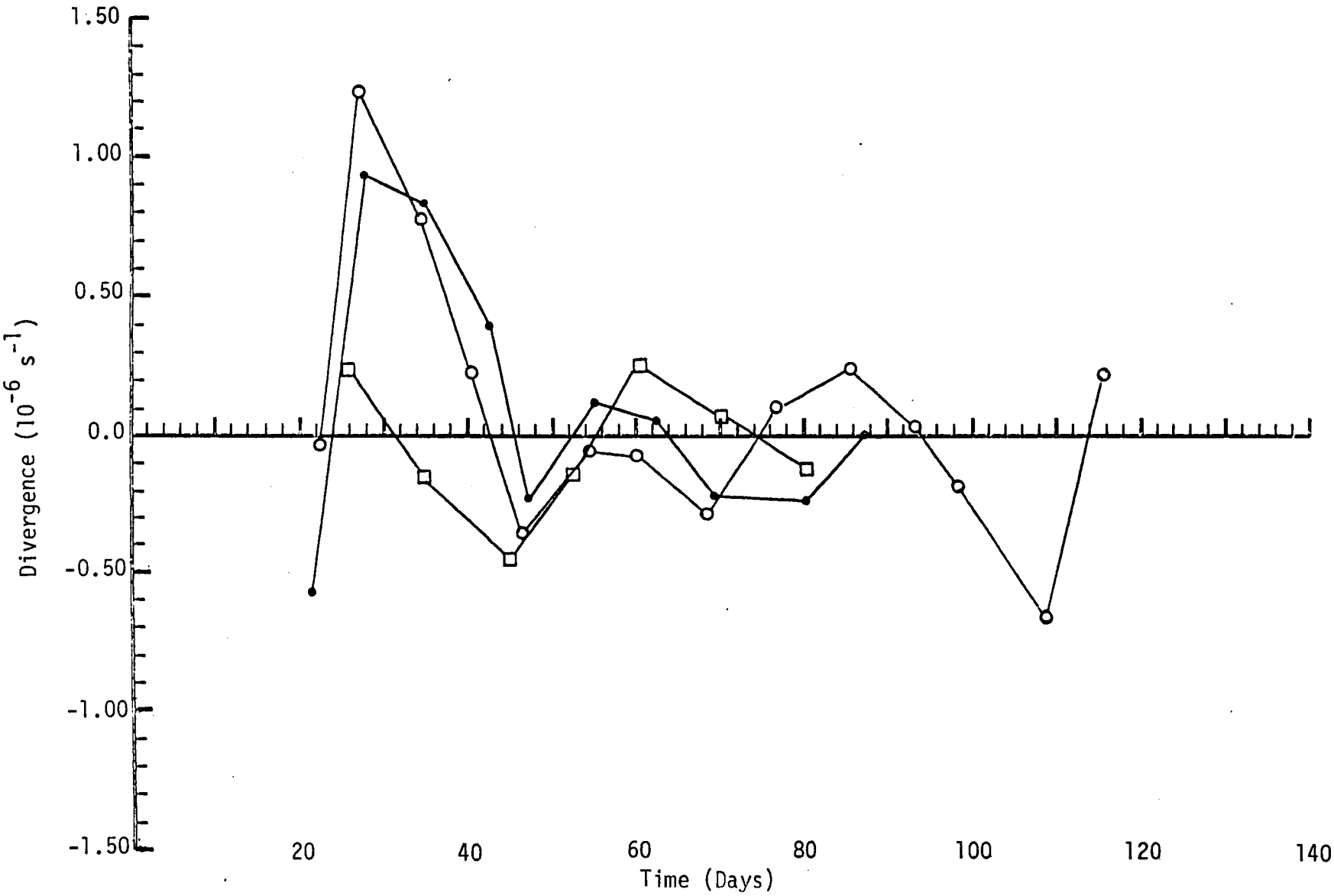

Fig. 23b. Time histories of divergence, D x 10^{-6}, computed from north-south speeds for ID's 1598 (dot), 1599 (circle) and 1600 (box).

that the sign changes occur at nearly the same time.

At the other extreme is the record of 1600. Here there is virtually no correlation between the signs and trends. For the first 30 days, the u record indicates divergence while the v record indicates convergence. The v record changes sign briefly at day 30. The one encouraging aspect is that the magnitudes of the divergence are not large.

The record for 1598 falls between these two extremes. Except for the change from negative to positive value for the v series, the records are consistent. In the early part of the records the values are consistent with the record of 1599.

It is concluded from this that 1599 gives the best representation of the divergence.

One unexplained factor is the sign changes. A classic but simple model of anticyclonic rings is that there is a slight divergence. (Cyclonic rings should exhibit a slight convergence.) The record of 1599 indicates a periodicity of about 10 days.

The values obtained from 1598 and 1600 probably reflect errors and biases arising from variations in translation speed, windage, etc. as much as they do the divergences.

Shear and Normal Deformation

Figures 24 a, b and c show the time series of the shear and normal deformation and the vorticity. The shear and normal deformations are discussed first.

Despite the small magnitudes of the order of 10^{-7} s^{-1}, there is surprising consistency between the records for different drifters. The time series for 1598 and 1599 show that the shear

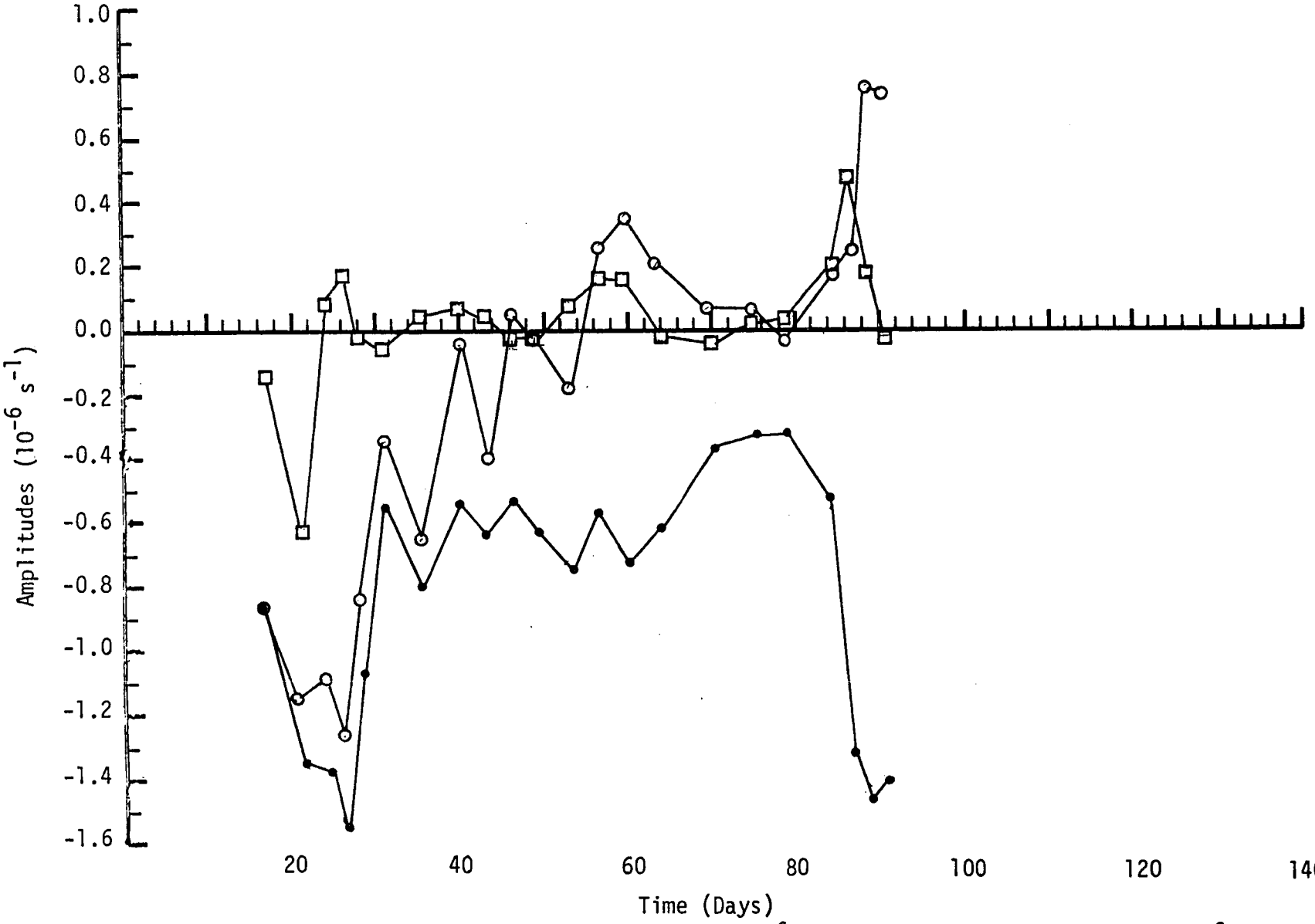

Fig. 24a. Time histories of the vorticity, $\zeta \times 10^{-6}$ (dot), shear deformation, $S \times 10^{-6}$ (circle) and normal deformation, $N \times 10^{-6}$ for ID 1598.

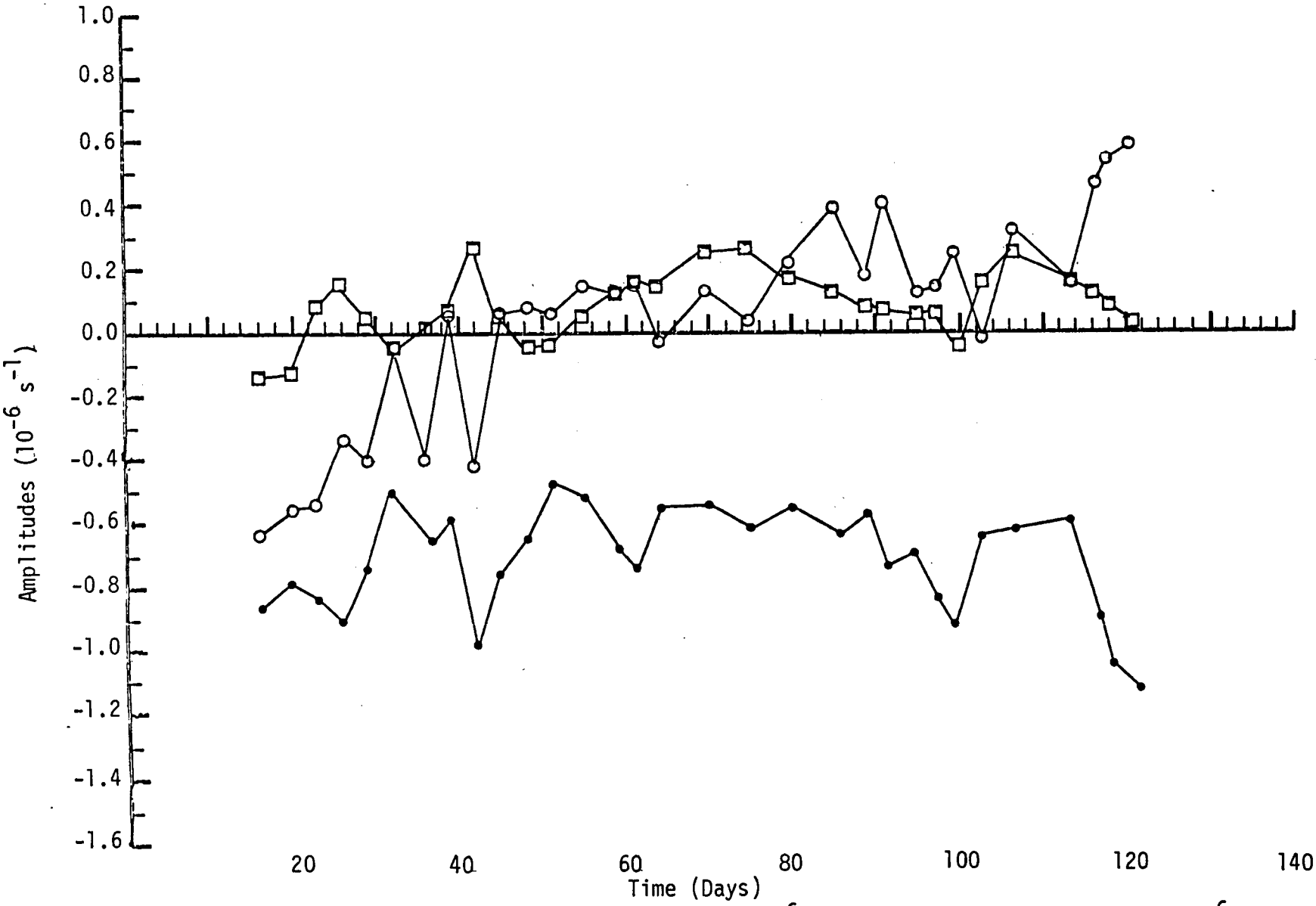

Fig. 24b. Time histories of the vorticity, $\zeta \times 10^{-6}$ (dot), shear deformation, $S \times 10^{-6}$ (circle) and normal deformation, $N \times 10^{-6}$ for ID 1599.

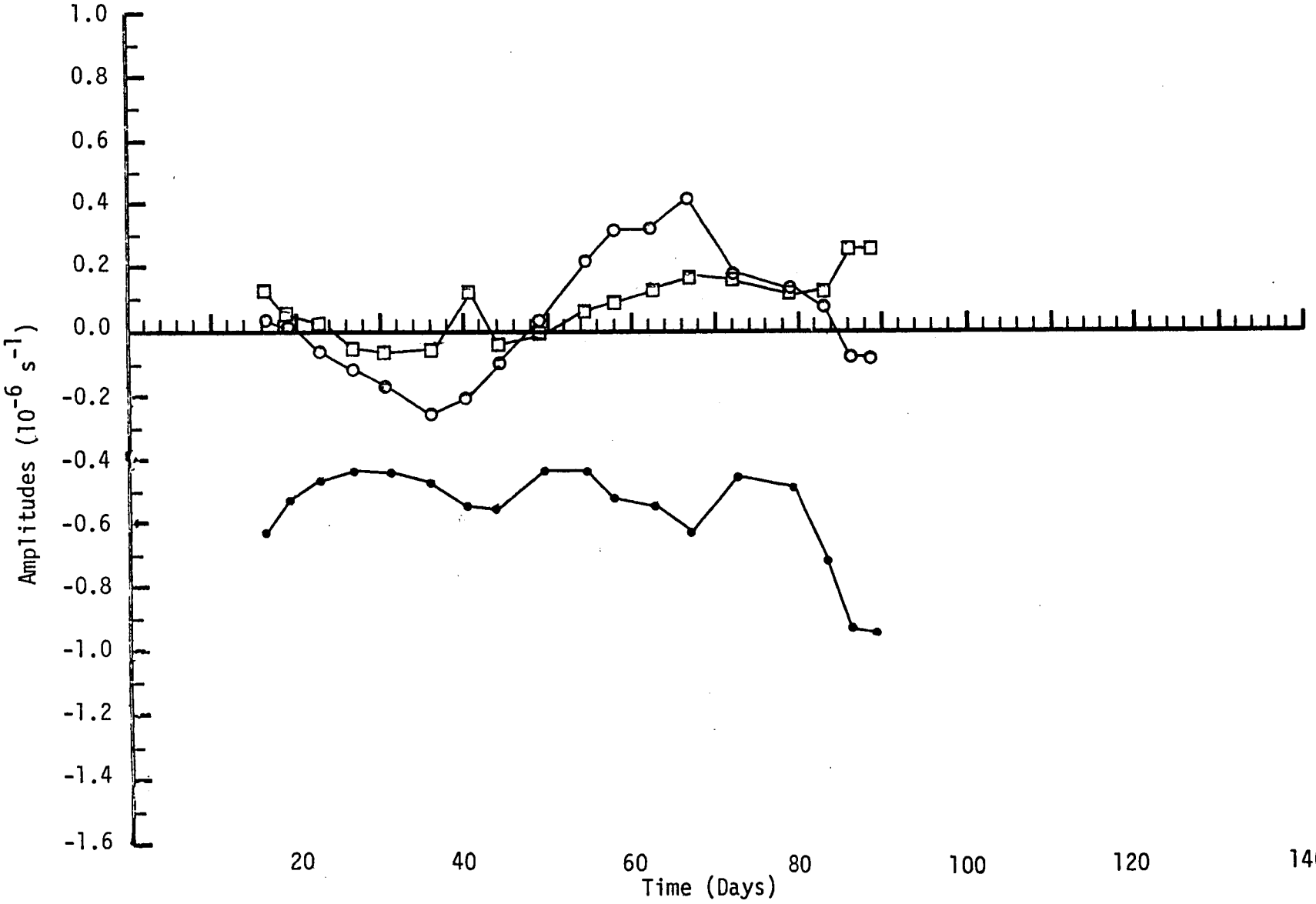

Fig. 24c. Time histories of the vorticity, $\zeta \times 10^{-6}$ (dot), shear deformation, $S \times 10^{-6}$ (circle) and normal deformation, $N \times 10^{-6}$ for ID 1600.

starts out negative but changes to positive around day 45. The time series of normal deformation also starts out negative in both cases but changes sign earlier. From day 22 on, it oscillates between positive and negative values except for one instance for 1599.

The time series for 1600 is much smoother than that of 1598 and 1599. Up until day 23, it is also out of phase with the latter two drifters. It is important to note, however, that the magnitudes of the deformation as given by the three drifters are comparable.

Because of the general consistency shown in these figures, it is felt that the values reported for the shear and normal deformation are reliable. The differences in detail between 1600 and the other two drifters can be accounted for by a difference in location, relative to the ring center, of this drifter. As it is clearly near the edge of the ring, it is reasonable to expect that it will experience different dynamical processes.

Vorticity

The time series of vorticity are perhaps the most encouraging result of all. They show remarkably little fluctuations and are quite consistent with each other. The vorticities recovered from 1598 and 1599 are very similar for the first 40 days. At the very end of the record of 1598, there is some deviation. However, the vorticity time series of 1599 is uniform for almost 60 days. The average values of both are about 7×10^{-7} s^{-1} with typical fluctuations of less than 2×10^{-7} s^{-1}.

The time series for 1600 is also quite uniform. The average value is about 5×10^{-7} s^{-1} with typical fluctuations of about

1×10^{-7} s^{-1}. That this is lower than the values for 1598 and 1599 is entirely consistent with the fact that this drifter was located further from the ring center. As shown in section 2, the presence of some deformation in the swirl velocity field can result in a lower rate of rotation near the ring edge. Also, it is not clear where the path of 1600 is respective to the curve of maximum swirl velocity. If it is even slightly beyond this curve, its rotation rate will be substantially reduced even if there is a deformation.

Perhaps the most important aspect of the DKP calculations is the relative magnitudes. Clearly, the dominant component in every case is the vorticity. Typically, it is 5 to 10 times as large as the other DKP. The role of the shear and normal deformation rates seem to be to produce geometric changes in the ring. They seem to have much less effect on the frequency of ring rotation. The role of horizontal divergences in ring dynamics appears to be less than the other DKP.

7.3 Calculation of Ring Geometry

There are three aspects to the calculation of ring geometry from the DKP. The first is that any divergence can distort the ring during the course of one revolution of a drifter. In the analysis given below, this distortion has been removed by calculating the geometric characteristics from the parametric equations:

$$x\, e^{-Dt/2} = A_u\, (2/\gamma) \cos P$$

$$y\, e^{-Dt/2} = B_v\, (2/\gamma) \sin P$$

The most general ring shape permitted by our model is an ellipse. There are three parameters which specify the ellipse at any

one time. It is stressed that each drifter may see different ellipse characteristics at a common time since the distances from the ring center vary from drifter to drifter.

This leads to the second aspect of the ring geometry calculations; namely the calculation of the geometric parameters. The first of these is the ring orientation. This was calculated at appropriate characteristic times from (2.16). The ellipse major axis was determined from the "Stokes" relations (2.20) by

$$\text{major axis} = \sqrt{(A_u^2 + B_v^2)\ (2/\gamma)^2}\ . \tag{7.1}$$

The minor axis is given by

$$\text{minor axis} = \sqrt{|A_u^2 - B_v^2|\,(2/\gamma)^2}\ . \tag{7.2}$$

Note that the characteristic time for each of these geometric parameters are the same.

The third aspect of the ring geometry calculations is the location of the ring center. To see how this is done, (2.17) is rewritten as

$$\begin{aligned} x_a &= x_c + x \\ y_a &= y_c + y\ . \end{aligned} \tag{7.3}$$

Here the subscripts a and c denote the absolute geographic positions and the ring center positions, respectively. The absolute positions at each critical time are, of course, known. At critical time T_1, the relative displacements (x,y) are given by

$$\begin{aligned} x &= (2/\gamma)\ A_u \\ y &= (2/\gamma)\ B_v \sin(-2\Gamma)\ . \end{aligned} \tag{7.4}$$

Different critical times will produce different displacement relations.

They are however, readily evaluated from (2.10).

From this it is seen that x_a, y_a, x, and y are all known at each critical time. Thus, from (7.3), the location of the ring center is easily obtained.

7.4 Discussion of Ring Geometry

Figure 25 shows the time series of the major and minor axes of the ring as determined by the three drifters. For clarity in presentation, only one segment of the major and minor axes is shown. When comparing the results of the three drifters, it is important to realize that there is no a-priori reason to expect any agreement. Each drifter tags a parcel from a different part of the ring. Just as each planet has a different ellipitical orbit about the sun, each parcel may follow a different path about the ring.

The figure shows that all three drifters persistently indicate an ellipitical ring. This is in sharp contrast with most theoretical models of rings which are assumed to be circular. Another aspect is that all three drifters indicate an orientation of ±30° of east/west. Moreover, from the first part of January 1981, all three drifters indicate a major axes orientation along 070° T - 250° T. This agreement is quite encouraging in that it indicates that one drifter can suffice for determining the ring orientation.

This is not the case on ring dimensions. It is seen from Figure 25 that drifters 1598 and 1599 are in close agreement on both the orientation and size of the major and minor axis. Clearly, this could be the result of the fact that they were seeded in the ring close together. An obvious implication of this is that errors in the

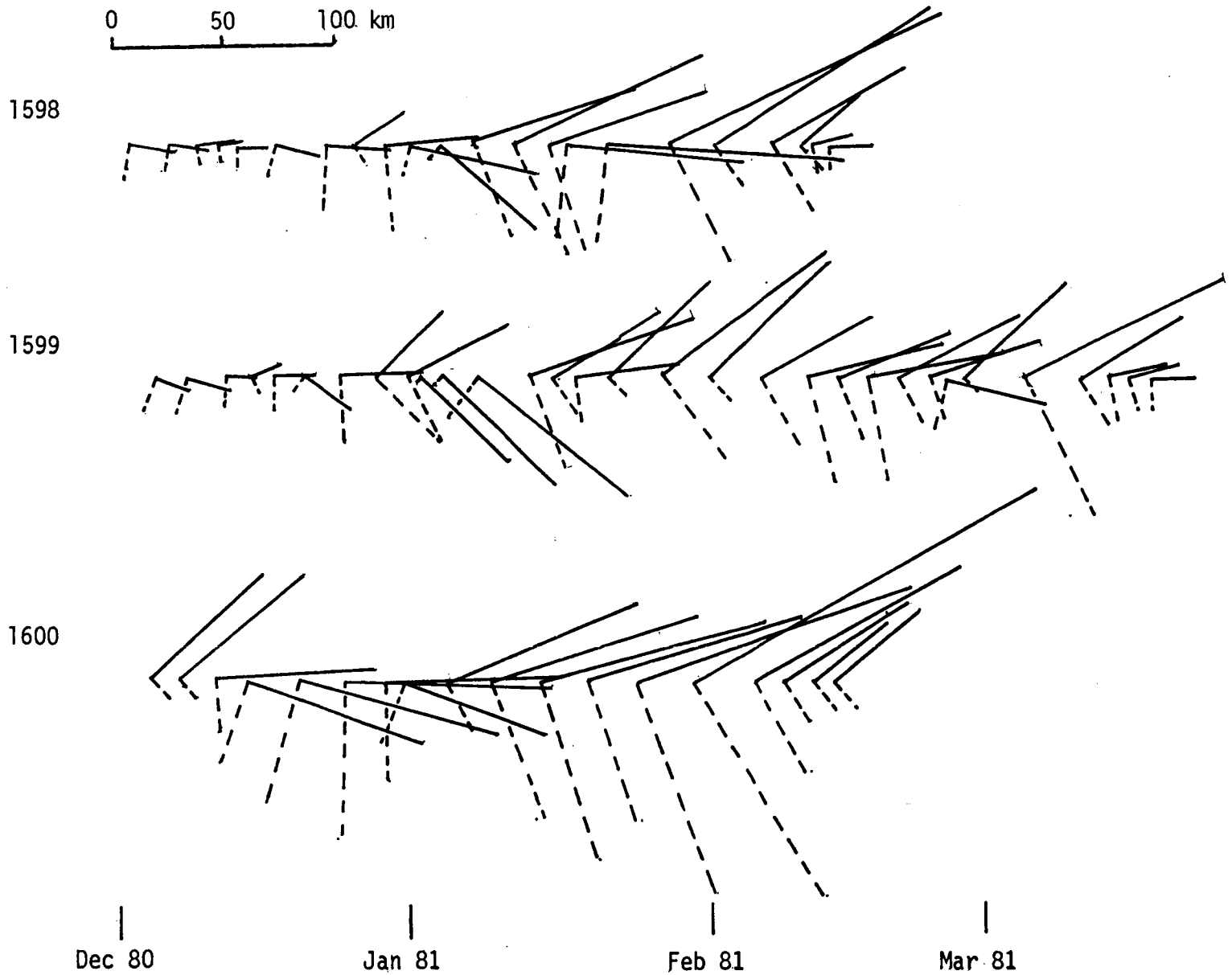

Fig. 25. Time histories of ellipse orientations. Half of the major axes (solid) and half of the minor axes (dashed) are shown. Lengths are to scale.

calculations of the DKP are not significantly biasing the results.

It appears from Figure 25 that, during the course of the deployment, the length of both the major and minor axes as determined by all three drifters increased. There are reversals to this trend in early January and early February 1981. The trend towards an increase in the lengths of the major and minor axes is consistent with the concept that there is divergence in an anticyclonic ring. In this regard, it is encouraging that the times of decreasing axis length are generally consistent with the changes in sign of the divergence (Figure 23).

Drifters 1598 and 1599 start off showing a circular ring with a path radius of about 40 km. After the middle of January, the major axis of the orbits of these two drifters increases to about 160 km while the minor axis increase to about 60 km. After the middle of January 1981, the major axis of 1599 is nearly constant at about 120 km while the minor axis stays at about 70 km. The only exception is a single estimate of exceptionally high values in early March.

Drifter 1600 initially indicates an ellipitical ring (orientation of the major axis of about 045° T to 225° T) with a major axis of 140 km and a minor axis of 30 km. During the course of the deployment, the major axis increased to over 250 km and the minor axis to over 200. The final values, however, are quite consistent with those obtained from 1598 and 1599.

Figure 26 show the ring center location and geometry on the base map of the Gulf of Mexico for a few selected times. This

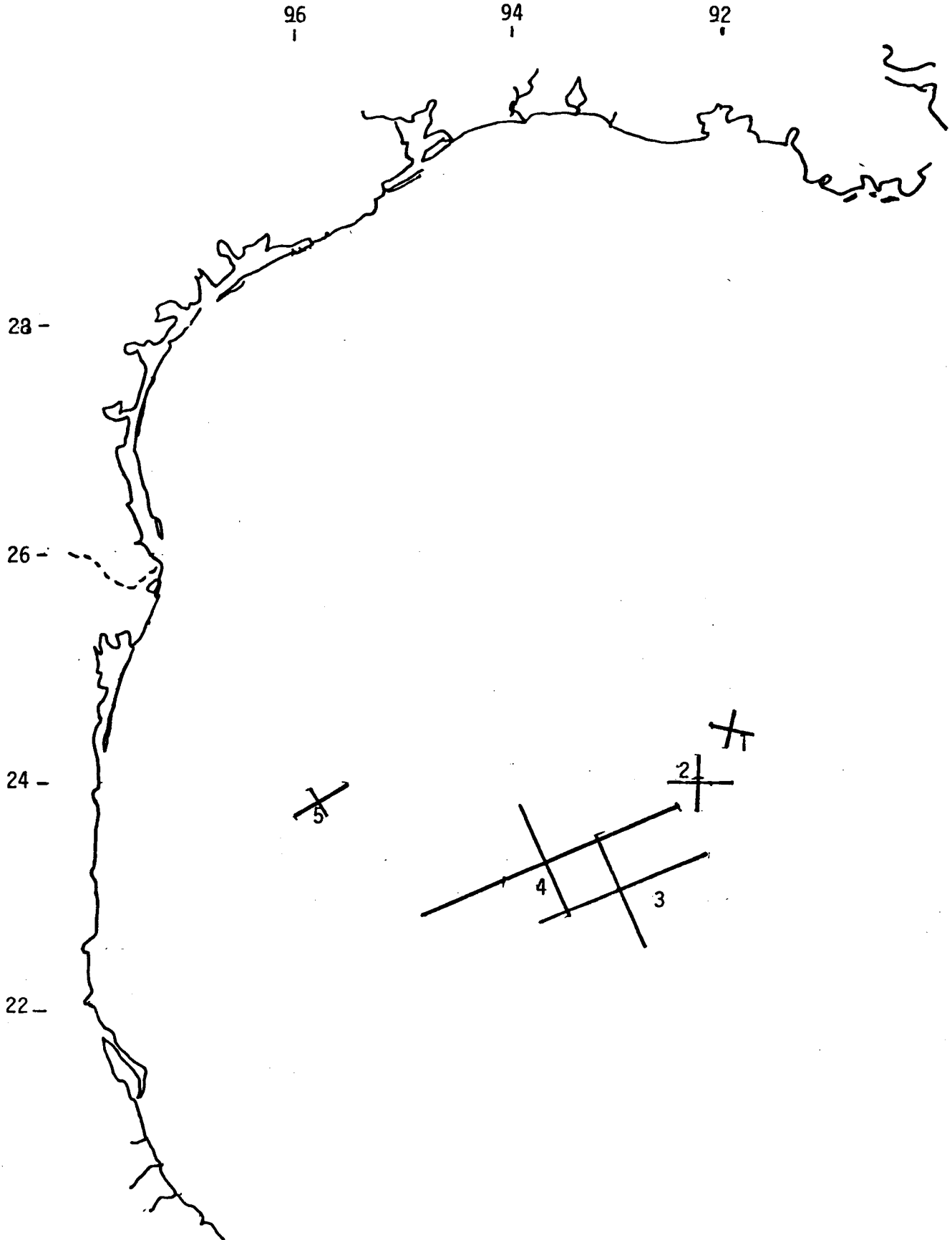

Fig. 26a. Location and shape of ring from ID 1598 on (1) 5 Dec, 25 Dec 80, (3) 14 Jan, (4) 30 Jan and (5) 14 Feb 81.

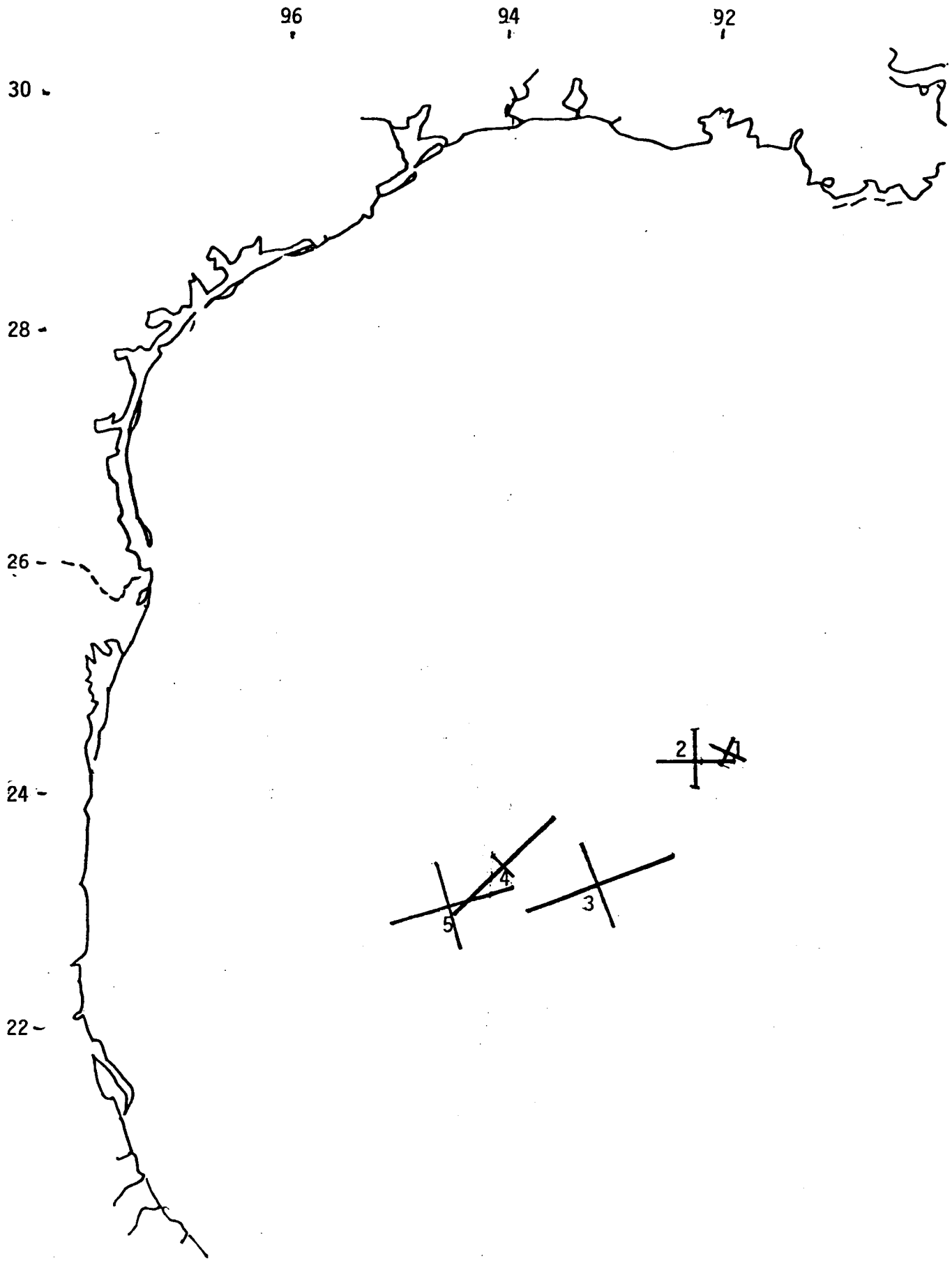

Fig. 26b. Location and shape of ring from ID 1599 on (1) 5 Dec, (2) 24 Dec 80, (3) 13 Jan, (4) 27 Jan and (5) 12 Feb 81.

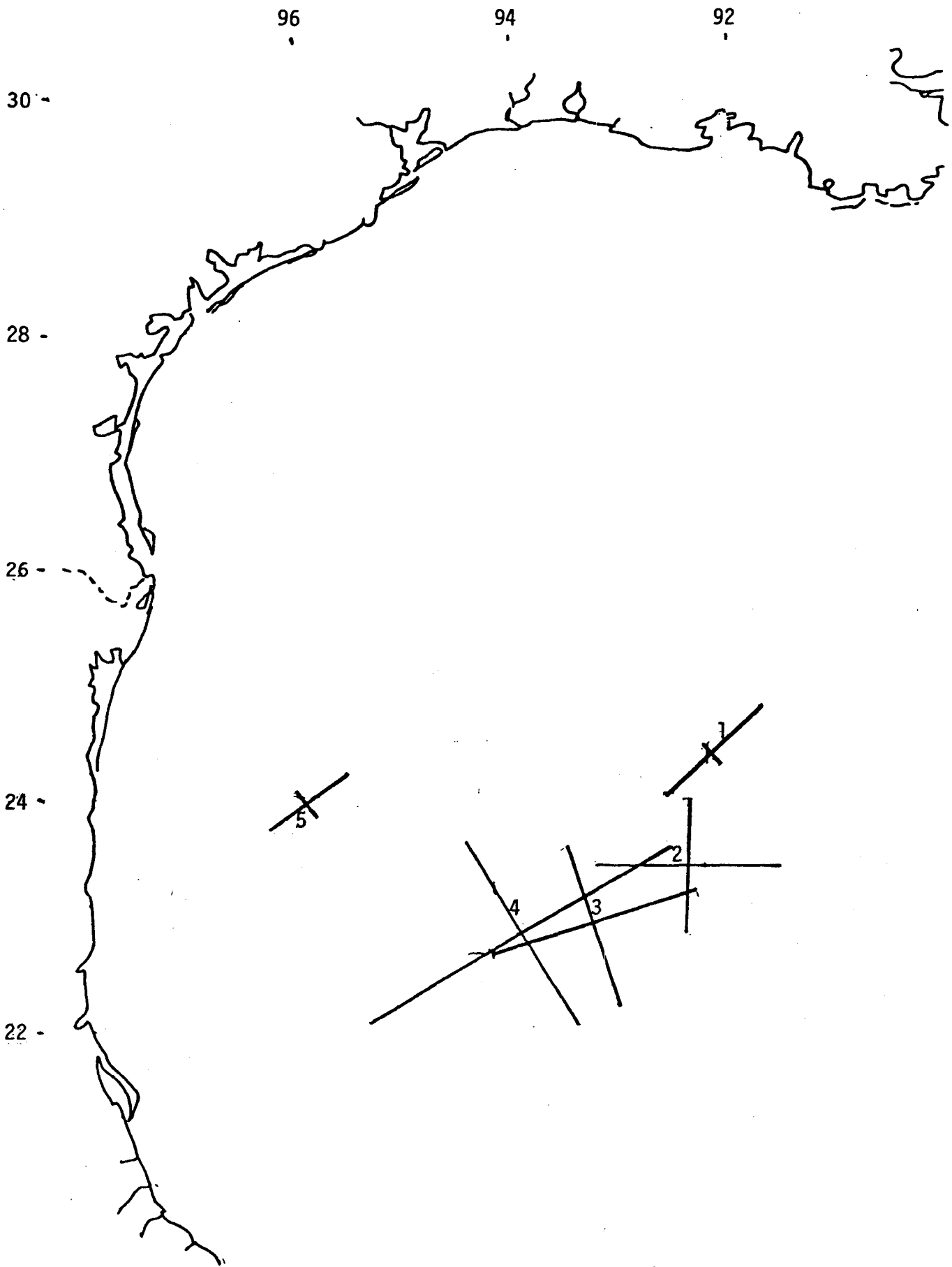

Fig. 26c. Location and shape of ring from ID 1600 on (1) 5 Dec, (2) 25 Dec 80, (3) 15 Jan, (4) 31 Jan and (5) 13 Feb 81.

figure illustrates the general consistency of the method of locating the ring center.

8. Conclusions and Recommendations

The analysis described in this report indicates a number of conclusions and recommendations concerning future drifter deployments. It should be kept in mind that these conclusions are based on the analysis of data from an anticyclonic ring in the Gulf of Mexico. The behavior of cyclonic rings, other mesoscale features, and anticyclonic rings in other regions may well be different.

1) The motions within a ring do not separate drifters. It is expected that a drifter array whose scale is less than that of a ring will not be dispersed if the array is deployed within a ring. It follows from this that the separation of elements of a drifter array are the result of translations by different rings.

Recommendation - The scale of drifter arrays need not be smaller than the typical ring size.

2) The general agreement between all three drifters on rotation rate, ring translations, ring orientation, and the DKP suggest that one drifter, if carefully seeded in the ring, will suffice to determine these characteristics. One drifter, however, is not sufficient to determine the ring size. This will require additional measurements, presumably from the thermal field.

Recommendation - For a field program in the Gulf of Mexico, it is essential that ship of opportunity or, even better, AXBT surveys be made of the ring. These can be used to determine the absolute ring size.

3) For the Gulf of Mexico, substantial analysis, i.e. spectral analysis and filtering, are required to recover the DKP from the drifter velocities.

4) Of all the DKP, the vorticity is clearly the most important. There appears to be insignificant separation of the drifters associated with the shear and normal deformation and the divergence.

5) It is clear that the ring undergoes substantial modification, even in deep water, as it moves across the Gulf of Mexico. This modification is reflected in a general increase in area and development of an east-west elliptical orientation.

6) Typical ring translation speeds of the ring are of the order of 5 cm/s. The swirl velocities, however, are of the order of 50 cm/s.

Acknowledgements

The research reported here was performed under contract NA-81-QA-C-148 between Science Applications, Inc. and NDBC. We thank Mr. E. Kerut and Dr. G. Hamilton of the NDBC and Dr. M. Brown of the Minerals Management Service for their support and encouragement. Mrs. V. Covington performed the difficult task of typing the manuscript with exceptional good humor, patience and, above all, great skill.

Bibliography

Lewis, J. K. and A. D. Kirwan, 1981: "Analysis of horizontal shear data." Final Report, NRL, contract N00014-81-C-2102, 63 pp.

Molinari, R., and A. D. Kirwan, 1975: "Calculation of differential kinematic properties of the Yucatan Current from Lagrangian observations." J. Phys. Oceanogr., 5, 483-491.

Mungall, J. C. H., C. E. Abel, and C. R. Olling, 1978: Hydrodynamic model estimates of the M_2 and K_1 currents of the Gulf of Mexico. Tech. Rpt. 78-9-T, Texas A&M University Research Foundation. 109 pp.

Okubo, A., 1970: "Dispersion of floatable particles in the vicinity of velocity singularities such as convergences." Deep Sea Res., 17, 445-454.

Okubo, A., and C. C. Ebbesmeyer, 1976: "Determination of vorticity, divergence, and deformation rates from analysis of drogue observations." Deep Sea Res., 23, 349-352.

Petterssen S.: "On the relation between vorticity, deformation, and divergence and the configuration of the pressure field." Tellus, 5 (3), 1953.

Reid, R. O. and R. E. Whitaker, 1981: "Numerical model for astronomical tides in the Gulf of Mexico." In Press, U. S. Army Engineer Waterways Experiment Station, Vicksburg, MS.

Stephens, J. J., 1965: "A variational approach to numerical weather analysis and prediction." Ph.D. Dissertation, Dept. of Meteor., Texas A&M University, College Station, Texas.

Stephens, J. J., 1967: "Variational statements of quasi-static and geostrophic equilibria." Die Beit. zur Physik dur Atmosphäre, 40, 3, 103-107.

Thomas, C. B., 1958: Calculus and Analytical Geometry. Addison-Wesley Publishing Company, Reading, MA.

Appendix A - Calculation of Amplitudes, Divergences and Translation Velocities

Introduction

The purpose of this appendix is to document the technique for calculating the amplitudes, divergences and translation velocities from the absolute velocity records. The procedure is based upon the assumption that the velocities and DKP do not vary over one rotation period. The procedure also provides independent estimates of the divergence from the east and the north velocity records. It is possible to develop a paridigm which yields the same value of the divergence from the east and north velocity records. The calulation is considerably more difficult and, in view of the results given in section 7, unwarrented in that the independent estimates of divergence do not differ significantlv.

The procedure given below is exact but requires an iterative solution technique. An example is given for the x (east/west) velocity component which has a starting time (t_o) at a local maximum of the absolute velocity. The times when the x velocity is at the following minimum and maximum is t_1 and t_2, respectively. The velocities at t_o, t_1, and t_2 are denoted by $\hat{u}_o$, $\hat{u}_1$, and $\hat{u}_2$, respectively. The extension of this method to subsequent times and the y (north/south) velocity component is straight-forward.

From (2.4) and (2.15) and the assumptions given above, the values of the absolute velocity at the critical times are

$$\hat{u}_o = U + A_u \tag{A.1}$$

$$\hat{u}_1 = U - A_u\, e^{Dt_1/2} \tag{A.2}$$

$$\hat{u}_2 = U + A_u\, e^{Dt_2/2}\,. \tag{A.3}$$

Eliminating D between (A.2) and (A.3) yields

$$\ln[(U - \hat{u}_1)/A_u] = (t_1/t_2) \ln[(\hat{u}_2 - U)/A_u] .$$

Solving for A_u gives

$$A_u = [(U - \hat{u}_1)^{t_2}/(\hat{u}_2 - U)^{t_1}]^{1/(t_2 - t_1)} . \qquad (A.4)$$

By inserting (A.4) into (A.1), one obtains

$$U = \hat{u}_o - [(U - \hat{u}_1)^{t_2}/(\hat{u}_2 - U)^{t_1}]^{1/(t_2 - t_1)} . \qquad (A.5)$$

This last equation may be solved by iteration. The relaxation technique used for this work used the iterative expression

$$U_n = U_{n-1} + R[\hat{u}_o - [(U_{n-1} - \hat{u}_1)^{t_2}/(\hat{u}_2 - U_{n-1})^{t_1}]^{1/[t_2 - t_1]}] \qquad (A.6)$$

where the initial value of U was zero and the relaxation constant R was varied between 0.2 and 0.8 in order to produce convergence. The convergence criteria was $|U_n - U_{n-1}| < 0.001$ m/s.

Once U is determined, (A.4) is used to calculate the swirl velocity magnitude A_u. Finally, the value for D is given by solving (A.2) or (A.3) for D.

In the event that the calculations start with a minimum in u, the procedure given above is repeated except that the signs of the second terms on the right hand side of (A.1) - (A.3) are reversed. The result for this situation is

$$U = \hat{u}_o + [(\hat{u}_1 - U)^{t_2}/(U - \hat{u}_2)^{t_1}]^{1/(t_2 - t_1)} \qquad (A.7)$$

$$A_u = [(\hat{u}_1 - U)^{t_2}/(U - \hat{u}_2)^{t_1}]^{1/(t_2 - t_1)} \qquad (A.8)$$

$$D = (2/t_1) \ln[(\hat{u}_1 - U)/A_u] = (2/t_2) \ln[(U - \hat{u}_2)/A_u] . \qquad (A.9)$$

The Department of the Interior Mission

As the Nation's principal conservation agency, the Department of the Interior has responsibility for most of our nationally owned public lands and natural resources. This includes fostering sound use of our land and water resources; protecting our fish, wildlife, and biological diversity; preserving the environmental and cultural values of our national parks and historical places; and providing for the enjoyment of life through outdoor recreation. The Department assesses our energy and mineral resources and works to ensure that their development is in the best interests of all our people by encouraging stewardship and citizen participation in their care. The Department also has a major responsibility for American Indian reservation communities and for people who live in island territories under U.S. administration.

The Minerals Management Service Mission

As a bureau of the Department of the Interior, the Minerals Management Service's (MMS) primary responsibilities are to manage the mineral resources located on the Nation's Outer Continental Shelf (OCS), collect revenue from the Federal OCS and onshore Federal and Indian lands, and distribute those revenues.

Moreover, in working to meet its responsibilities, the **Offshore Minerals Management Program** administers the OCS competitive leasing program and oversees the safe and environmentally sound exploration and production of our Nation's offshore natural gas, oil and other mineral resources. The MMS **Minerals Revenue Management** meets its responsibilities by ensuring the efficient, timely and accurate collection and disbursement of revenue from mineral leasing and production due to Indian tribes and allottees, States and the U.S. Treasury.

The MMS strives to fulfill its responsibilities through the general guiding principles of: (1) being responsive to the public's concerns and interests by maintaining a dialogue with all potentially affected parties and (2) carrying out its programs with an emphasis on working to enhance the quality of life for all Americans by lending MMS assistance and expertise to economic development and environmental protection.